Preliminary Investigation of High-Velocity Liquid Impact Damage

Tennessee Technological University

prepared for
Army Missile Command

DECEMBER 1972

TTU-ES-72-2

PRELIMINARY INVESTIGATION OF
HIGH-VELOCITY LIQUID IMPACT DAMAGE

RAY KINSLOW, VIRESHWAR SAHAI, AND JOHN PEDDIESON, JR.

PRINCIPAL INVESTIGATORS

AD753381

Prepared For

U.S. ARMY MISSILE COMMAND

REDSTONE ARSENAL

ALABAMA

CONTRACT NUMBER DAAH01-72-C-0375

DECEMBER 1972

TENNESSEE TECHNOLOGICAL UNIVERSITY

DEPARTMENT OF ENGINEERING SCIENCE

COOKEVILLE, TENNESSEE 38501

TTU-ES-72-2

PRELIMINARY INVESTIGATION OF

HIGH-VELOCITY LIQUID IMPACT DAMAGE

RAY KINSLOW, VIRESHWAR SAHAI, AND JOHN PEDDIESON, JR.

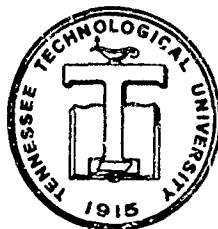PRINCIPAL INVESTIGATORS

Prepared For

U. S. ARMY MISSILE COMMAND

REDSTONE ARSENAL

ALABAMA
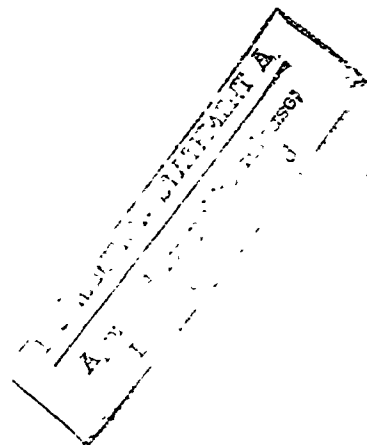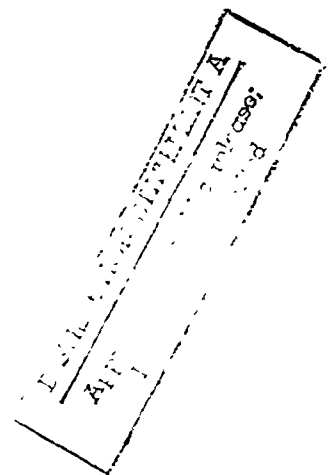
CONTRACT NUMBER DAAH01-72-C-0375

DECEMBER 1972

TENNESSEE TECHNOLOGICAL UNIVERSITY

DEPARTMENT OF ENGINEERING SCIENCE

COOKEVILLE, TENNESSEE 38501

ABSTRACT

The research described has been directed toward an understanding
of the mechanics of rain erosion of materials traveling at very high
velocities. An analysis of the motion of raindrops in a hypersonic
shock layer is described. A high-speed jet impingement analogy of the
impact of liquid drops on solid surfaces is used to analytically deter-
mine the cavity profile. The effect of stress waves generated by
liquid impact is discussed. It is shown that internal damage and
spallation resulting from stress waves is often much greater than the
material failure in the impact area itself. Experiments have demon-
strated that water-drop impact can be closely simulated by the use of
a high-speed water jet. Craters formed in the laboratory by the jet
are compared with those of a radome surface after a sled test in a
rainfield.

CONTENTS

ILLUSTRATIONS

APPENDIX 1

SECTION I.
INTRODUCTION

The requirement of an all-weather capability for high-speed aircraft and missiles has made rain erosion protection of these systems a vital design factor. No dependable design criterion, however, has yet been formulated. In a state-of-the-art survey of raindrop erosion, Wheelahan (1967) finds that very little quantitative information is available on damage caused by raindrops impacting at supersonic velocities. Heymann (1967) says that there exists no theory for predicting damage to be expected under given service conditions. A large number of papers and reports on this subject has been published over the past few years and many of them have contributed toward a better qualitative understanding of the mechanism of rain erosion and its relationship to material properties, although most of them have been limited to velocities less than 1000 ft/sec. These papers have included a great deal of experimental data and considerable theoretical work. Many of the theories, however, have been rigorously deduced from rather arbitrary assumptions. Contradictory empirical relations have been formulated. One only needs to read the discussions following many of the papers published in the proceedings of various rain erosion conferences to see that there is much disagreement among those who are working on this problem. There is considerable disagreement as to the forces that are actually responsible for the erosion and cratering resulting from a liquid-solid interaction. According to Eisenberg (1969), "There remains the mystery of which mechanism, shock waves or jet formation, is responsible for actual damage." Engle (1957), Fyall (1970), and others believe that the damage is produced by the introduction of shear and tensile stresses as a consequence of the high localized compressive forces exerted by the liquid.

Regimes of Impact Velocity

The various theories may not be as contradictory as they first
appear. In the case of solid-solid impact, there are at least three,
and perhaps four, regimes of the impact phenomena as the projectile
velocity increases. These are illustrated by the rather idealized
curve Figure 1.1 which shows the effect of velocity upon the penetrat-
ing power of projectiles into a ductile target. In the low-velocity
regime the penetration is strongly influenced by the strength of the
two materials. In this regime the penetration appears to increase as
the $4/3$ power of the velocity. A negligible amount of the projectile
energy is converted into stress waves. As the projectile velocity is
increased there is greater deformation and fragmentation of the pro-
jectile. At some point there is no increase in crater depth with ir-
creased velocity; in fact the depth actually decreases although the
crater volume may continue to increase. There comes a point where the
depth begins to again increase with velocity. The crater becomes more
hemispherical in shape and the penetration is now roughly proportional
to the $2/3$ power of the velocity. It is clear that a transition regime
has been crossed. The new regime is usually called the hypervelocity-
impact stage. The most common criterion for the beginning of this re-
gime is when the ratio of projectile velocity to that of a stress wave
in the target material exceeds unity. At these velocities the stresses
developed by the projectile's deceleration is much greater than the
yield strength of either the projectile or target and the materials'
densities affect the cratering process more than that of its other
properties (mechanical properties such as target and projectile strengths).
If the velocity is further increased, an impact regime is reached that is,

as yet, relatively unexplored. It is called the regime of impact explo-
sions, for the tremendous amount of energy becomes sufficient to vaporize
both the projectile and a small volume of the target. The partitioning
of the projectile's kinetic energy among such items as mechanical defor-
mation, heat generated, stress waves, ejected material, and perhaps vapor-
ization; the influence of material properties; the effects of stress waves;
and the mechanism of penetration and cratering are entirely different for
the various impact regimes. It is apparent that there are also different
mechanisms of erosion and cratering for liquid-solid impacts at various
velocities. Wheelahan (1967) points out that in the velocity range of
1000 to 3000 ft/sec, erosion rather than cratering is the dominant form
of damage, but as the impact velocity is increased above a few Mach num-
bers the damage is primarily by cratering. Somewhere between these two
types of damage there is obviously a regime of transition. Those appar-
ently contradicting models mentioned may not be contradictory at all but
each may apply at various impact velocities and for different materials.
For a particular target material the velocity-damage curves would be very
different for liquid and solid projectiles but would probably converge
in the hypervelocity range. If this be true, it will be possible to simu-
late the higher velocity liquid impacts with solid projectiles. This
would probably be at a higher velocity than is presently of interest in
the study of rain damage to high-speed aircraft and missiles. For example,
the hypervelocity regime of aluminum starts at a velocity greater than
20,000 ft/sec.

Although much research has gone into the accumulation of information
now available relative to high-speed liquid impact, it is obvious that
there is much more to be done. Mathematical models must be derived that

take into account the effects of the various material properties including hardness, density, elastic modulus, yield strengths, fracture strengths, and Poisson's ratio, as well as surface conditions and porosity; the fracture criteria for various materials, both ductile and brittle; the effects of drop size and angle of impact; the effects of target temperature; the impact pressures and radial flow distribution and duration; the effects of cavitation; and the momentum and energy imparted to the target. When it is realized that this must be done for the entire range of velocities, including the various regimes previously discussed, it is apparent that much is yet to be learned relative to liquid impacts. This will require the exchange of ideas among all investigators in this field of research. There will continue to be conflicting theories but controversy always stimulates research.

Scope of the Investigation

Although the rain field may be defined in terms of drop size, distribution, velocity, direction, and duration, it cannot be assumed that this describes the conditions between the shock wave and the target surface, which in this study is a conical nosecone. It has been suggested that water drops passing through the shock wave may be fragmented, slowed down, and turned before impacting the target. The shattering or fragmenting will not have an effect if the time to traverse the shock layer is less than the breakup time. If the deflection angles are of significant magnitude, the total number of impacts will be reduced. If the raindrops have sufficient momentum to prevent them from being deflected, all raindrops in the path of the nosecone will impact. Section II of this report is an analysis of the motion of raindrops in conical shock layers.

Two damage-producing attributes of liquid-drop impact are: (a) the impact pressure, and (b) the sheet jet produced by the radial liquid flow. Section III deals with the mechanisms of cratering and erosion resulting from these forces.

A third source of damage resulting from impact is the stress wave. This wave may contribute to fractures at or near the point of impact, or may produce damage by reflection from the target's rear surface. These fractures produced by reflected stress waves will generally be some distance from the point of impact and when they occur they may be more damaging than material failure in or near the impact area. This is an important problem as it may dictate the required nosecone thickness. It is analyzed in Section IV.

This investigation includes only a small amount of experimental work. A water jet accelerator was constructed and targets of Lucite and slip-cast fused silica were impacted. A description of the equipment and an analysis of the craters and fractures constitute Section V.

Finally, an SCFS nosecone was examined after travel through a rainfield at Holloman Air Force Base and a description of the resulting damage is included in Section VI.

A brief description of proposed future work is given in Section VII.

As the various sections of this report were prepared by different individuals, some variations in symbols and forms of equations will be found; however, the meanings of all symbols are defined in the text and no confusion on the part of the reader should result.

SECTION II.

MOTION OF RAINDROPS IN A HYPERSONIC SHOCK LAYER

Introduction

In order to estimate the rain-erosion damage that will occur when a vehicle flies through a rain field it is first necessary to know the relative velocities with which the rain drops strike the vehicle surface and the distribution of drops along the surface. The theoretical determination of these quantities is the subject of this section. In order to compute these quantities it is assumed in the present work that the cloud of drops can be treated as a quasi-continuous gas-like material. This model is accurate when a representative volume element of the air-drop mixture, small compared to the characteristic dimensions of the flow field, contains a sufficient number of drops to allow meaningful averages of the drop properties to be formed over the volume element. These averages are then treated macroscopically as continuous variables and the small volume is assumed to have the mathematical properties of a differential element. Thus the air-drop mixture is viewed, for the purposes of macroscopic analysis, as a mixture of two continuous fluid-like materials. General discussions of the governing equations appropriate to such two-phase flows are given in the books by Wallis (1969) and Soo (1967) and the review article by Marble (1970).

In the present work several assumptions have been used to develop the governing equations to be discussed subsequently. These are the subject of this paragraph. First, it is assumed that the presence of the drops has an insignificant effect on the motion of the gas phase. This assumption is justified when the mass fraction of the dispersed phase is small.

This condition is invariably satisfied in shock layers. Second, it is assumed that the volume fraction of the drop phase is small enough so that the interphase mass, momentum, and heat transfer laws can be evaluated using formulas appropriate for a single particle. This requirement is more stringent than the first one but it appears to be satisfied in most shock layers. Third, it is assumed that collisions between drops are sufficiently rare so that the drop-phase stress tensor can be ignored. Finally, it is assumed that the drops can be modeled, with sufficient accuracy, as identical spheres characterized by a single effective mass and radius, both of which are independent of time. Thus mass loss by the drops is not explicitly accounted for. Mass loss can occur by two mechanisms: evaporation and breakup. In a state-of-the-art survey Wheelahan (1967) stated that neither of the mechanisms appeared to be important. A set of equations including evaporation effects is given by Marble (1970) (see also Panton (1968), Panton and Oppenheim (1968), and Lu and Chiu (1966)). An order-of-magnitude analysis of these equations was carried out in the course of the present work and tended to confirm the belief that loss of mass due to evaporation is negligible. Recent experimental research on drop breakup (see, for instance, Waldeman, Reinecke, and Glenn (1972)) indicates that the mass loss associated with this phenomenon can be appreciable at high Mach numbers. Unfortunately the existing experimental data has not yet been put in a form suitable for incorporation in the theory to be subsequently discussed. An expression relating the rate at which mass is lost by a single drop to the parameters of the flow of the gas relative to the drop is required. To date, no such relationship has appeared in the

literature. Thus drop breakup cannot be considered explicitly. A possible way of correcting the theory for drop breakup will be discussed later.

Previous investigations along the lines of the present work are limited to the following papers. Probstein and Fassio (1970) computed the drop-phase velocity field and streamline pattern for shock layers on thin wedges and cones and in the stagnation regions of cylinders and spheres. They employed the constant density approximation to determine the gas flow field. For the wedge they obtained results in closed form while numerical integration was necessary to solve the equations in the other cases. Waldeman and Reinecke (1971) obtained results for the velocity field and streamline pattern for flow past a cone and a sphere. They relaxed the constant density assumption invoked by Probstein and Fassio (1970) but solved the governing equations for the drop phase approximately by a perturbation method. Both of these reports also gave results for the collection efficiencies of the various body shapes analyzed in them. (The collection efficiency is defined to be the ratio of the actual rate at which mass is removed from the drop phase by collection of drops on the body surface to the rate that would exist if the motion of the drop phase were entirely unaffected by the presence of the shock layer.) Further collection efficiency calculations were made by Spurk and Gerber (1972) who considered cones and slender power-law axisymmetric bodies.

In the present work the drop-phase velocity field, streamline pattern, density distribution, and temperature distribution are computed for conical shock layers. Since the collection efficiency seems to have little relevance to radome design, no results for this quantity are

presented. These calculations should be representative of the conditions occurring in radome shock layers because the results of Spurk and Gerber (1972) show that small deviations from a perfectly conical body shape produce insignificant changes in the flow variables of the dispersed phase. The solutions are obtained numerically and results are presented graphically to illustrate various parametric trends. In addition, some results are given for shock layers on wedges. While such calculations have no direct application to radome technology, the wedge is a useful test case because the gas-phase flow field has an especially simple form. In fact, by invoking the thin-shock-layer approximation it is possible to obtain solutions in closed form for this case. This process was begun by Probstein and Fassio (1970) and is completed in the present work.

Governing Equations

The appropriate governing equations for analysis of the behavior of the drop phase are found from balances of mass, linear momentum, and energy. These are respectively

$$\rho_{p,t} + \vec{\nabla} \cdot (\rho_p \vec{u}_p) = 0$$

$$\rho_p(\vec{u}_{p,t} + \vec{u}_p \cdot \vec{\nabla} \vec{u}_p) = \vec{P}$$

$$\rho_p(e_{p,t} + \vec{u}_p \cdot \vec{\nabla} e_p) = S \qquad (2.1)$$

where (2.1a) results from balance of mass, (2.1b) from balance of linear momentum, and (2.1c) from balance of energy; ρ_p is the drop-phase mass density, $\vec{u}_p$ is the drop-phase velocity vector, e_p is the drop-phase internal energy, $\vec{P}$ is the force per unit volume applied to the drop phase by the gas phase, S is the heat per unit volume transferred to the drop phase by the gas phase, $\vec{\nabla}$ is the gradient operator, t is time, and a

comma denotes partial differentiation with respect to the following
subscript. To render (2.1) determinate constitutive equations for e_p,
$\vec{P}$, and S are required. For the internal energy it is assumed (see
Marble (1970)) that

$$e_p = c_p T_p \tag{2.2}$$

where c_p is the heat capacity of the dispersed phase and T_p is its tem-
perature. Two sets of momentum and heat supply terms are used in the
present work. The first is (with $\vec{u}$ denoting the fluid-phase velocity vector)

$$\vec{P} = -(\rho_p/\tau_1)|\vec{u}_p-\vec{u}|^{1-b}(\vec{u}_p-\vec{u})$$

$$S = -(\rho_p c/\tau_2)(T_p-T) \tag{2.3}$$

where c is the specific heat at constant pressure of the gas phase,
b is a numerical factor, and τ_1 and τ_2 are momentum and thermal relaxation
factors defined as

$$\tau_1 = 2^{1+b} /Na^{2-b}\rho^{1-b}\mu^b$$

$$\tau_2 = mc/4\pi a\kappa \tag{2.4}$$

In (2.4) N is a numerical factor, m is the mass and a is the radius of
a representative spherical particle, ρ is the gas-phase density, μ is
the gas-phase viscosity, and κ is the gas-phase thermal conductivity.
The relative Reynolds number is

$$R = (2a\rho/\mu)|\vec{u}_p-\vec{u}| \tag{2.5}$$

Its value determines the numerical factors b and N as follows.

$$0 < R < 1 \quad : \quad b = 1, \ N = 24$$

$$1 < R < 1000 \quad : \quad b = 0.6, \ N = 24$$

$$1000 < R < \infty \quad : \quad b = 0, \ N = 0.44 \tag{2.6}$$

Equation (2.3a) is obtained by dividing the standard drag curve for
steady flow past a sphere into three parts and fitting an equation to

each part as described by Probstein and Fassio (1970). It is assumed in the present work that the only significant contribution to the inter-phase force is the steady state drag. This is known to predominate the drag due to added mass and that due to unsteady motion in most cases. Lift forces were included in some of the calculations made in the course of the present work and were found to have a negligible effect. Equation (2.3b) results from the pure-conduction heat transfer law for a single sphere. Equations (2.3) have a convenient analytical form which facilitated the determination of the exact solution referred to previously. These equations were useful in checking the computer program developed in the present work.

The second set of drag and heat transfer laws used is

$$\vec{P} = -(\rho_p/\tau_1)(1 + (64/R^{4/5}))|\vec{u}_p - \vec{u}|(\vec{u}_p - \vec{u})$$

$$S = -(\rho_p c/\tau_2)(1 + (3/10)R^{1/2}Pr^{1/3})(T_p - T) \qquad (2.7)$$

where all symbols previously defined retain their meanings with the stipulation that b be set equal to zero in (2.4a). In (2.7b) Pr is the Prandtl number defined by

$$Pr = \mu c/\kappa \qquad (2.8)$$

Formulas of the form of (2.7) have been proposed by many authors (see, for instance, Panton (1968)) with slightly different values of the coefficients and exponents and are known to be reasonably accurate over a wide range of Reynolds and Prandtl numbers.

Thin Shock Layers on Wedges[*]

Consider a wedge of surface length L and half-angle θ_b. The free-stream velocity is U_∞ and the ratio of the gas-phase density before the shock to that after the shock is ϵ. The density of the gas phase and the

---

[*]A shortened account of this work is contained in Peddieson and Lyu (1973).

drop phase just behind the shock are ρ_s and $\rho_{p\infty}$ respectively. The free-stream temperature of the mixture is T_∞. It is convenient to use cartesian coordinates x and y with x measured parallel to the body surface and y measured normal to it. It is convenient to define dimensionless variables as follows.

$$s = x/L, \quad n = y/L$$

$$F\vec{e}_s + G\vec{e}_n = \vec{u}/U_\infty, \quad F_p\vec{e}_s + G_p\vec{e}_n = \vec{u}_p/U_\infty \tag{2.9}$$

$$Q = \rho/\rho_s, \quad Q_p = \rho_p/\rho_{p\infty}$$

$$H = T/T_\infty, \quad H_p = T_p/T_\infty \tag{2.10}$$

where $\vec{e}_s$ and $\vec{e}_n$ are unit vectors associated with the s and n axes. Substituting (2.9) and (2.10) into (2.1), (2.2), and (2.3) (equations (2.3) are used initially because their forms facilitate the subsequent analytical work), and substituting (2.2) and (2.3) into (2.1) results in

$$(Q_p F_p)_{,s} + (Q_p G_p)_{,n} = 0$$

$$F_p F_{p,s} + G_p F_{p,n} = \alpha_1((F-F_p)^2 + (G-G_p)^2)^{(1-b)/2}(F-F_p)$$

$$F_p G_{p,s} + G_p G_{p,n} = \alpha_1((F-F_p)^2 + (G-G_p)^2)^{(1-b)/2}(G-G_p)$$

$$F_p H_{p,s} + G_p H_{p,n} = \alpha_2(H-H_p) \tag{2.11}$$

where

$$\alpha_1 = L/\tau_1 U_\infty^b, \quad \alpha_2 = (L/\tau_2 U_\infty)(c/c_p) \tag{2.12}$$

The gas flow variables are modeled by the inviscid solution for supersonic flow past a wedge. This solution is known exactly and for a thin shock layer (which occurs when θ_b and ϵ are small) has the form

$$F = 1, \quad G = 0, \quad H = H_s, \quad Q = 1 \tag{2.13}$$

where the subscript s denotes the value of the variable on the downstream side of the shock wave. The shock wave is known to be a straight line making an angle (for a thin shock layer)

$$\theta_s = \theta_b/(1 - \epsilon) \tag{2.14}$$

with the centerline of the wedge. The solution of (2.11) must satisfy the conditions

$$F_p = 1, \quad G_p = -\theta_b, \quad H_p = 1, \quad Q_p = 1 \tag{2.15}$$

on the shock wave which is the line

$$n = (\theta_s - \theta_b)s \tag{2.16}$$

This problem is most easily solved using a Von Mises transformation familiar from boundary-layer theory. This is done by defining a stream function ψ_p such that

$$\psi_{p,s} = -Q_p G_p, \quad \psi_{p,n} = Q_p F_p \tag{2.17}$$

and converting the independent variables from s and n to ψ_p and z where $z = n$. The total differential of ψ_p is

$$d\psi_p = \psi_{p,s}ds + \psi_{p,n}dn = -Q_p G_p ds + Q_p F_p dn \tag{2.18}$$

Solving (2.18) for ds yields

$$ds = -(1/Q_p G_p)d\psi_p + (F_p/G_p)dz \tag{2.19}$$

Now regarding s as a dependent variable which is a function of ψ_p and z it is clear that

$$s,_\psi = -1/Q_p G_p, \quad s,_z = F_p/G_p \tag{2.20}$$

Converting the derivatives in (2.11b,c,d) and rewriting (2.20b) one obtains

$$G_p F_{p,z} = \alpha_1((1-F_p)^2 + G_p^2)^{(1-b)/2}(1-F_p)$$

$$G_p G_{p,z} = -\alpha_1((1-F_p)^2 + G_p^2)^{(1-b)/2}G_p$$

$$G_p H_{p,z} = \alpha_2(H_s - H_p)$$

$$G_p s,_z = F_p \tag{2.21}$$

where (2.13a,b,c) have been used. Substituting (2.15a,b,d) and (2.16) into (2.18), integrating along the shock wave, and assuming $\psi_p(0,0) = 0$ yields

$$\psi_p = \theta_s z_s/(\theta_s - \theta_b) \tag{2.22}$$

It is convenient to replace ψ_p by z_s as one of the independent variables. When this is done (2.20a) reads

$$Q_p = -\theta_s/((\theta_s - \theta_b)G_p s_{,z_s}) \qquad (2.23)$$

The initial conditions are

$$F_p = 1, \quad G_p = -\theta_b, \quad H_p = 1, \quad s = z_s/(\theta_s - \theta_b) \qquad (2.24)$$

on $z = z_s$. Since equations (2.21) contain no derivatives with respect to z_s they can be integrated like ordinary differential equations along the streamlines (lines of constant z_s). The dependence of the solution on z_s enters through the application of the boundary conditions. For all values of b the solution for the tangential velocity is

$$F_p = 1 \qquad (2.25)$$

The other variables have different forms depending on the value of b. They are

$b = 1$:

$$s = (z_s/(\theta_s - \theta_b)) - (1/\alpha_1)\log(1 - (\alpha_1/\theta_b)(z_s - z))$$

$$G_p = -\theta_b + \alpha_1(z_s - z)$$

$$H_p = H_s - (H_s - 1)(1 - (\alpha_1/\theta_b)(z_s - z))^{\alpha_2/\alpha_1}$$

$$Q_p = 1/(1 - (\theta_b/\theta_s)(1 - (\alpha_1/\theta_b)(z_s - z))) \qquad (2.26)$$

$b = 0.6$:

$$s = (z_s/(\theta_s - \theta_b)) - (5/2\alpha_1\theta_b^{2/5})(1 - (1 - (3\alpha_1/5\theta_b^{3/5})(z_s - z))^{-2/3})$$

$$G_p = -\theta_b(1 - (3\alpha_1/5\theta_b^{3/5})(z_s - z))^{5/3}$$

$$H_p = H_s - (H_s - 1)\exp(-(5\alpha_2/2\alpha_1\theta_b^{2/5})((1 - (3\alpha_1/5\theta_b^{3/5})(z_s - z))^{-2/3} - 1))$$

$$Q_p = 1/(1 - (\theta_b/\theta_s)(1 - (1 - (3\alpha_1/5\theta_b^{3/5})(z_s - z))^{5/3})) \qquad (2.27)$$

$b = 0$:

$$s = (z_s/(\theta_b - \theta_s)) - (1/\theta_b\alpha_1)(1 - \exp(\alpha_1(z_s - z)))$$

$$G_p = -\theta_b \exp(-\alpha_1(z_s - z))$$

$$H_p = H_s - (H_s - 1)\exp(-(\alpha_2/\alpha_1\theta_b)(\exp(\alpha_1(z_s - z)) - 1))$$

$$Q_p = 1/(1 - (\theta_b/\theta_s)(1 - \exp(\alpha_1(z_s - z)))) \qquad (2.28)$$

Results equivalent to (2.26a,b), (2.27a,b), and (2.28a,b) have been given by Probstein and Fassio (1970). They used a Lagrangian description. The temperature and density results are new. The use of an Eulerian description facilitates the determination of the drop-phase density. These results were used as a check on the numerical calculations to be described subsequently and a check on the approximate analytical solutions discussed in Appendix 1.

Numerical Solutions for Thin Shock Layers

In this sub-section the symbol j is introduced to differentiate between plane and axisymmetric flow. For the former $j = 0$ while for the latter $j = 1$. The discussion will be for the conical case but the resulting equations are also valid for wedge flows if j is set equal to zero.

For numerical work it was found convenient to use a system of polar coordinates r and θ with $r = 0$ at the leading edge of the body and $\theta = 0$ on the axis of symmetry of the cone. Defining the dimensionless variables

$$\xi = r/L, \quad \eta = \theta$$

$$F\vec{e}_\xi + G\vec{e}_\eta = \vec{u}/U_\infty, \quad F_p\vec{e}_\xi + G_p\vec{e}_\eta = \vec{u}_p/U_\infty \qquad (2.29)$$

where $\vec{e}_\xi$ and $\vec{e}_\eta$ are unit vectors associated with ξ and η, substituting (2.29) and (2.10) into (2.1), (2.2), and (2.3) and substituting (2.2) and (2.3) into (2.1) yields

$$(\xi(\xi\eta)^j Q_p F_p)_{,\xi} + ((\xi\eta)^j Q_p G_p)_{,\eta} = 0$$

$$F_p F_{p,\xi} + (G_p/\xi)F_{p,\eta} - (G_p^2/\xi) = \alpha_1((F-F_p)^2 + (G-G_p)^2)^{(1-b)/2}(F-F_p)$$

$$F_p G_{p,\xi} + (G_p/\xi)G_{p,\eta} + (F_p G_p/\xi) = \alpha_1((F-F_p)^2 + (G-G_p)^2)^{(1-b)/2}(G-G_p)$$

$$F_p H_{p,\xi} + (G_p/\xi)H_{p,\eta} = \alpha_2(H_s-H_p) \qquad (2.30)$$

The gas flow variables are modeled by the constant density approximation (see Probstein and Fassio (1970))

$$F = 1, \quad G = -(2(\eta-\theta_b))^j, \quad H = H_s, \quad Q = 1 \tag{2.31}$$

(Note that, within the thin-shock-layer approximations, these expressions are exact for $j = 0$.) The shock wave is a cone making an angle

$$\theta_s = \theta_b/(1 - (\epsilon/2^j)) \tag{2.32}$$

with the axis of symmetry. The conditions

$$F_p = 1, \quad G_p = -\theta_s, \quad H_p = 1, \quad Q_p = 1 \tag{2.33}$$

must be satisfied on the shock wave.

Again it is useful to employ a Von Mises transformation. Defining a stream function ψ_p such that

$$\psi_{p,\xi} = -(\xi\eta)^j Q_p G_p, \quad \psi_{p,\eta} = \xi(\xi\eta)^j Q_p F_p \tag{2.34}$$

and converting to the independent variables ψ_p and $z = \eta - \theta_b$ one obtains

$$G_p F_{p,z} - G_p^2 = a_1 \xi((1 - F_p)^2 + ((2z)^j + G_p)^2)^{(1-b)/2}(1 - F_p)$$

$$G_p G_{p,z} + F_p G_p = -a_1 \xi((1-F_p)^2 + ((2z)^j + G_p)^2)^{(1-b)/2}((2z)^j + G_p)$$

$$G_p H_{p,z} = a_2(H_s - H_t)$$

$$G_p \xi_{,z} = \xi F_p$$

$$Q_p = -1/((\xi(z + \theta_b))^j G_p \xi_{,\psi_p}) \tag{2.35}$$

The relationship between ψ_p and ξ_s the shock position where a streamline originates is easily found using (2.34) to be

$$\psi_p = (\theta_s^{1+j}/(1+j))\xi_s^{1+j} \tag{2.36}$$

Using this expression (2.35) can be written as

$$Q_p = -(\xi_s/\xi)^j(\theta_s/(z + \theta_b))^j(\theta_s/G_p \xi_{,\xi_s}) \tag{2.37}$$

Equations (2.35a,b,d) were numerically integrated simultaneously along various streamlines using a fourth-order Runge-Kutta algorithm. Since each streamline represents a line of $\xi_s = $ a constant, the partial derivatives with respect to z can be treated as ordinary derivatives in this calculation. After the determination of F_p, G_p, and ξ (2.35c) was integrated

using a fourth-order Runge-Kutta method to obtain H_p and Q_p was obtained from (2.37) where the derivative with respect to ξ_s was approximated by a two-point backward difference. A discussion of the numerical results obtained by this method is the subject of the next three paragraphs.

Figures 2.1 and 2.2 show the distribution of the drop-phase normal velocity and the drop-phase density along the vehicle surface. These calculations are for a vertex half-angle $\theta_b = 0.1$ and a gas density ratio $\epsilon = 0.1$. Results are plotted for various values of the dimensionless drag parameter α_1. These results are for the linear drag law $b = 1$. Figure 2.1 pertains to wedges while Figure 2.2 pertains to conical shock layers. It can be seen that for small values of the drag parameter the drop-phase normal velocity and the drop-phase density are nearly constant along the surface. This represents a situation in which the motion of the drops is almost unaffected by the presence of the shock layer. As α_1 increases significant deviations from the free-stream values of the variables quickly become apparent. It is clear that this effect is greater for the wedge than for the cone. Figure 2.1 represents either the numerical solution or the analytical solution represented by (2.26a,d). For the step sizes used in this work ($\Delta\xi_s = .005$, $\Delta z = ((\theta_s - \theta_b)/100)$) it was found that the numerical and analytical solutions were indistinguishable. Reductions in the step sizes failed to produce any change in the solution variables.

Figures 2.3 through 2.8 present further results for the problem discussed in the previous paragraph. The distributions of various variables are plotted along selected streamlines. The parameter $\psi = \xi_s/(9(1+j))$ increases as the distance from the origin of the streamline to the nose

increases. Figures 2.3 and 2.4 show the variation of the normal velocity with z for two values of α_1. On the streamlines close to the nose of the vehicle the particles are slowed down the least. The drag becomes increasingly more effective as the distance from the nose increases. This trend becomes more pronounced as α_1 becomes larger. As the normal velocity is decreased along a given drop-phase streamline the drop-phase density increases. This is shown in Figures 2.5 and 2.6. The increases in density are larger for plane flow than for axisymmetric flow and become steadily larger as the value of dimensionless drag coefficient is raised. Figures 2.7 and 2.8 depict selected drop-phase streamlines. The streamlines are slightly deflected downstream by the action of the interphase drag. This effect is accentuated as the distance of the origin of the streamline from the nose increases and as α_1 increases. The radial velocity F_p has not been plotted because its value was found to be very close to unity for all the calculations discussed here.

Figure 2.9 shows some comparisons of the results obtained in different drag regimes (different values of b) for $\theta_b = 0.1$ and $\varepsilon = 0.1$. Obviously the sensitivity of the solution variables to the value of b increases as α_1 increases because b is contained only in the drag terms whose magnitude is determined by the value of α_1. It is clear from the plotted data that for $\alpha_1 = 10$ significantly different values of the flow variables exist in different regions of the standard drag curve. For thin shock layers it is reasonable to assume that one drag law will be applicable throughout the flow field. This has been verified by the calculations of Spurk and Gerber (1972). Calculations of the type described in the previous two paragraphs were carried out for the cases of b = 0.6 and b = 0. Since

the results were qualitatively similar to those already discussed they are not presented graphically.

Numerical Solutions for General Conical Shock Layers

It is now desired to eliminate any assumption that either the cone or the shock layer is thin. Since this implies that a wide range of relative Reynolds numbers may be encountered by a typical drop as it traverses the shock layer, it is appropriate to use the drag and heat transfer laws given by (2.10). The governing equations (2.30) are now replaced by

$$(\xi^2 \sin(\eta) Q_p F_p)_{,\xi} + (\xi \sin(\eta) Q_p F_p)_{,\eta} = 0$$

$$F_p F_{p,\xi} + (G_p/\xi) F_{p,\eta} - (G_p^2/\xi) = \alpha_1 \xi Q(1 + (64/(\alpha_3 Q((F-F_p)^2 + (G-G_p)^2)^{1/2})^{4/5}))((F-F_p)^2 + (G-G_p)^2)^{1/2}(F-F_p)$$

$$F_p G_{p,\xi} + (G_p/\xi) G_{p,\eta} + (F_p G_p/\xi) = \alpha_1 \xi Q(1 + (64/(\alpha_3 Q((F-F_p)^2 + (G-G_p)^2)^{1/2})^{4/5}))((F-F_p)^2 + (G-G_p)^2)^{1/2}(G-G_p)$$

$$F_p H_{p,\xi} + (G_p/\xi) H_{p,\eta} = \alpha_2 \xi (1 + (3Pr^{1/3}/10)(\alpha_3 Q((F-F_p)^2 + (G-G_p)^2)^{1/2})^{1/2})(H-H_p) \tag{2.38}$$

where α_1 is given by (2.12) with $b = 0$ and ρ replaced by ρ_s in the equation defining τ_1 (equation (2.4a) with $b = 0$) and $\alpha_3 = (2aU_\infty \rho_s)/\mu$. Note that α_3 has the form of a Reynolds number based on the free-stream velocity, the effective particle radius, the gas density just behind the shock, and the gas viscosity. The gas flow variables are modeled as follows.

$$F = \cos(\theta_s) - a_1(1 - (\theta/\theta_s))$$

$$G = -a_2(\sin(\theta_s)/\theta_s)(\theta-\theta_b)$$

$$Q = 1 + a_3(1 - (\theta/\theta_s))$$

$$H = H_s + a_4(1 - (\theta/\theta_s)) \tag{2.39}$$

Equations (2.39a,b,c) were obtained by Waldman and Reinecke (1971) by fitting linear functions to existing theoretical and experimental data for the gas flow field. Equation (2.39d) was obtained the same way in the course of the present work. Representative values of the constants contained in (2.38) are $a_1 = 0$, $a_2 = 1.67$, $a_3 = 0.35$, $a_4 = 4.0$. Calculations carried out in the course of this work showed that the drop-phase flow variables were rather insensitive to the values of the a's. The shock angle is computed (following Waldman and Reinecke (1971)) from the formula

$$\theta_s = \theta_b / (1 - (\epsilon/a_2)) \tag{2.40}$$

The boundary conditions to be satisfied on the shock ($\theta = \theta_s$) are

$$F_p = \cos(\theta_s), \quad G_p = -\sin(\theta_s), \quad H_p = H_s, \quad Q_p = 1 \tag{2.41}$$

In this case the drop-phase stream function defined so that

$$\psi_{p,\xi} = -\xi \sin(\eta) Q_p G_p, \quad \psi_{p,\eta} = \xi^2 \sin(\eta) Q_p F_p \tag{2.42}$$

and the modified governing equations (2.35) are replaced by

$$G_p F_{p,z} - G_p^2 = \alpha_1 \xi Q (1 + (64/(\alpha_3 Q((F-F_p)^2 + (G-G_p)^2)^{1/2})^{4/5}))((F-F_p)^2 + (G-G_p)^2)^{1/2}(F-F_p)$$

$$G_p G_{p,z} + F_p G_p = \alpha_1 \xi Q (1 + (64/(\alpha_3 Q((F-F_p)^2 + (G-G_p)^2)^{1/2})^{4/5}))((F-F_p)^2 + (G-G_p)^2)^{1/2}(G-G_p)$$

$$G_p H_{p,z} = \alpha_2 \xi (1 + (3Pr^{1/3}/10)(\alpha_3 Q((F-F_p)^2 + (G-G_p)^2)^{1/2})^{1/2})(H-H_p)$$

$$G_p \xi_{,z} = \xi F_p$$

$$Q_p = -1/(\xi \sin(z + \theta_b) G_p \xi_{,\psi_p}) \tag{2.43}$$

Equation (2.36) is replaced by

$$\psi_p = ((\sin(\theta_s))/2) \xi_s^2 \tag{2.44}$$

This relationship can be used to rewrite (2.43e) as

$$Q_p = -(\xi_s/\xi)(\sin(\theta_s)/\sin(z+\theta_b))(\sin(\theta_s)/G_p \xi_{,\xi_s}) \tag{2.45}$$

Equations (2.43a,b,c,d) and equation (2.45) were solved numerically using the method discussed earlier. These solutions were found to be insignificantly different from those described earlier, for corresponding values of the parameters.

In order to carry out a parametric study a representative density ratio of $\varepsilon = 0.2$ was selected and used in all the calculations to be considered below. Figures 2.10 and 2.11 illustrate the influence of the parameter α_3 on the solution variables evaluated on the wall of the cone for $\theta_b = 0.1$. For large α_3 the quadratic drag law is approached and the solution is insensitive to α_3. As α_3 decreases the sensitivity of the solution to its value increases and large reductions in the drop-phase normal velocity and increases in the drop-phase density occur. The power of α_3 to influence the numerical results increases with increasing α_1.

Figures 2.12 through 2.17 depict the variation of the transverse velocity and the density along selected streamlines and the shapes of these streamlines for various values of α_3. The vertex half-angle for these cases is $\theta_b = 0.2$. The parameter $\psi = \xi_s/10$. It is evident that the variation of quantities from streamline to streamline is increased by decreasing α_3. For the data plotted in these figures there is little variation across the streamlines for any of the parametric values shown. Comparison of the results for $\alpha_3 = 10^5$ and $\alpha_3 = 10^9$ reveals that they are virtually identical indicating that the quadratic-drag-law asymptote to the standard drag curve has been attained.

Figures 2.18 through 2.20 show the influence of the cone half-angle θ_b on the surface values of the normal velocity and the density of the drop phase for various values of α_3. As the angle θ_b increases the

amount of variation of the flow variables along the surfaces decreases.
This trend is most apparent for $\alpha_3 = 10^2$. It is obvious that both the
normal velocity and the density of the drop phase are increasing functions
of the cone half-angle.

Figures 2.21 through 2.23 illustrate the influence of α_1 on the drop-
phase normal velocity and the drop-phase density at the vehicle surface
for $\theta_b = 0.4$ and various values of α_3. As discussed earlier small values
of α_1 lead to virtually constant distributions of G_p and Q_p along the
surface. As α_1 increases large variations in the values of the flow
variables at the wall appear. This effect is much more pronounced in
this case than it was for the thin shock layers discussed previously.
The largest variations occur for the smallest value of the Reynolds
number parameter α_3. Even for the larger values of α_3 significant varia-
tions of G_p and Q_p can occur.

Figures 2.24 through 2.29 present results for the streamline shapes
and the variations of the transverse velocity and the density of the drop
phase along selected streamlines for the same geometry discussed in the
previous paragraph. The streamline parameter $\psi = \xi_s/10$. In all cases it
can be seen that the variations of the plotted variables with z increases
as the distance of the streamline from the leading edge of the cone in-
creases. This trend becomes less prominent as α_3 is increased and more
prominent as α_1 is increased.

In all the cases discussed in the present work the temperature dis-
tributions were computed along with the other results that have been
discussed. Since the surface temperature distribution of the drop phase
does not now appear to be pertinent to design procedures for the preven-
tion of rain erosion damage this data was not presented graphically.

For drop sizes typical of those found in rain fields representative values of the dimensionless drag parameter $a_1 = L/\tau_1$ lie in the range $10^{-1} \leq a_1 \leq 1$ if $\tau_1 = m/(.22\pi\rho_s a^2) = 6.0 \cdot a(\bar{\rho}_p/\rho_s)$ ($\bar{\rho}_p$ is the density of the material contained in a single drop) is evaluated using the initial drop radius. It should be possible to account for breakup of the drops (when this occurs) by using an equivalent value of a which is smaller than the free-stream value. This would decrease τ_1 which would increase the dimensionless drag parameter a_1. As has been shown, this has the effect of decreasing significantly the computed velocity with which the drops strike the surface. It also appears to have the effect of increasing the surface density of the drop phase but it must be remembered that

$$\rho_p = mq \tag{2.46}$$

where q is the number of drops per unit volume. If m (and thus $\rho_{p\infty}$) is evaluated using the effective value of a the values of ρ_p on the wall will decrease even though those of Q_p increase. It should be possible to determine the effective values of a appropriate to various flow conditions by matching numerical solutions of the type discussed in the present report with experimental results.

Conclusion

In the present section a numerical procedure to compute drop-phase flow fields in shock layers has been developed. A computer program was written to carry out the calculations. The method was verified by comparison with an analytical solution for flow over a thin wedge. Numerical results were computed and presented graphically for various representative cases in order to illustrate various parametric trends. Further results, corresponding to a particular experimental setup were found. These will be discussed in Section VI.

SECTION III.

CRATERING AND EROSION MECHANISMS

Introduction

This part of the research is directed toward the development of a rational theory which will adequately predict the relationship between the impact velocity and pressure and the crater size in a given rain environment on a given material. A review of literature (for recent comprehensive surveys, see Heymann (1967) and Eisenberg (1970)) has shown that there have been many recent advances toward an understanding of liquid impact erosion. However, while an impressive amount of experimental data has been generated, most of the analytical models suggested have been phenomenological and not much work has been done toward the development of a physical theory for quantitative prediction of erosion damage. This is understandable in view of the very complex nature of the damage mechanism. The theoretical analysis described below is not in itself expected to quantitatively predict all the rain erosion characteristics of materials; nevertheless, it is hoped that it will provide a better understanding of the erosion mechanism and help identify the parameters that are important.

The models proposed in this study are based upon the assumption that for high speeds of impact, the initial pressure developed is high enough to liquefy the target material in the neighborhood of the impact area. Recent studies by Heymann (1969) have shown that initial pressures of several times the magnitude of "water-hammer pressure" are possible. At sufficiently high velocities of impact, therefore, these impact pressures are likely to exceed the mechanical strength of the

This section prepared by Dr. Vireshwar Sahai, Associate Professor of Engineering Science and Peter W. Hsu, Graduate Assistant

target material, making it behave like a liquid in the immediate
neighborhood of the point of impact.

Such a fluid-fluid impact model for high-velocity impacts was
first conceived by Öpik (1936). Recently this model was studied both
experimentally and analytically by Engel (1966, 1967). Her analytical
study, however, was semi-empirical, and it involved an arbitrary as-
sumption with regard to partition of the energy of the impinging drop.
It was assumed arbitrarily that half of this energy is imparted to
the target and the other half is retained by the drop.

The initial part of the present research was devoted to further
study of the Engel's model of rain erosion. It was hoped that it would
be possible to use a more rational basis for the determination of
energy partition than that used by Engel. It was soon realized, how-
ever, that the energy balance associated with liquid-solid impact is
very complex. Part of the kinetic energy of the impinging drop goes
to the lateral outflow, part is dissipated in the shock waves passing
through the drop and in the shearing associated with change of liquid
flow direction, and the remaining part is dissipated in the target
material. Consideration of all these energy terms made the problem
unwieldy, and attempts to refine Engel's model were subsequently
abandoned.

Instead it was found that incorporation of the concept of "appar-
ent mass," used by Ludloff (1967) in the treatment of hypervelocity
impacts of solids on solids, into the Opik-Engel model makes this model
more amenable for application to the rain erosion problem. Furthermore,
this concept allows the calculation of mass and energy of the ejecta
from the crater.

Before describing the apparent mass model, however, another fluid-fluid impact model based on an analogy with the impingement of a high-speed jet on a liquid surface will be considered. This model was extensively analyzed and has yielded good results. As pointed out by Cheslak, Nicholls, and Sichel (1969), the cavities formed by the impingement of high-speed jets on a liquid surface bear a striking resemblance to those formed on solid surfaces by high-speed impact. While high-speed jets are commonly used to simulate rain erosion (see, for example, Hammitt, et al (1967)), little work has been done to exploit this analogy.

Jet Model

As indicated earlier, this model is based upon the assumption that for high speeds of impact, the initial pressure developed is high enough to liquefy the target material allowing the impact to be categorized as a fluid-fluid impact. Based on the arguments of Plesset and Chapman (1971) and others, it is assumed, however, that the high contact pressure due to the initial impact decays very soon and is reduced to the stagnation level. The calculations of Plesset and Chapman showed that the duration of the stagnation pressure pulse is an order of magnitude higher than the period over which the initial water hammer pressure acts. They further expressed the opinion that this longer acting stagnation pressure pulse may be the primary source of damage caused by fluid impact.

Based upon the above-mentioned arguments, a simple idealized model of steady-state impingement of a cylindrical liquid jet on a liquid surface will be used. The drop is replaced by a cylindrical jet in order to simplify mathematical analysis. This simplification is prompted

by the fact that jets are often used with success to simulate rain
erosion. Because of its importance in industrial processes (such as
the oxygen conversion process in the steel industry), the jet impinge-
ment on liquid surfaces has been studied extensively both experimentally
and analytically. Some of this work is described below.

Banks and Chandrasekhara (1963) presented an experimental investi-
gation of normal penetration of a high-velocity gas jet through a liquid
surface. Banks and Bhavamai (1965) extended this study to a more general
one--experimental study of the impingement of a liquid jet on the surface
of a heavier liquid. Some 300 experiments were made to measure the sizes
of cavities formed due to impact of oil jets on water and water jets on
carbon tetrachloride.

From the viewpoint of the present application, the most useful ana-
lytical study of the problem is by Rossler and Stewart (1968). They de-
rived the governing differential equation for the cavity profile using a
steady-state force analysis. However, since their eventual purpose was
to explore the instability of the indention formed by the impact, they
did not verify their equation against experimental results such as those
cited above. In what follows, a general form of the Rossler-Stewart
equation, applicable to any given pressure and shear distribution on
the liquid surface, will be derived. After testing the theory against
experimental results of Banks and Bhavamai (1965) for the case of impact
of a liquid jet against a liquid surface, it will be applied to determine
the crater sizes in the high-speed impingements of water and mercury drops
against metals. Attempts will be made to determine the correspondence of
surface tension with some strength property of the target material. Experi-
mental results of Engel (1959, 1960) will be used for this purpose. An

approximate form of the Rossler-Stewart equation and its solution will
also be presented.

Governing Equations—It is assumed that the cavity formed by normal
impact is axisymmetric. The configuration of the cavity and the coordi-
nate system used are shown in Figure 3.1. The forces acting on an infin-
itesimal segment ds along the cavity profile are shown in Figure 3.2.
Here

P = pressure difference across the interface

τ = shear stress on the interface

σ = surface tension of the target liquid

w = weight of the impinging jet occupying the cavity

B = buoyant force

For the cavity to be in equilibrium, the sum of the vertical compo-
nents of these forces must vanish. Hence

$2\pi r ds \, p \cos\theta + 2\pi[r\sigma\sin\theta]_r$

$= 2\pi r ds \, \tau \sin\theta + 2\pi r dr(\rho_1 - \rho_2)gh + 2\pi[r\sigma\sin\theta]_{r+dr} = 0$

Here ρ_1 and ρ_2 are jet and target densities respectively, g is the gravi-
tational constant, and θ is the angle between ds and a horizontal line.
Noting that ds = dr/cosθ and taking the limit results in

$$p - \tau \tan\theta = (\rho_2 - \rho_1)gh + (\sigma/r)d/dr(r \sin\theta) \tag{3.1}$$

Finally, if the trigonometric relation tanθ = -dh/dr and a corresponding
one for sinθ are used, equation (3.1) becomes

$$h'' + (h'/r)[1+(h')^2] = (1/\sigma)[(\rho_2-\rho_1)gh-p-\tau h'][1+\tau(h')^2]^{3/2} \tag{3.2}$$

Here h and r are coordinates describing the cavity profile (see Figure 3.1a)
and the primes denote differentiation with respect to r. Equation (3.2) is
the governing equation for the cavity profile and is to be solved subject to
the following boundary conditions:

$h' = 0$ at $r = 0$ and at $r \to \infty$ both h' and $h \to 0$ (3.3)

Equation (3.2) is a highly nonlinear second order differential equation. The input information needed for its solution includes the two densities, the surface tension of the target fluid, and the pressure and shear distributions along the cavity profile. Unfortunately no analytical forms of pressure and shear distributions are available for high-speed impacts. Approximate forms based on experimental results will therefore be needed.

Before discussing the possible forms of pressure and shear distributions for the solution of equation (3.2), it will be convenient to nondimensionalize the equation. The following relationships are used for this purpose:

$$h^* = h/\beta R, \quad r^* = r/\beta R, \quad p^*/(\tfrac{1}{2}\rho_1 V^2), \quad \tau^* = \tau/(\tfrac{1}{2}\rho_1 V^2) \quad (3.4)$$

Here R is the jet radius, V is the impact velocity, and β is an adjustable nondimensional parameter chosen so that $r^* = 1$ will be the location of zero pressure point. The starred quantities are nondimensional. The dimensionless form of equation (3.2) can then be written as follows:

$$h^{*''} + (h^*/r^*)[1 + (h^{*'})^2] = [Ah^* - B(p^* + \tau^* h^{*'})][1 + (h^{*'})^2]^{3/\sim} \quad (3.5)$$

Here $A = [(\rho_2-\rho_1)g\beta^2 R^2]/\sigma$ and $B = (\tfrac{1}{2}\rho_1 V^2 \beta R)/\sigma$. A and B are both dimensionless parameters. Approximate forms of the pressure and shear distributions will now be described in terms of the new dimensionless variables.

Pressure Distribution--In view of the assumptions stated above, the form of pressure distribution needed is that for steady-state impact of a liquid jet on a flat surface. B anks and Chandrasekhara (1963) used a normal distribution

$$p^* = \exp(-Kr^{*2}) \quad (3.6)$$

which served as a fair approximation to the measured data of Gibson (1934).
This distribution, however, does not take the possible negative pressure
near the cavity edge into account. Rossler and Stewart (1968) used a
different distribution to fit Gibson's data, a modified form of which
is given by

$$p^* = F \sin(1-r^*)\pi/2 \tag{3.7}$$

$$\text{where } F = \begin{cases} 1 & , \ 0 \leq r^* < 1 \\ 0.015 \ (r^*-1), & 1 \leq r^* < 3 \\ 0 & , \ 3 \leq r^* \end{cases}$$

This sectionally continuous distribution does take the negative pressure
near the cavity edge into account. A conservation of momentum analysis
showed that the parameter β in the definition of $r^*(r^* = r/\beta R)$ must be
equal to 2.72. However, a value of $\beta = 2.0$ provides a better fit with
the experimental data of Gibson. The pressure distributions given by
equation (3.6) and equation (3.7) with $\beta = 2.0$ and $\beta = 2.72$ are compared
with Gibson's results in Figure 3.3a.

Another useful equation for pressure distribution is that by Leech
and Walker (1966). They carried out an extensive set of experiments and
fitted their results with the following polynomial:

$$p^* = 1 - 3r^{*2} + 2r^{*3}, \quad \beta = 2.6 \tag{3.8}$$

Their results however do not differ significantly from those of Gibson.
A pressure distribution which is close to that of Leech and Walker and
which takes negative pressures near the cavity edge into account is given
by the equation

$$p^* = (1 - r^{*2}) \exp(-r^{*2}), \quad \beta = 2.6 \tag{3.9}$$

The pressure distributions given by equations (3.7), (3.8), and (3.9) are
compared with each other in Figure 3.3b.

<u>Shear Distribution</u>--Banks and Chandrasekhara (1963) and Cheslak,
et al (1969) concluded from their experimental results that the viscosity
of the impinging jet has a negligible effect on stable cavities on liquid
surfaces. In the impact of drops on solid surfaces, however, the shear
stresses may not be negligible because the velocity of the lateral flow
is expected to be very large. To take the shear stresses into account,
the following approximate distribution suggested by Rossler and Stewart
(1968) will be used:

$$\tau^* = (\alpha^2)(0.664/Re_s^{\frac{1}{2}})\{1 - \exp[-(s/R)^2]\} \qquad (3.10)$$

Here $Re_s = \rho_1 \alpha Vs/\mu$ is the local Reynolds number based on the distance s
along the cavity profile. μ is the viscosity of the jet fluid. The
numerical factor α (to be called the shear factor) has been introduced
to take care of the possibility that the lateral flow velocity may be
larger than the normal impact velocity. In the case of liquid-solid
impacts, several experimenters (see, for example, Heymann (1967)) have
found the lateral flow velocity to be several times the velocity of impact.

<u>Numerical Solution</u>--A generalized program (for a listing of the pro-
gram, see Hsu (1972)) using a fourth-order Hamming's method based on an
interval-halving iterative technique was developed to solve the govern-
ing equations on a Xerox Sigma 6 computer. This program was used to
determine the cavity shapes and sizes in the case of jet impingement
on liquid surfaces as well as liquid drop impact on solid surfaces.

Because of the nonlinear nature of the governing equation and the
nature of the boundary condition made convergence difficult, several
subroutines were written to take care of the various difficulties. The
final form of the computer program seems to provide fast and stable con-
vergence in all cases under consideration.

-32-

Discussion of Results--First, the effect of various parameters in
the governing equation was investigated. For simplicity, the center
line velocity of the jet was assumed to remain unchanged upon impact,
thus neglecting the effect of jet spreading. The parameters used were
those for impact of an air jet on water. As shown in Figure 3.4, the
cavity depth increases with increasing velocity. When the velocity
exceeds a certain limit, the cavity shape is no longer shallow, and a
cavity lip is created. Both the cavity depth and the lip height con-
tinue to grow until a maximum cavity size is reached at a critical
velocity. Beyond this value the cavity depth starts to decrease while
the lip height continues to increase. It might be mentioned, however,
that the pressure distribution used becomes less and less accurate as
the cavity gets deeper.

In Figure 3.5, the effect of increasing the shear factor α on the
cavity size is presented. The shear factor seems to have a more signif-
icant influence on deep cavities than on shallow cavities. Note also
that the numerical solution is capable of providing the cavity profile
as well as the cavity depth. Figure 3.5 also shows the presence of a
cavity lip in the case of deep cavities.

Next, the effect of increasing the surface tension was investigated.
As expected, the depth of the cavity decreases as the surface tension is
increased. The effect of changing the parameter β in the pressure dis-
tribution will be discussed later.

The theory was then checked against experimental results of Banks
and Bhavamai (1965) for impacts of oil jets against water and water jets
against carbon tetrachloride. The effect of turbulent spreading of the
jet was taken into account in this case.

Figure 3.6 presents the results for the case of the impact of an oil jet on water. The coordinates used are the same as those used by Banks and Bhavamai. The ordinate h^*_{max} is the cavity depth nondimensionalized with respect to the jet elevation. The abscissa M^* represents nondimensional jet momentum. The experimental points of Banks and Bhavamai for various nozzle elevations are plotted on this graph. Also plotted are the calculated results of the present theory using pressure distribution equation (3.7) with $\beta = 2.72$ and $\beta = 2.0$. In view of the considerable scatter in the experimental data, the agreement seems to be satisfactory.

An empirical equation obtained by Banks and Bhavamai which fits their experimental data is compared with the present theory in Figures 3.7 and 3.8 for oil-water and water-carbon tetrachloride impacts respectively. The ordinate used here represents a normalized cavity depth defined in Banks and Bhavamai (1965) or Hsu (1972). Specific comparisons with experimental results showed that the higher value of β is better for cases of deep penetration while lower values of β are more suitable for shallow cavities.

This model was also applied to the case of the impact of a water drop on water surface. This case was considered by Engel (1966) as a model for high-speed liquid-solid impingements. In Figure 3.9, her experimental results are compared with those computed from the present theory. The agreement is satisfactory.

The fluid-fluid impact model was then applied to the impact of liquid drops on solid surfaces. The premise on which this model is based has already been discussed earlier. In this analysis, the pressure distributions given by both equations (3.7) and (3.9) were used,

but no significant difference was noted. As far as the shear distribution given by equation (3.10) is concerned, it was found that increasing the shear factor α to a value up to 4 does not significantly change the results; therefore, α was fixed at a value of 1. In fact, it was found that the shear term in equation (3.5) is small compared with other terms in the equation. Several workers (see, for example, Smith and Fyall (1969)) have found from their experiments that the shearing action resulting from the high-speed radial flow is not very significant.

One of the difficulties in applying the proposed model to liquid-solid impacts is that of relating the surface tension parameter σ to some strength property of the solid. It was fortunately found that the use of a simple relationship

$$S = \sigma/R, \tag{3.11}$$

where S is the dynamic yield strength of the target material and R is the drop radius, gives good correspondence with the available experimental results.

Figures 3.10, 3.11, 3.12, and 3.13 present the calculated results for the impact of 2-mm water and mercury drops on copper and aluminum targets at high velocities. Engel (1960) carried out experiments to measure pit depths in such impacts. Mercury drops were used because they are capable of imparting large momenta due to their high densities. Experimental results of Engel are also plotted on the figures for comparison. Calculated results seem to be surprisingly good in view of the crude nature of the model used. Because of the assumption that the target material behaves as a fluid, the model should be more applicable at higher values of the momentum. This is apparent from the figures; the correspondence between calculated and measured pit depths is better

for the mercury impact than for the water impact. Also, in the case of water impact, the calculated results get closer to the measured data as the impingement velocity increases.

Approximate Solution--Examination of the relative importance of the various parameters in the nondimensional form of the governing equation (equation (3.5)) revealed the possibility of a simple approximate solution. In the case of liquid-solid impacts σ is very large and consequently the nondimensional parameter A is very small. The first term on the right-hand side is therefore negligible in comparison with other terms. As suggested earlier, the shear term makes an insignificant contribution. In addition, the cavities are expected to be shallow, therefore $(h^{*\prime})^2 \ll 1$. With these approximations, equation (3.5) simplifies to

$$h^{*\prime\prime} + h^{*\prime}/r^* = -B_p^* \tag{3.12}$$

An exact solution to equation (3.12) can be obtained if the approximate form of the pressure distribution given by equation (3.9) is used. The solution of equation (3.12) subject to the proper boundary conditions (equation (3.3)) is then, simply,

$$h^* = (B/4) \exp(-r^{*2}) \tag{3.13}$$

The maximum cavity depth which occurs at $r^* = 0$ is given, in dimensional form, by the following expression:

$$h_{max} = \rho_1 V^2 \beta^2 R^2 / 8\sigma \tag{3.14}$$

The approximate solution given by equation (3.14) is compared with the numerical solution of the entire equation and with the experimental results of Engel in Figures 3.14 and 3.15 for impacts of mercury drops against 2024-0 aluminum and steel respectively. It can be concluded that the approximate solution is quite adequate. Similar correspondence was found in other cases not presented here.

It may be concluded from the above results that the jet model described above is capable of providing good results, at least in the case of liquid impact on metals. Unfortunately, experimental results in a form suitable for checking the validity of the model were not available for other materials, such as ceramics. However, the present results are significant in two respects. First, the results may be directly applicable because some designs of radomes suggest that metals may be incorporated in the attachment to the afterbody of the vehicle or in the nose as a protection against rain erosion. Microwave engineers have shown that such a use of metals is possible without serious detriment to radar performance. Second, the development of a reliable theory must be based upon materials on which the test data is repeatedly reproducible. Metals are such materials.

Apparent Mass Model

The apparent mass model, just like the jet model, is a rough, approximate hydrodynamic model. This model, based on a concept first used by Ludloff (1967) in connection with his study of hypervelocity impact, is characterized by the following assumptions:

1. Upon impact a fraction of the initial kinetic energy is expended in liquefying the surrounding target material. The remainder of the initial kinetic energy causes impulsive motion in the liquefied mass such as that which occurs when a body impacts on the free surface of a liquid. Such a motion can truly be characterized as irrotational (see Batchelor (1967)). The theory of flows with free surfaces suggests that the concept of "apparent" mass may be useful in describing the flow of the target material.

2. Since the drop is expected to be flattened by impact, the
    velocity field of the target material is similar to that
    around a disc translating through a fluid.

3. The material resists the formation of the crater by a force
    equal to the product of some strength property S of the mater-
    ial and the surface area of the crater.

When a body of mass M enters a liquid, there is a sudden reduction
of its velocity. This is ascribed to an apparent addition to its mass
by the mass of the liquid set instantaneously in motion. This additional
mass is called the apparent mass.

In the present case it will be assumed, for simplicity, that the
crater is hemispherical and remains in that shape as it grows with
increasing radius r. The equation of motion for the target fluid can
then be written as

$$d/dt[(M + M')r] + 2\pi r^2 S = 0 \qquad (3.15)$$

Here M is the mass of the drop and M' is the apparent mass. For the
motion of a disc, the apparent mass is given by (see Batchelor (1967))

$$M' = (8/3)\rho_2 c^3 \qquad (3.16)$$

where ρ_2 is the density of the target material and c is the radius of the
disc.

If M and M' are constant, equation (3.15) can be integrated over r
to obtain the energy equation

$$(1/2)(M + M')\dot{r}^2 + (2/3)\pi S r^3 = (1/2)MV^2 \qquad (3.17)$$

Here the condition $\dot{r} = V$ when $r = 0$ has been applied. V is the impact
velocity. The maximum cavity depth is the value of r when $\dot{r} = 0$ and is
given by

$$h_{max} = (3MV^2/4\pi S)^{1/3} \qquad (3.18)$$

Most of the rain erosion data, however, is expressed in terms of an erosion rate. An average erosion rate E will be defined here as follows:

$$E = h_{max}/t_{max} \tag{3.19}$$

Here t_{max} is the time required to achieve a cavity depth of magnitude h_{max}. The time t_{max} can easily be obtained by integrating equation (3.17).

The solution outlined above was tested against known experimental data. Although the model seems to be qualitatively correct, quantitative correspondence was lacking. This is hardly surprising in view of the very rough nature of the model.

It seems that the model may be improved by two additional considerations. First, no provision has been made in the model for ejected material during crater formation. This can be done, as suggested by Ludloff (1967), by specifying an additional integral condition based upon experimental results about ejecta. Second, the expression for the apparent mass (equation (3.16)) should be modified to take into account the growth of the crater. The following expression is suggested:

$$M' = \varepsilon\rho_2 r^3 \tag{3.20}$$

where ε is an adjustable parameter.

Equation (3.15) can then be written as

$$(d/dt)[(M + \varepsilon\rho_2 r^3)\dot{r}] + 2\pi r^2 S = 0 \tag{3.21}$$

This equation has to be solved numerically. Efforts are currently underway to determine the solution and to test it against experimental results.

The apparent mass model deserves further consideration, because, as opposed to the jet model, it considers the process to be time-dependent.

It is thus capable of calculating not only the maximum cavity depth but also the rate of erosion. The latter parameter, as indicated earlier, is the one that is usually measured in experiments relating to rain erosion.

SECTION IV.

STRESS WAVES RESULTING FROM LIQUID IMPACT

High-speed collisions with objects such as meteoroids and other debris in space or dust, hail, and raindrops in the atmosphere pose potential hazards to spacecraft, missiles, or airplanes.

A high-velocity impact generally creates a crater in the structure, driving a strong shock wave into it. If the impacted structure, or "target," is sufficiently thin, a puncture will result. If the target is relatively thick, the shock will rapidly decay into an elastic stress wave. When such a wave encounters a free surface it is reflected, generally as a tensile wave, and its amplitude may be of sufficient magnitude to produce fractures near the rear surface. Such fractures may appear as granular cracks near the surface, as rear surface bulges, or as a complete detachment of target material, creating a shrapnel effect. An example of each is shown in Figure 4.1 for copper, aluminum, and steel targets.

The fractures in a transparent acrylic (methyl methacrylate) resin are also shown in Figure 4.1. Although this material (trade names of Lucite and Plexiglas) would probably never be used for the actual structure, it is excellent for the study of stress waves and fracture as both the waves and the fracturing process can be photographed. These can then be compared with analytical conclusions (Kinslow (1964)).

Stress Relations for Spherical Waves

Spherical dilatational wave propagation in a homogeneous, isotropic material can be specified by the equation

$$\partial^2\phi/\partial t^2 = c_1^2[\partial^2\phi/\partial r^2 + (2/r)\partial\phi/\partial r] \qquad (4.1)$$

where ϕ is a scalar displacement potential, C_1 is the wave velocity, and t is time. Particle displacement (u) and velocity (v) are specified by the relations

$$u = \partial\phi/\partial r \quad \text{and} \quad v = \partial u/\partial t \tag{4.2}$$

where r denotes the radius vector from the point of projectile impact. The radial and tangential stresses are given by the relations

$$\sigma_r = (\lambda + 2\mu)(\partial u/\partial r) + 2\lambda(u/r) \tag{4.3}$$

and

$$\sigma_{t_1} = \sigma_{t_2} = \lambda(\partial u/\partial r) + 2(\lambda + \mu)(u/r) \tag{4.4}$$

where λ and μ are the Lamé constants and are related to Young's modulus (E) and Poisson's ratio (v) as follows:

$$\lambda = vE/(1 + v)(1 - 2v) \tag{4.5}$$

$$\mu = E/2(1 + v) \tag{4.6}$$

Model for Generating Stress Waves

The mathematical model for generating spherical elastic waves is that described by the author in the reference, Kinslow (1963). To summarize briefly, it is assumed that there is a hollow, hemispherical cavity in the target with its center at the point of impact and that a time-varying pressure or forcing function is applied to this imaginary cavity surface, generating stress waves in the material. The pressure applied to the surface of the cavity, having a radius r_o, is an impulse described by the relation

$$p/p_o = K(e^{-\alpha_1 t} - e^{-\alpha_2 t}) \tag{4.7}$$

where p_o is the maximum pressure, α_1 and α_2 are decay constants, t is elapsed time, and K is a constant. By the proper choice of values of α_1 and α_2 various wave forms can be generated. The values for describing the forcing function may be selected to approximate liquid impact.

Solution of the Wave Equation

If the forcing function is applied to the surface of the hemispherical cavity, a solution of the wave equation is

$$\phi = \sum_{i=1}^{n} (K_i p_o r_o)/(\rho r(\omega_0^2 + (a_0 - ia)^2)(-e^{-ia\tau}$$

$$+ e^{-a_0\tau} (1 + ((a_0-ia)/(\omega_0))^2)^{\frac{1}{2}} \cos(\omega_0\tau - \tan^{-1}(a_0-ia)/(\omega_0))))$$ (4.8)

where

$$r = t - ((r-r_0)/(C_1))$$ (4.9)

$$a_0 = (C_1/r_0)((1-2\nu)/(1-\nu))$$ (4.10)

$$\omega_0 = (C_1/r_0)(((1-2\nu)^{\frac{1}{2}})/(1-\nu))$$ (4.11)

Reflected Stress Waves

The simplest example of the reflection of an elastic dilatation wave from a free surface occurs when the wave strikes normal to the surface. Since the resulting surface stress must be zero, a compression wave must, therefore, always be reflected as a tensile wave, and a tensile wave must be reflected as a compression wave. When such a wave strikes a free surface at an oblique angle, the situation is much more complex. Not only will waves of dilatation be reflected but there will also be generated distortional or shear waves. From an analysis of these waves reflected from a plane surface (Kinslow (1969)), it seems that only the incident and reflected dilatation waves need to be considered in determining the maximum tensile stress except at points some distance from the normal axis where fractures are not likely to occur. For this reason, the amplitude of the reflected shear waves are not computed in this preliminary analysis, although their existence is recognized and taken into account in the computation of the magnitude of the reflected dilatation waves.

Relative values of computed principal stresses soon after the wave reflection from a plane surface are shown in Figure 4.2. Compressive stresses are considered as positive and tensile stresses as negative. At the time shown, the maximum tensile stress has a value of -61 units. It can be seen, however, that this is not the maximum tension that will be created as at a slightly later time this reflected tensile wave will combine with the tensile "tail" of the incident wave to generate a much higher tensile stress at a somewhat greater distance from the rear surface.

Stresses Resulting from Multiple Impacts

The coordinate system is given in Figure 4.3. The locations of impacts on a plane surface (the x-y plane) are designated as $O_n(O_1,O_2,O_3,---)$ and are given by the coordinates (x_{on},y_{on}). The location of any point P at which the principal stresses are desired is specified by the coordinates (x,y,z). For the computation of stresses resulting from impact at O_n, the coordinates (x_n,y_n,z_n) are employed, where

$$x_n = x - x_{on} \tag{4.12}$$

$$y_n = y - y_{on} \tag{4.13}$$

$$z_n = z \tag{4.14}$$

The location of P may also be specified by the coordinates (r_n,θ_n,ϕ_n).

The following derivation of the components of stress at point P are relative to the O_n coordinate system. For the sake of simplicity the subscript n is omitted from the derivations and in the six cartesian components of stress, the symbol $[\ ]_n$ indicates that all values enclosed by the bracket are relative to that system.

The relations between the (x,y,z) and the (r,θ,ϕ) coordinates are

$$x = r \sin\phi \cos\theta \qquad (4.15)$$

$$y = r \sin\phi \sin\theta \qquad (4.16)$$

$$z = r \cos\phi \qquad (4.17)$$

The direction cosines of the positive r-axis have components in the (x,y,z) system as follows

$$\cos(x,r) = \partial x/\partial r = \sin\phi \cos\theta \qquad (4.18)$$

$$\cos(y,r) = \partial y/\partial r = \sin\phi \sin\theta \qquad (4.19)$$

$$\cos(z,r) = \partial z/\partial r = \cos\phi \qquad (4.20)$$

Similarly, the direction cosines of the $t_\theta - \xi t_\phi$-axis are respectively

$$\cos(x,t_\theta) = (1/r \sin\theta)(\partial x/\partial\theta) = -\sin\theta \qquad (4.21)$$

$$\cos(y,t_\theta) = (1/r \sin\theta)(\partial y/\partial\theta) = \cos\theta \qquad (4.22)$$

$$\cos(z,t_\theta) = 0 \qquad (4.23)$$

and

$$\cos(x,t_\phi) = (1/r)(\partial x/\partial\phi) = \cos\phi \cos\theta \qquad (4.24)$$

$$\cos(y,t_\phi) = (1/r)(\partial y/\partial\phi) = \cos\phi \sin\theta \qquad (4.25)$$

$$\cos(z,t_\phi) = (1/r)(\partial z/\partial\phi) = -\sin\phi \qquad (4.26)$$

where

$$r = \sqrt{x^2 + y^2 + z^2} \qquad (4.27)$$

$$\sin\phi = \sqrt{x^2 + y^2}/r \qquad (4.28)$$

$$\cos\phi = z/r \qquad (4.29)$$

$$\sin\theta = y/\sqrt{x^2 + y^2} \qquad (4.30)$$

$$\cos\theta = x/\sqrt{x^2 + y^2} \qquad (4.31)$$

As the spherical wave propagates through the material, the radial and tangential stresses having values given by equations (4.3) and (4.4), respectively, are shown acting on an elemental volume in Figure 4.4. At

any point, P, and for any time. The six cartesian components of stress relative to the $[o,x,y,z]_n$ coordinate system may be computed from the following relations.

$$[\sigma_x]_n = [\sigma_{t\theta}\cos^2(x,t_\theta) + \sigma_{t\phi}\cos^2(x,t_\phi) + \sigma_r\cos^2(x,r)]_n \qquad (4.32)$$

$$[\sigma_y]_n = [\sigma_{t\phi}\cos^2(y,t_\phi) + \sigma_r\cos^2(y,r) + \sigma_{t\theta}\cos^2(y,t_\theta)]_n \qquad (4.33)$$

$$[\sigma_z]_n = [\sigma_r\cos^2(z,r) + \sigma_{t\theta}\cos^2(z,t_\theta) + \sigma_{t\phi}\cos^2(z,t_\phi)]_n \qquad (4.34)$$

$$[\tau_{xy}]_n = [\sigma_{t\theta}\cos(x,t_\theta)\cos(y,t_\theta) + \sigma_{t\phi}\cos(x,t_\phi)\cos(y,t_\phi)$$
$$+ \sigma_r\cos(x,r)\cos(y,r)]_n \qquad (4.35)$$

$$[\tau_{yz}]_n = [\sigma_{t\phi}\cos(y,t_\phi)\cos(z,t_\phi) + \sigma_r\cos(y,r)\cos(z,r)$$
$$+ \sigma_{t\theta}\cos(y,t_\theta)\cos(z,t_\theta)]_n \qquad (4.36)$$

$$[\tau_{zx}]_n = [\sigma_r\cos(z,r)\cos(x,r) + \sigma_{t\phi}\cos(z,t_\phi)\cos(x,t_\phi)$$
$$+ \sigma_{t\theta}\cos(z,t_\theta)\cos(x,t_\theta)]_n \qquad (4.37)$$

These components of stress resulting from each of the several impacts can now be added as follows:

$$\sigma_x = [\sigma_x]_1 + [\sigma_x]_2 + [\sigma_x]_3 + \ldots \qquad (4.38)$$

$$\sigma_y = [\sigma_y]_1 + [\sigma_y]_2 + [\sigma_y]_3 + \ldots \qquad (4.39)$$

$$\sigma_z = [\sigma_z]_1 + [\sigma_z]_2 + [\sigma_z]_3 + \ldots \qquad (4.40)$$

$$\tau_{xy} = [\tau_{xy}]_1 + [\tau_{xy}]_2 + [\tau_{xy}]_3 + \ldots \qquad (4.41)$$

$$\tau_{xz} = [\tau_{xz}]_1 + [\tau_{xz}]_2 + [\tau_{xz}]_3 + \ldots \qquad (4.42)$$

$$\tau_{yz} = [\tau_{yz}]_1 + [\tau_{yz}]_2 + [\tau_{yz}]_3 + \ldots \qquad (4.43)$$

These six components of stress are now substituted in the following cubic equation:

$$S^3 - (\sigma_x + \sigma_y + \sigma_z)S^2 + (\sigma_x\sigma_y + \sigma_y\sigma_z + \sigma_z\sigma_x - \tau_{xy}^2 - \tau_{yz}^2 - \tau_{zx}^2)S -$$
$$(\sigma_x\sigma_y\sigma_z - \sigma_x\tau_{yz}^2 - \sigma_y\tau_{zx}^2 - \sigma_z\tau_{xy}^2 + 2\tau_{xy}\tau_{yz}\tau_{zx}) = 0 \qquad (4.44)$$

The roots of this equation are the three principal stresses.

Stresses Resulting from Two Liquid Impacts

One of the problems that must be dealt with in the analysis of radome damage resulting from rain impact is the effects of multiple drops and the interaction of the stresses developed by the individual drops.

When a rain field is described, the probable spatial and time distribution of drops interacting with a radome surface moving at a specified velocity can be determined. The effects of the distances between two drops and the times between impacts are analyzed.

The stresses computed are relative values only and dimensionless units of time and dimensions are employed. The radome thickness is denoted by T, the stress by σ, and the time by τ. A pressure wave typical of high-velocity impact is employed.

First, two impacts at the same time are considered. The maximum tensile stress resulting from two impacts will be generated either directly beneath the points of impact or on an axis midway between these points. Figure 4.5 gives the values of the tensile stress for different distances between the impact points. The maximum tensile stress for a single impact has a relative value of $\overline{\sigma} = 115$. If two drops are very close together at the same time, the resulting stress will obviously be twice this value, or 230. As the distance between drops is increased, the developed stress will decrease. In this case of simultaneous impacts, it can be seen that the maximum stress occurs along the axis between the two points. At a distance of about 0.8 T, the stresses directly beneath the impact points have decreased to about that resulting from a single drop, but the stress on the z-axis has a value of almost 200. The stress on this axis continues to decrease as

the distance between drops increases. At a distance of approximately 1.8 T, the stress on this axis has decreased to the value created by a single impact. This means that if the distance between two drops is greater than twice the thickness of the target, the maximum stress can probably be determined by computing the stress developed by a single drop and that the interaction of the stress waves can be neglected.

The effect of time $(\overline{\Delta t})$ between drops will now be considered. The stresses developed by two drops impacting the same point are shown in Figure 4.6(a). As pointed out, the tensile stress will have a value of ⁻30 for zero time between impacts. As the time increases, the stress decreases up to a relative time of 0.50, beyond which the stress is the same as for the impact of a single drop. If the distance between drops is 0.4 T, the tensile stress for various times $(\overline{\Delta t})$ is given in Figure 4.6(b). The first impact is P_1 and the later impact is P_2. The other curves give this information for various distances between impacts.

It should be noted that these results are based on an assumed material and for a typical stress wave. The results would not be the same for different materials and impact conditions.

Stresses Resulting from Single-Drop Impact

When a collision occurs between a fast-moving surface and a water-drop, a high pressure is first generated at the point of contact. This is followed by a lateral flow of water at very high velocity. The pressure distribution at the liquid-solid interface and the times and durations of the pressures at various points on the surface have not yet been determined except for rather low impact velocities such as that being done by Huang (1971-72). Similar data for high Mach numbers is

perhaps the greatest need in the analysis of this problem at the present time. Both analytical and experimental methods are being employed in attempts to obtain this information. For the relatively low-velocity impacts, Huang's computations indicate that the pressure is a maximum at the center of the impact area, decreasing as the distance from the center increases. Some, including Herbert (1970), believe that the pressure is not a maximum at the center, but that the maximum pressure is near the periphery of the drop. Others believe that cavitation occurs because of the high jet velocity creating tensile stresses at the surface.

Due to the non-uniform time-varying pressure distribution generated by liquid-drop impact, it is not possible to accurately determine the stress wave characteristics by a single stress wave source. The method of multiple impacts derived in a previous paragraph will be used by considering a cluster of wave sources as shown in Figure 4.7 for each drop impact. The forcing function to be applied to each imaginary cavity will be determined by the pressure-time history over the target surface. This will result in a large number of wave fronts which, according to huygens' principle, will combine to form a single wave. The stress distribution created by this wave can be computed for various times. The maximum pressure, tension, and shear stresses, as well as the displacements, strains, and strain rates can be determined.

The locations of fractures in a Perspex plate resulting from the impact of a water jet is shown in Figure 4.8(a). This was taken from one of the many excellent photographs by Brunton (1967) of Cambridge University. It shows a ring crater on the surface, a fracture directly under the center of the impact area, and a large fracture near the rear surface. Not knowing the actual pressure distribution, various values were assumed

and the maximum tensile stresses were computed throughout the target. The areas where these stresses exceeded a specified value are shown in Figures 4.8(b) through (g). The similarity to the observed fractures may be seen. The stresses not only depend upon the maximum pressure distribution but the time rate of the spread of these pressures from the point of first contact. This is illustrated by Figures 4.8(e) and (f). The same maximum pressure distribution was assumed in both instances and only the times were different. These shaded areas would represent fractures only if a critical stress criterion of fracture applies.

By assuming various combinations of pressures and times, it may be possible to obtain a numerical solution that will match the experimental results. If this is accomplished, the pressure-time values used in the computation should represent the true values for that particular impact.

This method of multiple stress wave sources can also be applied for the case of oblique impact if the pressure-time variations are known.

SECTION V.

PRELIMINARY EXPERIMENTS

Liquid Jet Accelerator

A device similar to the one constructed at the Cavendish Laboratory, University of Cambridge, and described by Fyall in Chapter 8 of the Radome Engineering Handbook, edited by Walton (1970), has been constructed and used to accelerate small amounts of water to a relatively high velocity. The accelerator is shown in Figure 5.1. The nylon piston is inserted in the chamber to almost the end; a few drops of water are inserted in the orifice with a hypodermic needle; and the piston is accelerated by means of a 0.22-caliber rifle bullet striking its end. For the dimensions shown, a bullet velocity of 750 ft/sec accelerates the water to a velocity of 2200 ft/sec. Photographs of the impact range (constructed in a surplus iron lung) are shown in Figure 5.2. The jet coming from the nozzle is shown in Figure 5.3. Variations in the piston and nozzle design, the amount of water, and the bullet velocities will be made in attempts to reach higher velocities and to more accurately simulate raindrops.

Impact Damage to Lucite Targets

Figure 5.4 shows the ring fractures on the surface of a 0.25-inch Lucite target. The center portion of the surface was not affected. The lower photograph on the first page is of a sectioned target so that the depth of fracture could be seen. Ring craters resulting from lower velocities are shown on the second page of the figure. These ring craters are similar to the ones photographed by Brunton (1967) and by Fyall (1969). Side views of targets are shown in Figure 5.5 in which

the rear surface fractures can be seen. There were also fractures below the center of the point of impact but are barely distinguishable in these photographs.

A vertical milling machine and a dial gage were used as a profilometer for measuring crater depths. Figure 5.6 shows the craters on a nosecone being measured. The photograph, cross-section, and depth contours of a crater in Lucite are shown on Figure 5.7.

Damage to Slip-Cast Fused Silica Targets

The front and rear surfaces of the SCFS targets were painted with black ink before impact so that the extent of any fractures could be easily seen. The photographs at the top of Figure 5.8 show the damage to a 0.25-inch target. It was completely penetrated. The fracture as viewed from the back is interesting. The lower photographs of this figure show the damage to a slightly thicker target. The familiar ring crater is seen on the front and a crack is detected on the rear. Cross-sections of this crater are shown in Figure 5.9. The maximum depth is about 0.0085 inch. Unlike the ring crater in Lucite, the center, apparently undamaged portion, shows a permanent deformation. It may be, however, that the material is not compressed but that the crack whose boundaries are seen on the rear surface extends internally to the front crater and that this entire cone of material is pushed backward. Crater contours are shown in Figure 5.10.

It appeared that the fracture of the 0.40-inch target shown in Figure 5.11 was very similar to the last one discussed except for the rear surface spall directly behind the impact point and that the fracture approximately 1 inch from the center was somewhat more pronounced. Shortly after the first photographs were made, the entire rear portion

shown in the last two photographs of this figure became detached. Upon an examination of these fractures, Figure 5.12 was drawn. The photographs of Figure 5.13 show an edge view of the target just before and following impact. The spall material can be seen. Surface damage resulting from oblique impacts is shown in Figure 5.14.

A Possible Explanation of the Target Fracture

The fractures indicated by A, B, and C of Figure 5.12 are of interest as either of them would probably cause greater damage than does the ring crater. The crack C is of special importance for the reason that it creates the largest spall, and hence more structural weakening, than either of the others would have produced.

Initially the path of crack A is determined by the tensile stresses around the immediate impact area. As suggested by Yoffee (1951) the crack propagates into the plate normal to the maximum tangential stress near the crack tip. If this maximum stress is caused to shift from its original direction, the direction of the crack propagation would be expected to change. This could be caused by the stress waves generated by the impact and is probably the reason for A not following a straight line. The maximum speed of the crack propagation was analytically determined by Yoffee to be approximately 0.6 times the velocity of the shear wave. This agrees well with the value of 0.38 times the dilatational wave velocity as observed by Küppers (1967) in experiments with glass.

It is apparent that the stress wave associated with the impact travels through the plate and reflects from the rear surface, intersecting the crack before it has time to propagate through the target.

It is computed that the crack reaches the first point of branching in approximately 3.5 μ-sec and that the reflected dilatational wave reaches the same point in approximately 3.4 μ-sec. The stresses associated with the arrival of this wave will cause a change in the state of stress around the propagating crack tip and is probably the cause of the branching which creates crack C. As the reflected shear wave velocity is less than that of the dilatational wave, it will intersect crack A at a later time and would be expected to cuase another branching such as crack B.

SECTION VI.

SLED TEST RESULTS

A rocket sled test program was conducted at Holloman Air Force Base, New Mexico, to determine the rain erosion resistance of slip-cast fused silica at velocities above 5000 ft/sec. The fabrication techniques used at the Georgia Institute of Technology to slip-cast, heat-treat, and flame-glaze the radomes; a description of the test facilities; and the results of six sled tests have been described by Walton and Harris (1966).

The radome from run No. 2, Holloman No. 7RB1, serial No. 2723 has been examined, and some observations will be made concerning the impact damage that it sustained in the 400-ft rainfield. The rain intensity was reported as 2.5 inches per hour and the average drop size was said to be between 1.5-and 2.0-mm diameter. The average velocity was about 5300 ft/sec.

Figure 6.1 shows the radome on the sled after the run. A view of the radome with its metal tip broken off and a closer view of some of the craters are shown in Figure 6.2. Its dimensions as well as the locations of the centers of the photographs of Figures 6.4, 6.5, and 6.6 are given in Figure 6.3.

The photographs of Figure 6.4 were taken around the circumference at 45-degree intervals at a distance of 11.6 inches from the tip. By counting all craters that could be detected, it was found that they averaged 27.1 per square inch. Those of Figure 6.5 were 8.3 inches from the tip and averaged 40.4 craters per square inch. At a distance of 3.0 inches from the tip, the photographs overlapped and they are shown in Figure 6.6. These averaged 25.1 craters per square inch. At

this location there appeared to be more erosion from the impacts than craters. Based on all of these photographs, it was estimated that for the entire radome there was an overall average of 31 craters per square inch. There is probably some reason as to why the crater density is greater near the middle of the radome than near either the tip or the base, but we have no explanation at this time. The radome had been flame-glazed by the use of a plasma jet to fuse the surface and to provide a coating of non-porous fused silica that served to seal the surface. Walton and Harris reported the thickness of the fused layer varied from 0.03 to 0.04 inch near the tip to less than 0.005 inch near the base. They also reported that although each drop appeared to cause some surface damage it did not appear to extend significantly beneath the glazed surface. This is in agreement with our findings as we measured only a few depths greater than 0.005 inch.

Because the impact velocities of all drops, both large and small, are essentially the same, various authorities argue that the impact pressures as given by the "water-hammer" equation, $P = \rho CV$, will be the same for all drops where ρ is the density of the liquid, C the velocity of the compression wave in the liquid, and V the component of the impact velocity normal to the surface. Brunton (1967) explains that one of the reasons why a large drop is more damaging than a small one at the same velocity is that with the large drop the maximum pressure acts for a longer period of time. This would also result in longer stress waves being propagated into the target, affecting the internal cracking and spall damage. The areas of the craters resulting from the larger drops would obviously be greater than those caused by small drops.

There still remains the question as to whether or not the "water-hammer"
pressure is the maximum.

Crater Characteristics

The depths of some of the craters were measured and depth contours
were plotted. The purpose of this is to learn more of the nature of the
fractures and to determine the extent to which drop impacts can be simu-
lated by the use of the water jet accelerator and by solid projectile
impacts. Cross-sections of a typical crater near the base of the radome
are shown in Figure 6.7. The depths were measured from the curved sur-
face of the radome. The first profiles were taken outside the crater
and indicate the roughness or irregularities of the surface. As it is
impossible to recognize the actual crater boundaries from the measure-
ments (although they can be seen visually) because of the surface rough-
ness, the depths shown in Figure 6.8 start with the 0.001-inch contour.
Comparing the profiles and depth contours of this crater with those
produced by the jet-produced cavity shown in Figures 5.9 and 5.10 several
similarities and differences will be noted. In both cases there is a
central plateau surrounded by areas of greater depth containing several
rather deep pits. The primary differences are that the radome crater
is more irregular in shape (although its actual boundary is not shown)
and the crater surface is rougher. The jet-produced crater is somewhat
larger and deeper than that formed by the drop. Also, the central
plateau of the first was the original surface which had been painted
black and it is apparent that at least some of the original radome
surface had been removed from this region in the second. The differences
are simple to explain; in fact, the similarities are more than would have
been expected.

Although both targets were of slip-cast fused silica, the surfaces were entirely different. As stated, the radome had been provided with a coating of non-porous fused silica which varied from 0.005 to 0.030 inch thick. Walton (1966) observed that once the impact pressure was sufficient to cause damage in the glazed surface that there was a tendency to chip out a portion of the glaze extending beyond the actual area of impact. In an unglazed surface, he reported, the damage was restricted to the area of impact. For a comparison of the damage resulting from jet impacts and drop impacts, it is necessary to have two identical materials. From these results, however, it appears that the drop impact can be simulated.

Another explanation of the difference between the two craters is that the jet impact was normal to the target's surface at a velocity of about 2000 ft/sec and that of the drop was at an angle of about 15° at a speed of approximately 5000 ft/sec, giving a normal velocity component of approximately 1300 ft/sec. This difference may explain the difference between maximum crater depth of 0.008 inch in the jet-created crater and only 0.005 inch in the drop-generated.

The direction of impact seems to make little difference in the crater's general appearance. It appears that the simulation of a high-velocity impact at a small angle with the surface can be accomplished with a lower velocity impact at a different angle as long as the normal velocity components are the same. For example, the velocity of 5000 ft/sec at 15° with the surface could probably be simulated with a velocity of 2000 ft/sec at an angle of 40°.

The profiles and crater contours of another crater located near the midpoint of the radome surface are given in Figures 6.9 and 6.10.

Although this crater area is less than the previous one, its depth is somewhat greater.

The Rain Field

It has been suggested that some of the drops may be deflected away from the radome's surface by the hypersonic shock layer. The simulated rain rate for the Holloman tests was adjusted to 2.5 inches per hour. The drop size distribution for this facility as given by Mortensen (1970) agrees reasonably well with the one for natural rain given by Fyall (1970). Based upon this distribution and a terminal drop velocity of 6 m/sec, also from Fyall (1970), which gives a concentration of 2.94 gm/m^3, the following distribution of drop sizes was computed:

Drop Diameter (mm)	Number in 1 m^3
0.25 - 0.75	672
0.75 - 1.25	305
1.25 - 1.75	241
1.75 - 2.25	145
2.25 - 2.75	74
2.75 - 3.25	32
3.25 - 3.75	15
3.75 - 4.25	5
4.25 - 4.75	2
4.75 - 5.25	1
	1492 drops/m^3

The base area of the radome times the length of the rainfield gives a volume of 3.54 m^3 or 5147 drops in its path. Considering the radome as conical, its surface area is 155 in.^{2}. This gives an average of 33 impacts per square inch if all drops in the radome path were intercepted. As the number of craters was estimated to be 31 per square inch, it is concluded that practically all drops in the radome's path produced craters. This was also the conclusion reached by Walton (1967), who stated that an

examination of the radome revealed that the number of drops impacted corresponded to the number of drops larger than 0.5 mm. It is also in agreement with the analytical conclusions reached in Section II of this report which indicated that for all velocities of this radome between 2000 and 10,000 ft/sec, the maximum deflection of the raindrops would be less than one-half degree.

SECTION VII.

PLANNED FUTURE INVESTIGATIONS

The research described in this report will be extended in several ways. These are described below.

The Motion of Raindrops in a Hypersonic Shock Layer

First, calculations will be carried out for blunt-nosed (spherical) vehicle shapes. Since the shock wave is detached from the body surface in such cases, one would expect that the effectiveness of the inter-phase drag force in slowing down the drops before they strike the vehicle surface would be greater for a spherical shock layer than for a conical shock layer. This, in turn, would lead to less likelihood of damage to the radome. The computations described above will deter-mine what, if any, lessening of susceptibility to rain erosion damage would be produced by nose blunting so that this could be weighed against other factors in missile design.

Second, the interphase drag and heat transfer laws will be modified to apply to the case of moderate void fractions (the void fraction is the ratio of the air volume to the total mixture volume). All previous work has been restricted to the case of large void fractions. The sen-sitivity of the solution variables to the value of the void fraction will be found and, if necessary, the appropriate correction factors to the large-void-fraction solutions will be determined.

Third, extensive calculations will be carried out to determine the sensitivity of the results to the distribution of drop sizes present within the mixture. Previous work has assumed that the exact size dis-tribution is unimportant and that the real rain field can be replaced, for the purposes of analysis, with a fictitious rain field in which all

drops have the same size. This effective size is usually taken to be
the average size of the actual drops. The limits of validity of this
assumption will be found and, if necessary, correction factors will be
determined.

Fourth, an attempt will be made to obtain approximate closed-form
solutions for conical and spherical shock layers. Such formulas would
allow rapid estimation of the solution variables for design purposes.
The trends of the numerical data obtained thus far suggest several
possible approximations that would simplify the basic differential
equations enough to make possible analytical solutions. The limits
of validity of the approximate solutions will be determined by compari-
son with the exact numerical results.

Cratering and Erosion Mechanism

Research performed under the present contract has shown that the
jet-impingement model is a very useful tool in the investigation of
high-velocity impacts of drops against solid targets. This model will
be improved as described below.

An important ingredient of the model mentioned above is the distri-
bution of the pressure applied to the target by the impinging drop.
Past work has employed pressure distributions obtained by fitting curves
to experimental data found from observations of jets impinging on rigid
surfaces. A better pressure distribution will be found by extending
the work of Huang (1971) who investigated the two-dimensional low-speed
impact of drops of various shapes on a rigid plane by numerical solution
of the hydrodynamic partial differential equations governing the motion
of fluid in the drop. Huang's method will be applied to both normal and

oblique high-speed impacts on elastic surfaces. The thermal energy
equation will be solved together with the hydrodynamic equations.
This will allow the calculation of heat transferred to the target.
This is expected to be important for high-speed impacts. The boundary
conditions at the target surface will be modified by a procedure simi-
lar to that used by Lee and Cheng (1971) to account for the elasticity
of the target. The pressure distributions thus obtained will then be
used in the jet-impingement model to obtain further information about
crater depths and sizes and the influence of various factors on these
quantities.

Fractures Resulting from Stress Waves Generated by Liquid Impact

Equations have been derived and computer programs have been written
that will enable values of stress in an impacted target to be computed
if the pressure-time relationships on the surface are known. The pres-
sures created by both the drop impact and the lateral jetting action
are considered in the computation of the stresses resulting from the
generated stress waves. The reflections of these waves from the inside
surface of the radome are also taken into account. This program will
also compute the stresses resulting from any number of multiple impacts
at any time intervals and on both normal and inclined surfaces.

When a rain field is described (i.e., inches per hour, duration,
and drop size distribution) and the radome profile, thickness, and
velocity are specified, it will be possible to completely determine
the probable damage. Before this can be done, however, the items men-
tioned in the previous paragraphs such as the size and motion of drops
behind the shock wave, the effects of aerodynamic heating, the distri-
bution and duration of pressure applied to the target, and the fracture

criteria for the radome material must be determined. These are some of the important topics that will be investigated during the coming year.

Experimental and Quasi-Theoretical Investigations

It appears that perhaps the greatest insight into the mechanics of rain erosion may be gained from experimental and semi-empirical investigations. Experimental results are certainly necessary to establish the validity or limitations of theoretical analyses. Although only preliminary experimental work has been done to date, the results are in qualitative agreement with the theory of fracture that has been proposed. This theory does not agree with those proposed by other investigators, but it is the only one that explains all types of fractures that have been observed to result from liquid impact. Further work will be performed to give quantitative results. Although emphasis is to be placed upon damage to ceramic type radome materials, Lucite is being used as the standard material in some of these studies because its properties are well known, because of its transparency and easy determination of internal damage, and because its surfaces can be artificially roughened to determine the effect of surface conditions on the lateral jetting and resulting surface pressures. Once the distribution and duration of the pressures on the target are determined for various parameters, these can be applied to other materials to determine the damages that would be caused.

A liquid jet accelerator has been constructed to simulate raindrop impact. The first shots gave velocities of approximately 2000 ft/sec. It is believed that by making modifications in design, the velocities can be at least doubled. It will also be possible to accelerate two drops

simultaneously so that the effects of multiple impact can be determined and compared with the theoretical results. By the use of other liquids such as mercury it will be possible to simulate higher impact velocities.

A few liquid impacts of slip-cast fused silica targets have been made. The craters seem to be very similar to those formed during rocket sled tests.

A profilometer has been constructed with which measurements of the craters can be made. A series of experiments will be performed from which data the drop velocities and sizes can be correlated with crater characteristics such as volume and depth for various angles of impact. These experiments will also include the effects of varying the temperature of the targets. The effects of surface roughness will also be investigated.

It seems that the effects of the reflected stress waves from the inner surface is very important. Spallation may present a serious problem if thin-walled radomes are used. Detachment of radome material from the inner surface at high velocities would destroy equipment. Water impact experiments show that the rear surface of the target often suffers a greater damage than the front surface. Experiments have also demonstrated the importance of having a smooth and uniform rear surface as small defects such as scratches and voids greatly weaken the target.

Another phase of the proposed experimental program is to impact the targets with small solid particles. There are at least three reasons for this: (1) In flight, aircraft and missiles encounter foreign bodies other than water drops; (2) To aid in a more complete understanding of the mechanics of the collision process; (3) To examine the merits and limitations of simulation techniques in which solid particles are

substituted for water drops. The last of these is perhaps the principal reason for including these experiments in this program. A light-gas gun with the capability of accelerating drop-size plastic projectiles to velocities as high as 40,000 ft/sec has been constructed at Tennessee Tech. Lead and polyethylene spheres have been used to simulate rain erosion. Plasticine (modeling clay) is said to most closely resemble water flow characteristics on impact.

A ballistic pendulum will be used to determine the energy and momentum transfer to the target. The momentum multiplication factor is a very important value to be determined for both normal and oblique impacts. Other types of instrumentation will include the use of strain and thermal gages, interferometry, photoelasticity, etc. as needed to identify the important parameters that are critical to the radome's performance in a rain environment.

REFERENCES

Banks, R. B. and Bhavamai, A. (1965), "Experimental Study of the Impingement of a Liquid Jet on the Surface of a Heavier Liquid," Journal of Fluid Mechanics 23, p. 229.

Banks, R. B. and Chandrasekhara, D. V. (1963), "Experimental Investigation of the Penetration of a High-Velocity Gas Jet through a Liquid Surface," Journal of Fluid Mechanics 15, p. 13.

Batchelor, G. K. (1967), An Introduction to Fluid Dynamics, Cambridge University Press.

Brunton, J. H. (1967), "Erosion by Liquid Shock," Proceedings of the Second Meersburg Conference on Rain Erosion and Allied Phenomena, A. A. Fyall and R. B. King, editors.

Cheslak, F. R., Nicholls, J. A., and Sichel, M. (1969), "Cavities Formed on Liquid Surface by Impinging Gas Jets," Journal of Fluid Mechanics 36, p. 55.

Eisenberg, P. (1970), "Cavitation and Impact Erosion-Concepts, Correlations, Controversies," Characterization and Determination of Erosion Resistance, ASTM STP 474, p. 3.

Engle, O. (1957), "Mechanism of Rain Erosion, Part X: A Review and Evaluation of the Present State of the Problem," National Bureau of Standards, Washington, D. C., WADC TR-53-192X, AD-142240.

Engle, O. G. (1959), "Pits in Metal Caused by Collision with Liquid Drops and Soft Metal Spheres," Journal of Research of National Bureau of Standards 62, p. 229.

Engle, O. G. (1960), "Pits in Metal Caused by Collision with Liquid Drops and Rigid Steel Spheres," Journal of Research of National Bureau of Standards 64A, p. 61.

Engle, O. G. (1966), "Crater Depths in Fluid Impacts," Journal of Applied Physics 37, p. 1798.

Engle, O. G. (1967), "Initial Pressure, Initial Flow Velocity, and the Time Dependence of Crater Depth in Fluid Impacts," Journal of Applied Physics 38, p. 3935.

Fyall, A. A. and Smith, P. (1969), "Single Impact Studies of Rain Erosion--Part 1. Preliminary Evaluation," Royal Aircraft Establishment Technical Report 69086.

Fyall, A. A. (1970), "Rain Erosion--A Special Radome Problem," Chapter 8, Radome Engineering Handbook, J. D. Walton, editor, Marcel Dekker, Inc., New York.

Gibson, A. H. (1934), Hydraulics and Its Application, Constable.

Hammit, F. G., et al (1967), "Laboratory Scale Devices for Rain Erosion Simulation," Proceedings of the 2nd Conference on Rain Erosion and Associated Phenomena, Meersburg, Germany, 166.

Herbert, W. (1970), "Comparison Between Some Characteristic Parameters of Rain and Sand Erosion," Proceedings of the 3rd International Conference on Rain Erosion and Associated Phenomena, A. A. Fyall and R. B. King, editors.

Heymann, F. J. (1967), "Eine Übersicht von Schlusseln zu den Verhaltnissen zwischen der Erosiongeschwindigkeit und Augschlags-Parametern." Proceedings of the 2nd Conference on Rain Erosion and Associated Phenomena, Meersburg, Germany, 98.

Heymann, F. J. (1969), "High Speed Impact between a Liquid Drop and a Solid Surface," Journal of Applied Physics 40, p. 5113.

Hsu, P. W. (1972), "Jet Model of High Speed Liquid Solid Impacts," M. S. Thesis, Tennessee Technological University.

Huang, Y. C. (1971), "Numerical Studies of Unsteady, Two-Dimensional Liquid Impact Phenomena," Ph.D. Thesis, Mech. Engr. Dept., Univ. of Mich.; also available as ORA UMICH Report 03371-8-T.

Huang, Y. C. and Hammitt, F. G. (1972), "Liquid Impact on Elastic Solid Surface," Univ. of Mich., College of Engrg., Mech. Engr. Dept., Report No. UMICH 03371-12-I.

Kinslow, Ray (1963), "Properties of Spherical Stress Waves Produced by Hypervelocity Impact," AEDC-TDR-63-197 (AD421578).

Kinslow, Ray (1964), "Observations of Hypervelocity Impact of Transparent Plastic Targets," AEDC-TDR-64-49 (AD438947).

Kinslow, Ray (1969), "Properties of Reflected Stress Waves," AIAA Hypervelocity Impact Conference, Cincinnati, Ohio, AIAA Paper No. 69-363.

Küppers, Horst (1967), "The Initial Course of Crack Velocity in Glass Plates," International Journal of Fracture Mechanics 3, No. 1, p. 13.

Leach, S. J., and Walker, G. L. (1966), "The Application of High Speed Liquid Jet to Cutting," Phil. Trans., Roy. Soc. (London) 260A, p. 295.

Lu, H. Y. and Chiu, H. H. (1966), "Dynamics of Gases Containing Evaporable Liquid Droplets Under a Normal Shock," AIAA Journal 4, p. 1008.

Ludloff, K. G. (1967), "A Hydrodynamic Model for Hypervelocity Impact," Ph.D. Dissertation, U.C.L.A.

Marble, F. E. (1970), "Dynamics of Dusty Gases," *Annual Review of Fluid Mechanics* 2, p. 397.

Mortensen, R. B. (1970), "Rain Erosion Testing from 1 to 6 Km/Sec," Proceedings of the 3rd International Conference on Rain Erosion and Associated Phenomena, A. A. Fyall and R. B. King, editors.

Opik, E. J. (1936), "Researches on the Physical Theory of Meteor Phenomena: I. Theory of the Formation of Meteor Craters," *Tartu Ulikool Sternwarte Publications*, Publications de l'Observatories Astronomique de l'Universite de Tartu, 28, 1.

Panton, R. (1968), "Flow Properties for the Continuum Viewpoint of a Non-Equilibrium Gas-Particle Mixture," *Journal of Fluid Mechanics* 31, p. 273.

Panton, R. and Oppenheim, A. K. (1968), "Shock Relaxation in a Particle-Gas Mixture with Mass Transfer Between Phases," *AIAA Journal* 6, p. 2071.

Peddieson, J. and Lyu, C. H. (1973), "Dusty Hypersonic Wedge Flows," *AIAA Journal* 11, to appear.

Plesset, M. S. and Chapman, R. B. (1971), "Collapse of an Initially Spherical Vapor Cavity in the Neighborhood of a Solid Boundary," *Journal of Fluid Mechanics* 47, p. 283.

Probstein, R. F. and Fassio, F. (1970), "Dusty Hypersonic Flows," *AIAA Journal* 8, p. 772.

Rosler, R. S. and Stewart, G. H. (1968), "Impingement of Gas Jets on Liquid Surfaces," *Journal of Fluid Mechanics* 31, p. 163.

Soo, S. L. (1967), *Fluid Dynamics of Multiphase Systems*, Blaisdell Publishing Co.

Spurk, J. H. and Gerber, N. (1972), "Dust Collection Efficiency for Power Law Bodies in Hypersonic Flight," *AIAA Journal* 10, p. 755.

Waldman, G. D. and Reinecke, W. G. (1971), "Particle Trajectories, Heating, and Breakup in Hypersonic Shock Layers," *AIAA Journal* 9, p. 1040.

Waldman, G. D., Reinecke, W. G., and Glenn, D. C. (1972), "Raindrop Breakup in the Shock Layer of a High-Speed Vehicle," *AIAA Journal* 10, p. 1200.

Wallis, G. B. (1969), *One Dimensional Two-Phase Flow*, McGraw-Hill, Inc.

Walton, J. D. and Gorton, C. W. (1967), "Rain Erosion of Ceramics at High Mach Numbers," Proceedings of the 2nd Meersburg Conference on Rain Erosion and Allied Phenomena, A. A. Fyall and R. B. King, editors.

Walton, J. D. and Harris, J. N. (1966), "Rain Erosion Sled Testing of Slip-Cast Fused Silica Radomes," Final Technical Report, Part I, Project A-925; prepared for U. S. Army Missile Command, Redstone Arsenal, Alabama; Georgia Inst. of Technology.

Wheelahan, E. J. (1967), "State-of-the-Art Survey of Raindrop Erosion," U. S. Army Missile Command Report No. RS-TR-67-13, Redstone Arsenal, Alabama.

Yoffee, E. H. (1951), "The Moving Griffith Crack," Philosophical Magazine, series 7, Vol. 42, pp. 739-750.
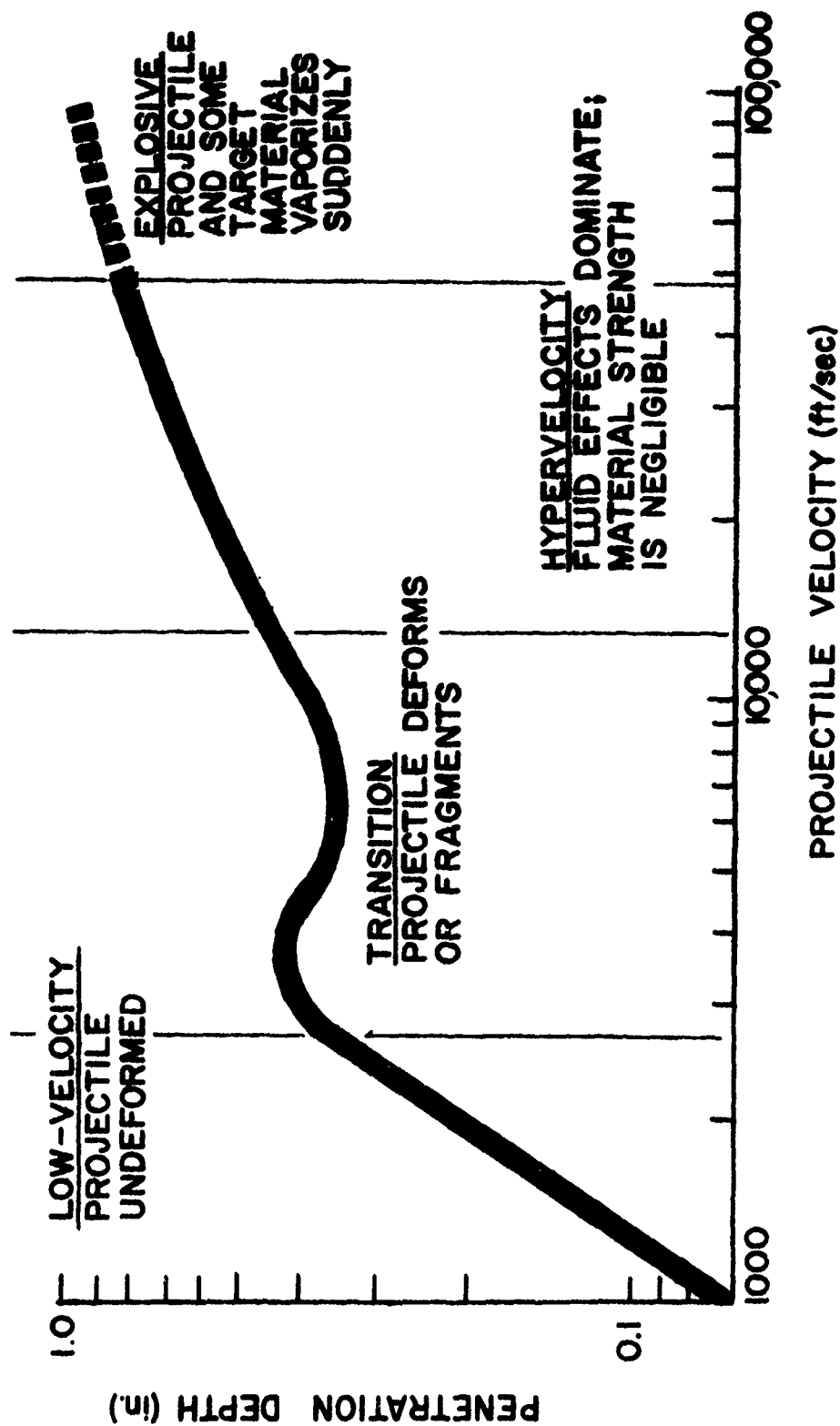
FIGURE 1.1. REGIMES OF IMPACT PHENOMENA
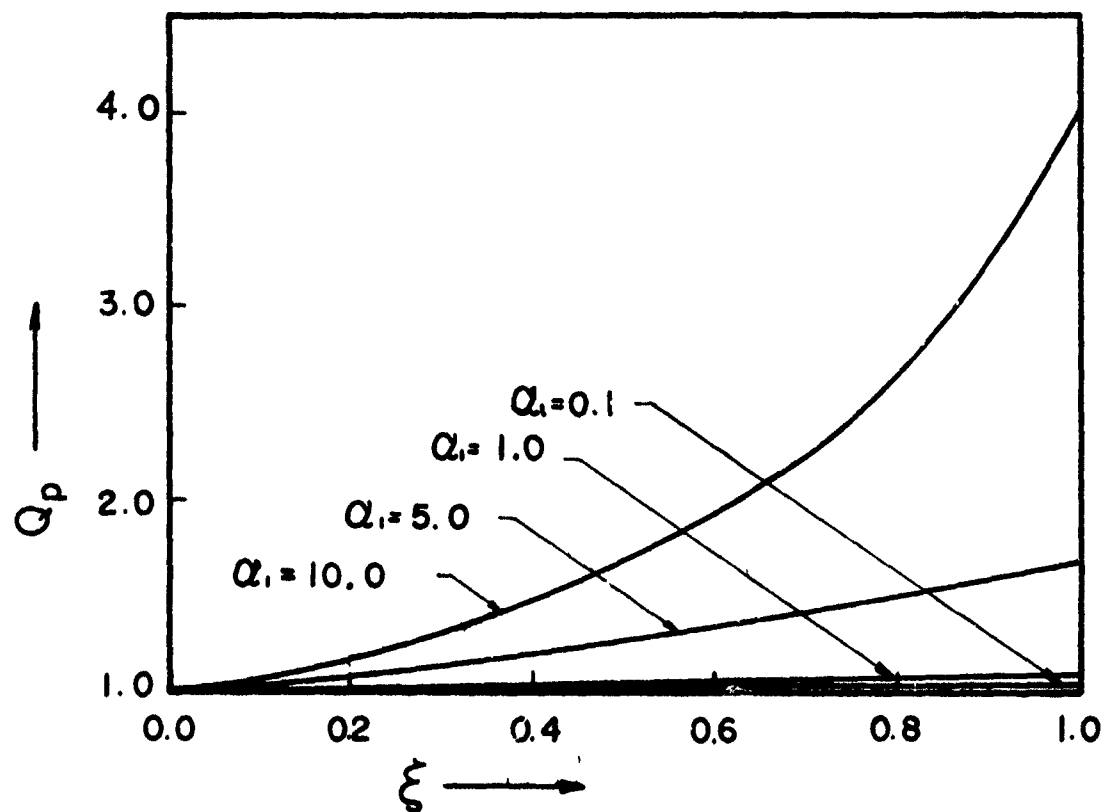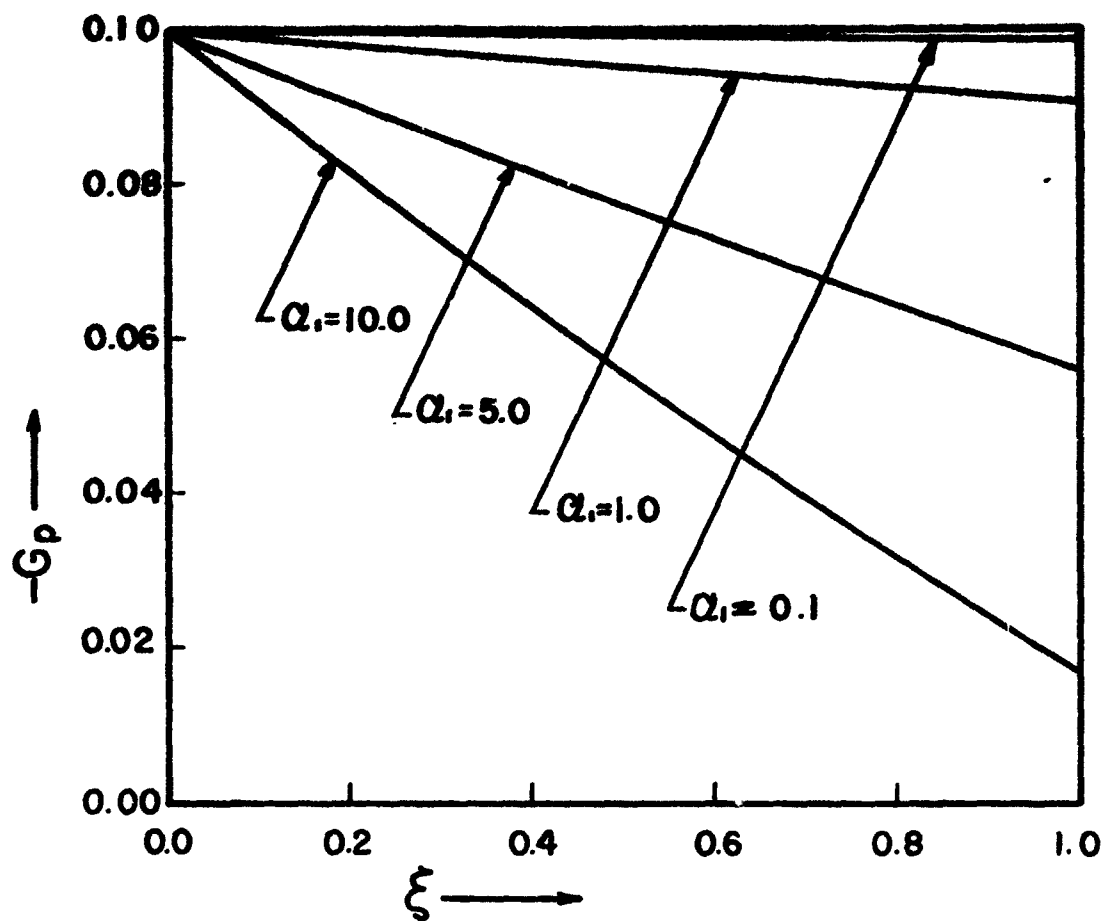
FIGURE 2.1. SURFACE DISTRIBUTIONS OF DROP-PHASE NORMAL VELOCITY AND
DROP-PHASE DENSITY (WEDGE)
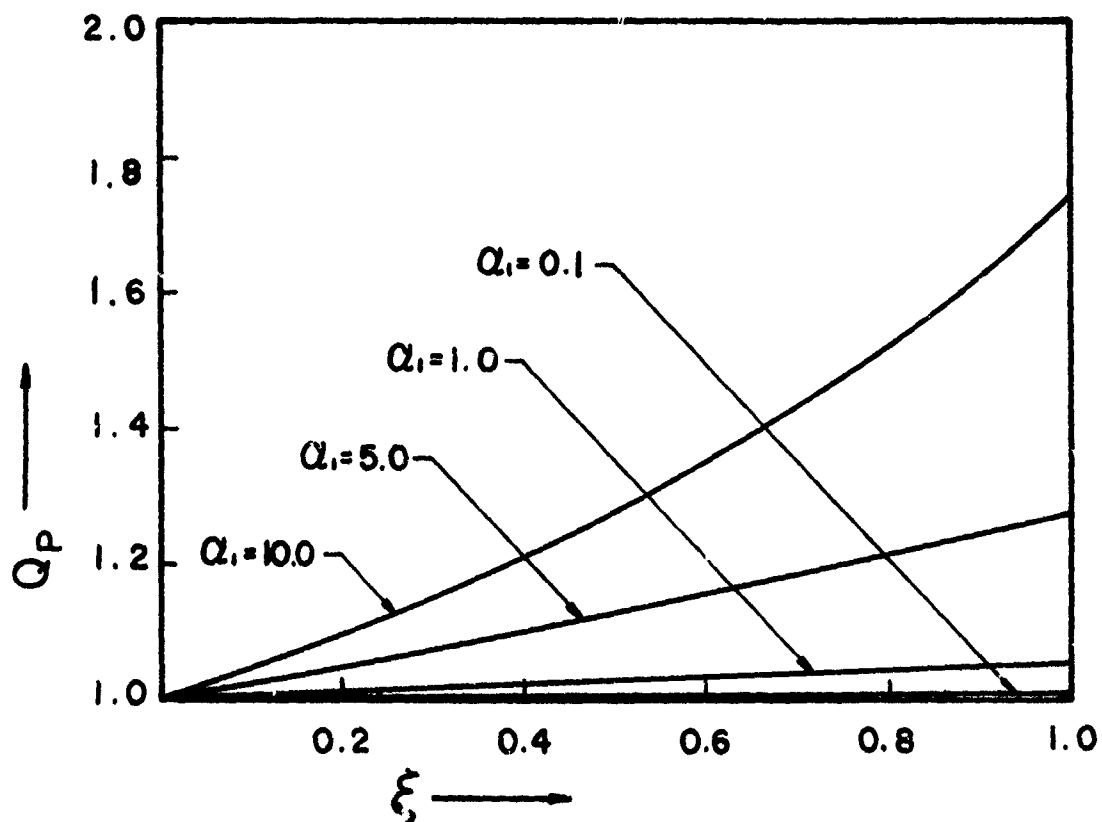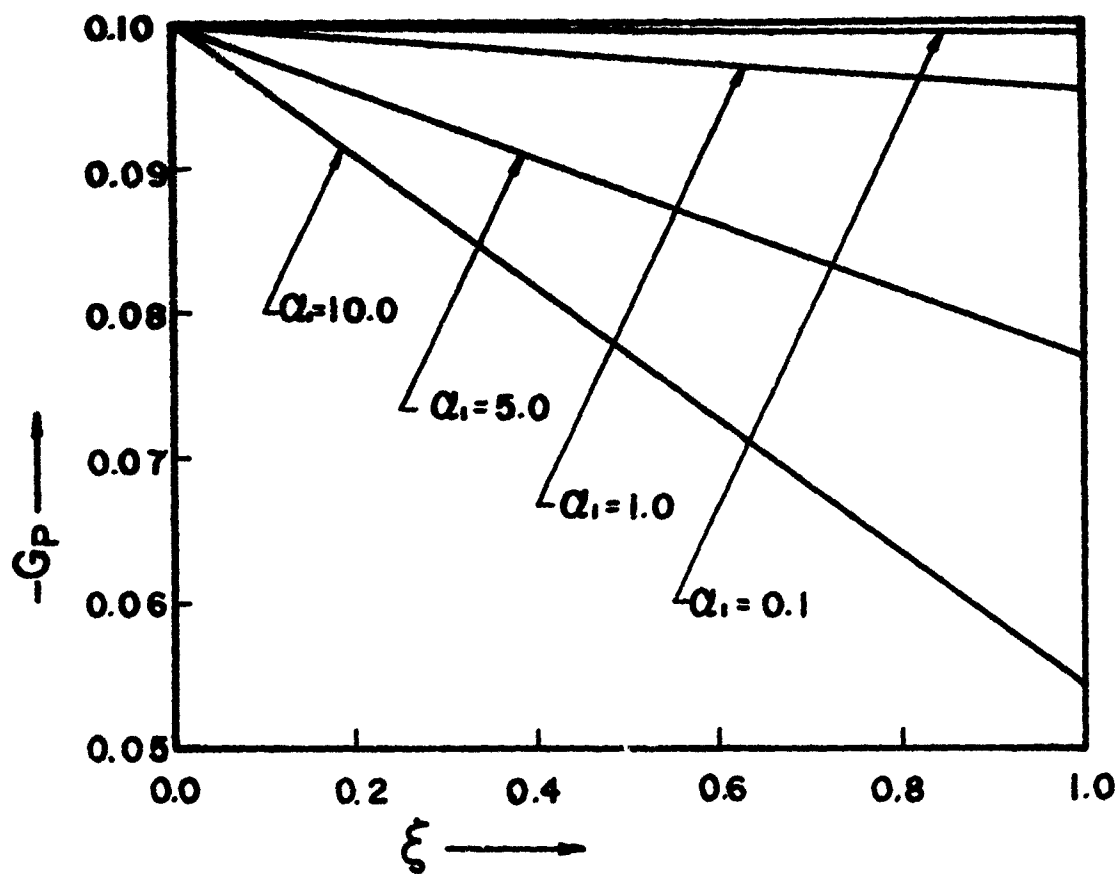
FIGURE 2.2.   SURFACE DISTRIBUTIONS OF DROP-PHASE NORMAL VELOCITY AND
DROP-PHASE DENSITY (CONE)
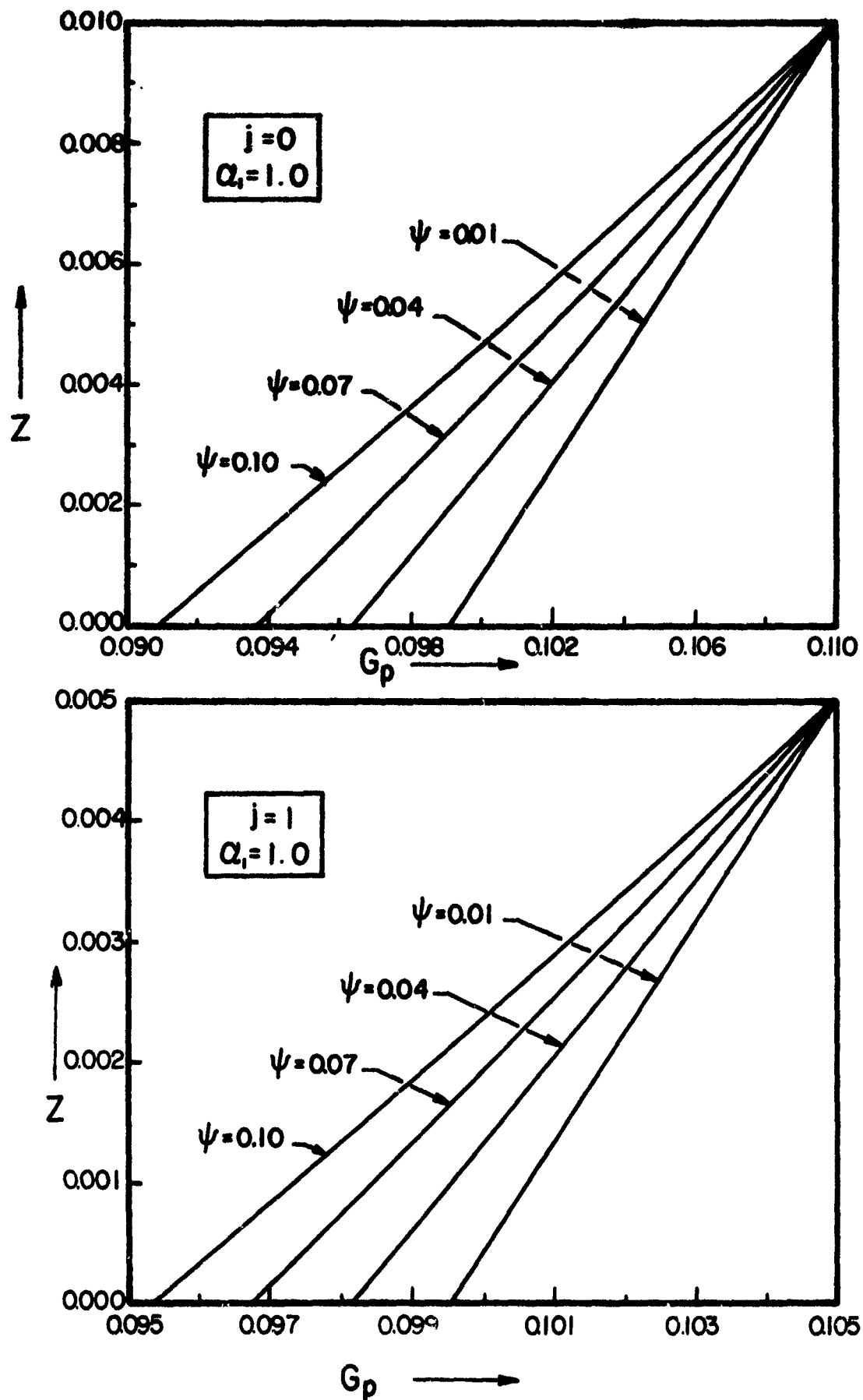
FIGURE 2.3. DROP-PHASE NORMAL-VELOCITY VARIATIONS ALONG SELECTED STREAMLINES
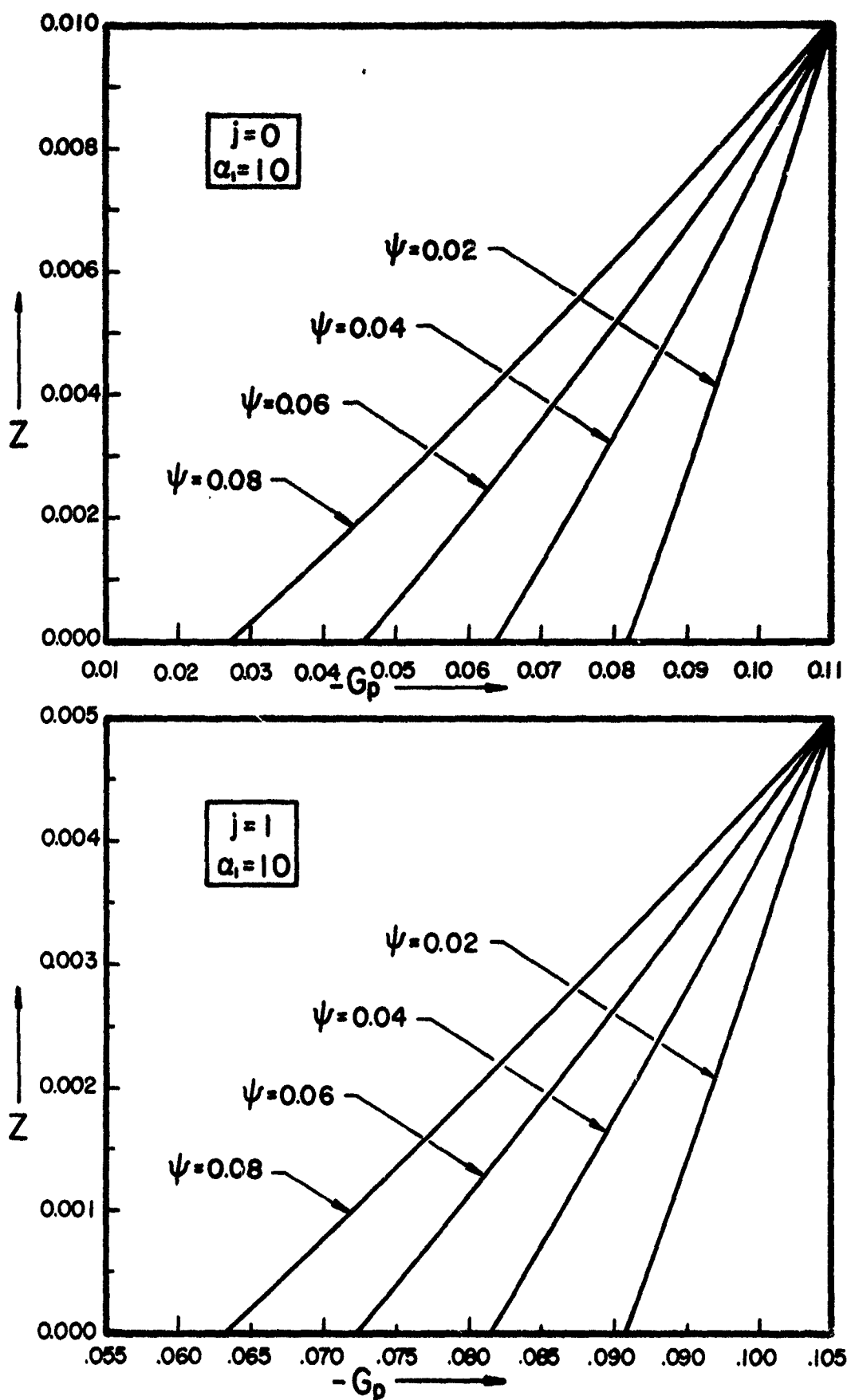
FIGURE 2.4.   DROP-PHASE NORMAL-VELOCITY VARIATIONS ALONG SELECTED
             STREAMLINES
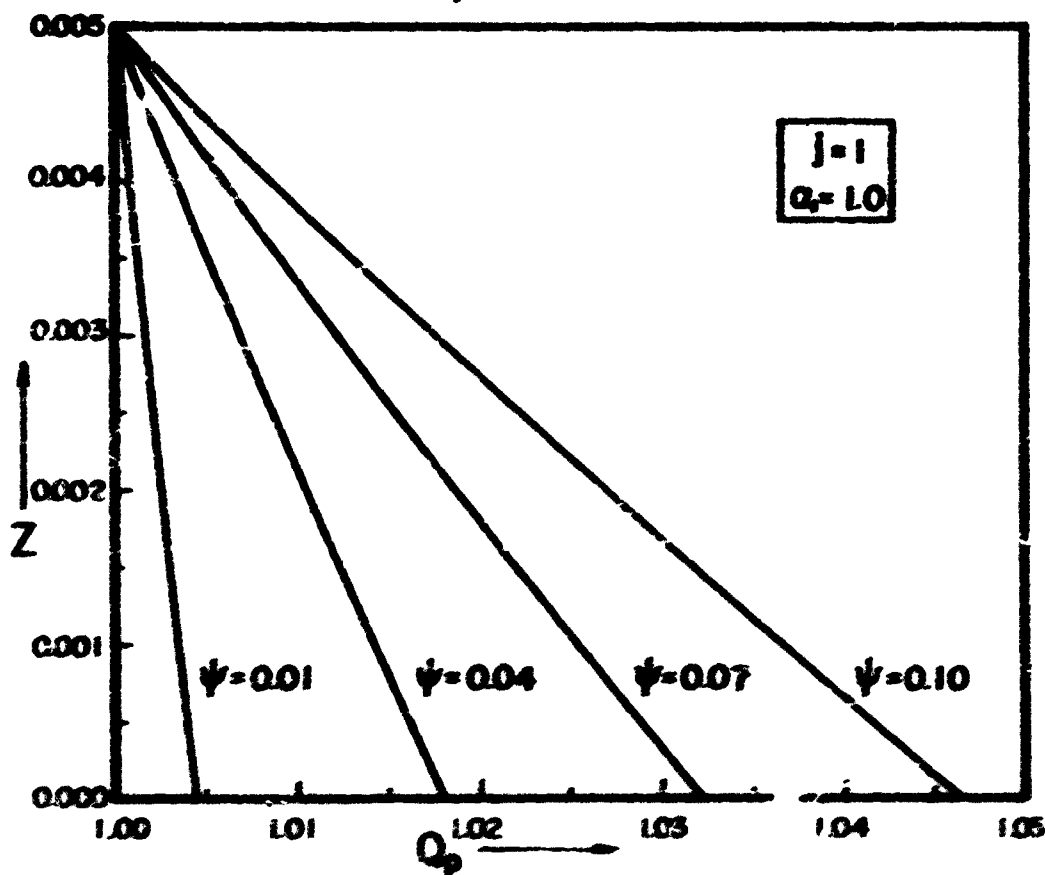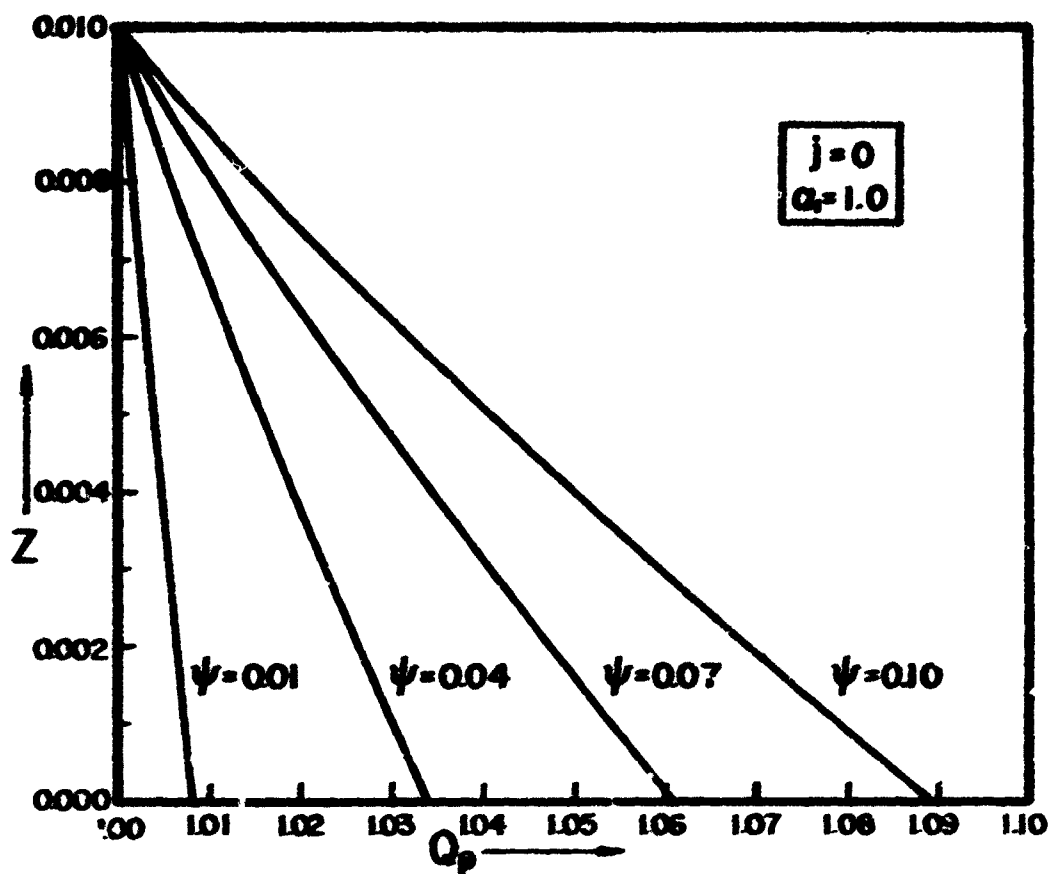
FIGURE 2.5. DROP-PHASE DENSITY VARIATIONS ALONG SELECTED STREAMLINES
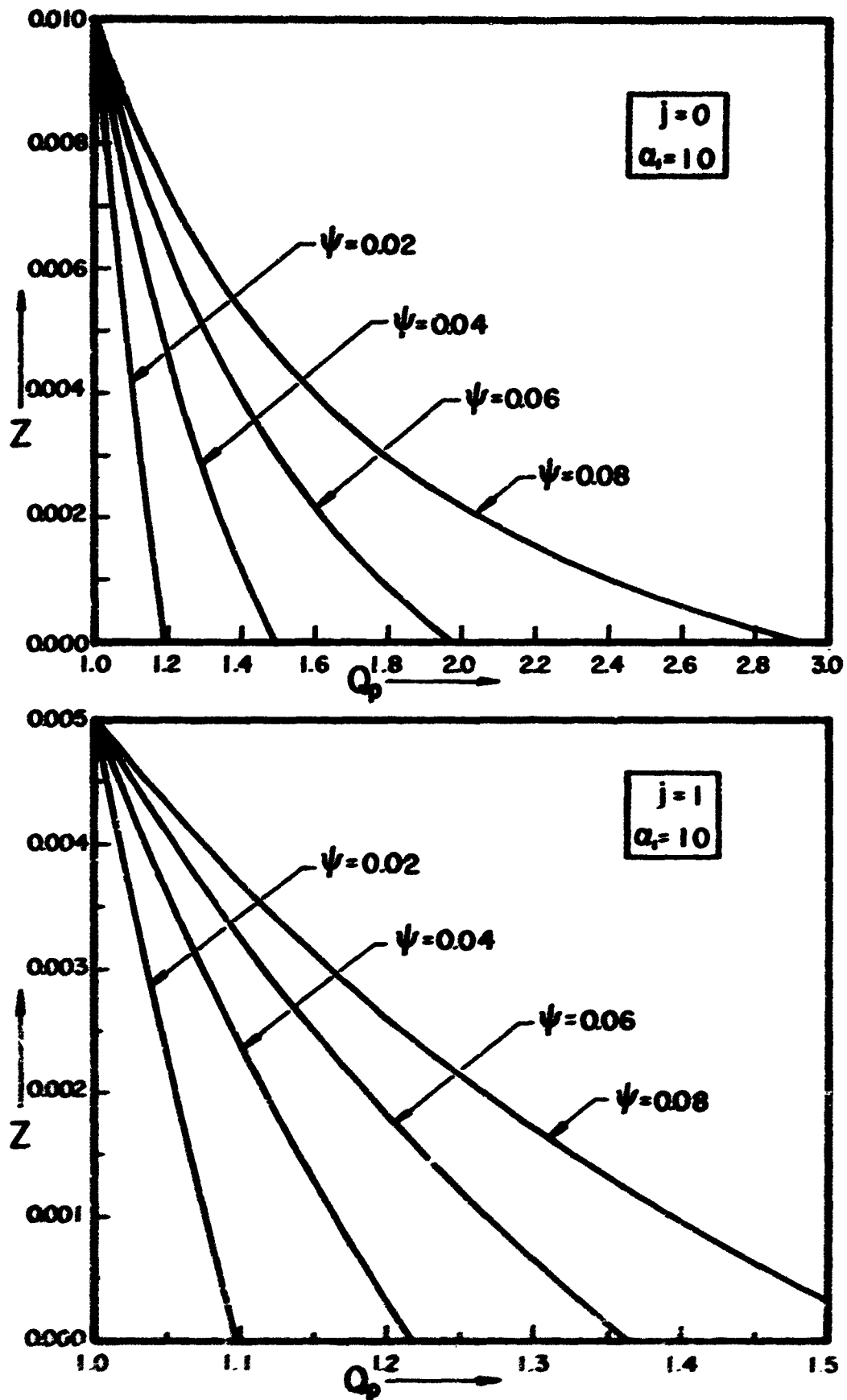
FIGURE 2.6. DROP-PHASE DENSITY VARIATIONS ALONG SELECTED STREAMLINES
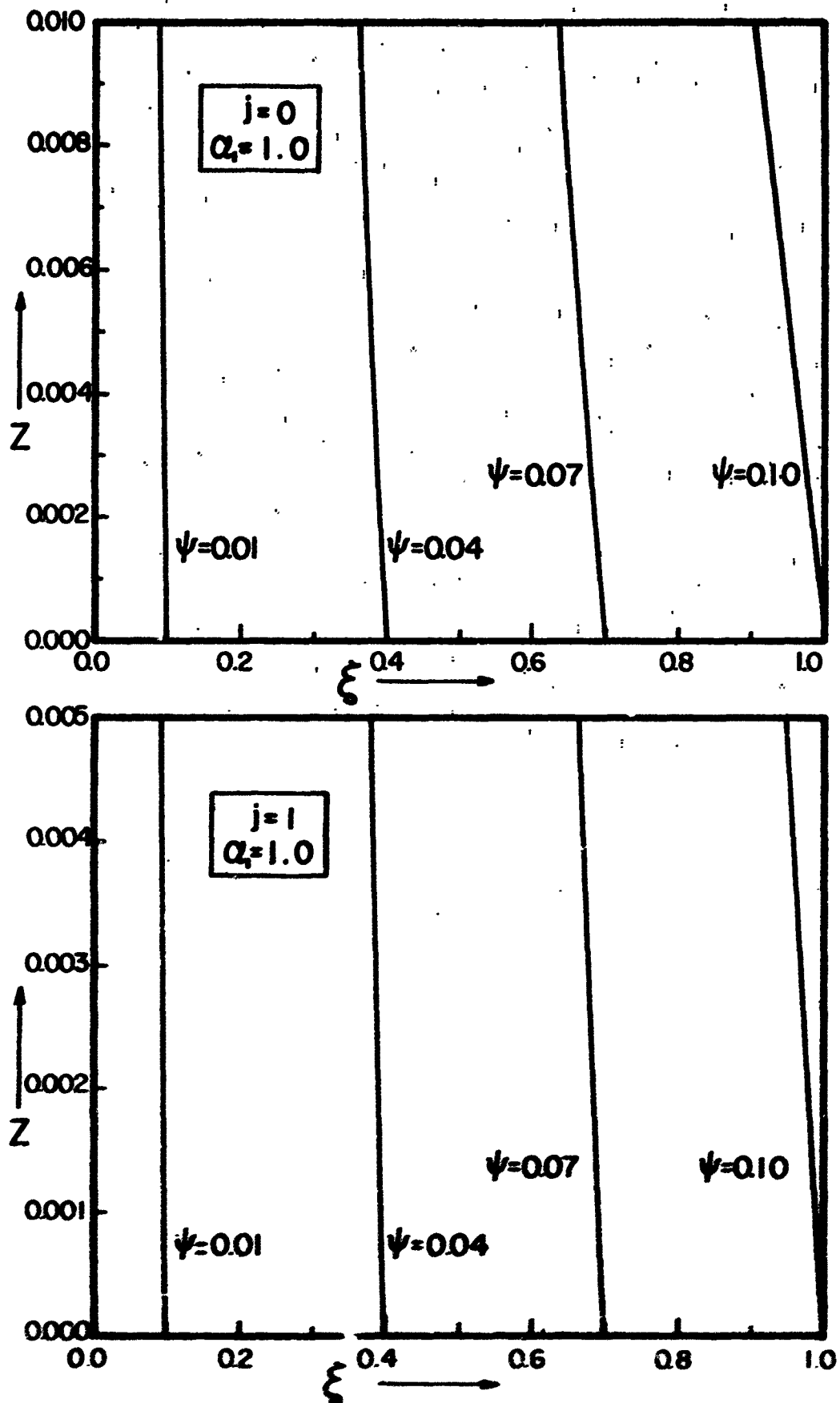
FIGURE 2.7. SELECTED DROP-PHASE STREAMLINES
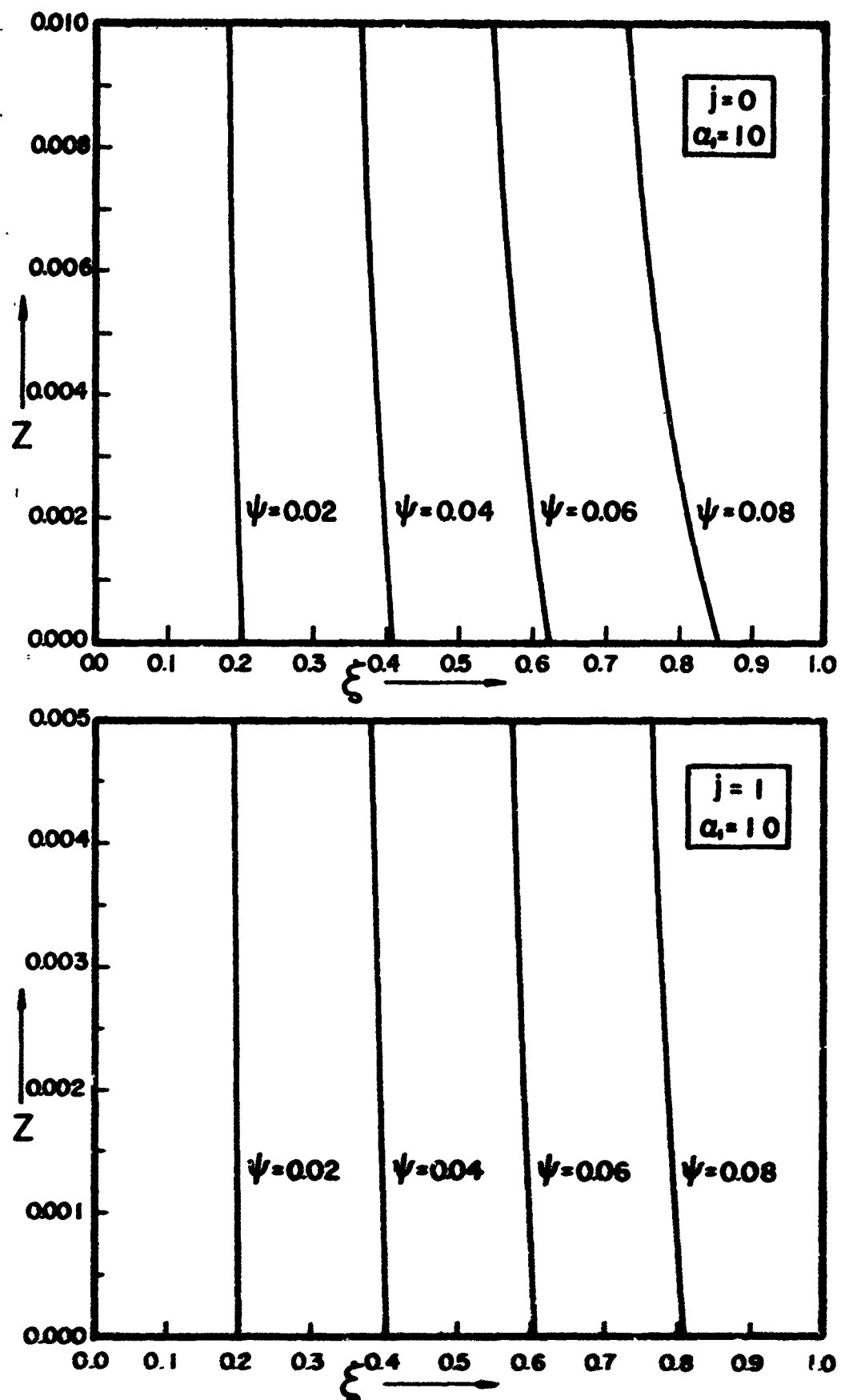
FIGURE 2.8. SELECTED DROP-PHASE STREAMLINES
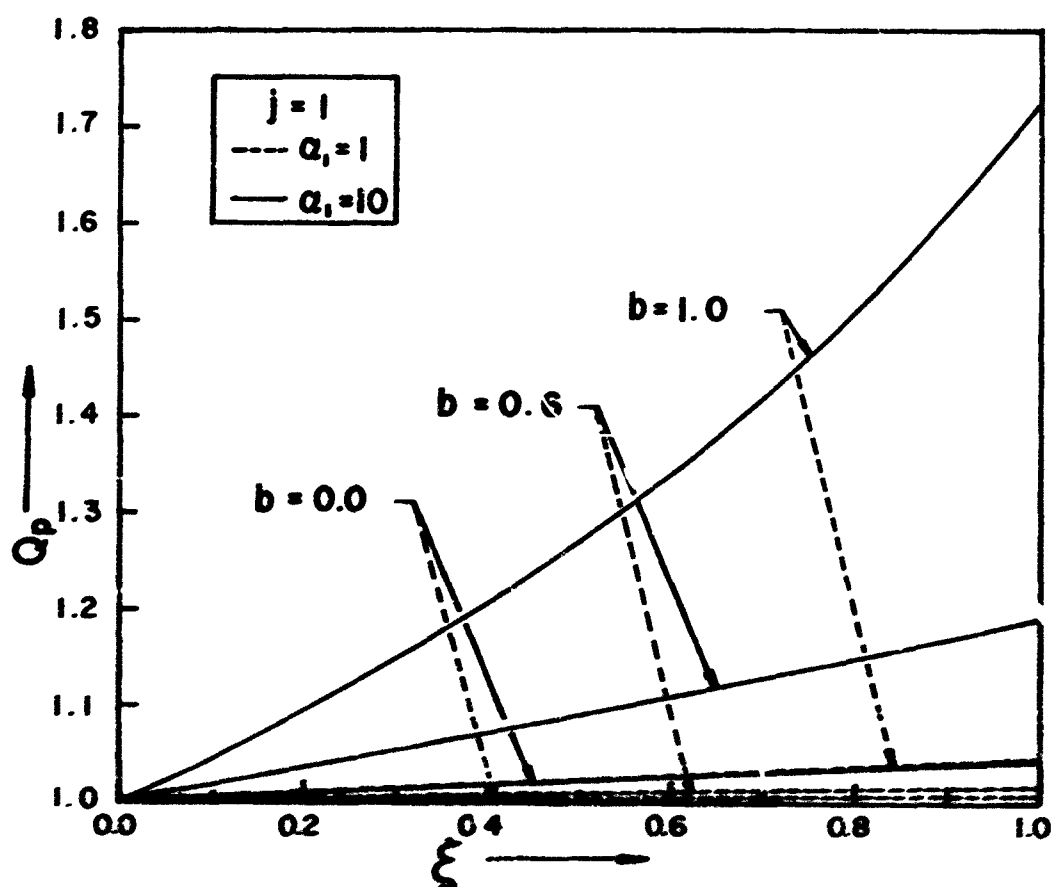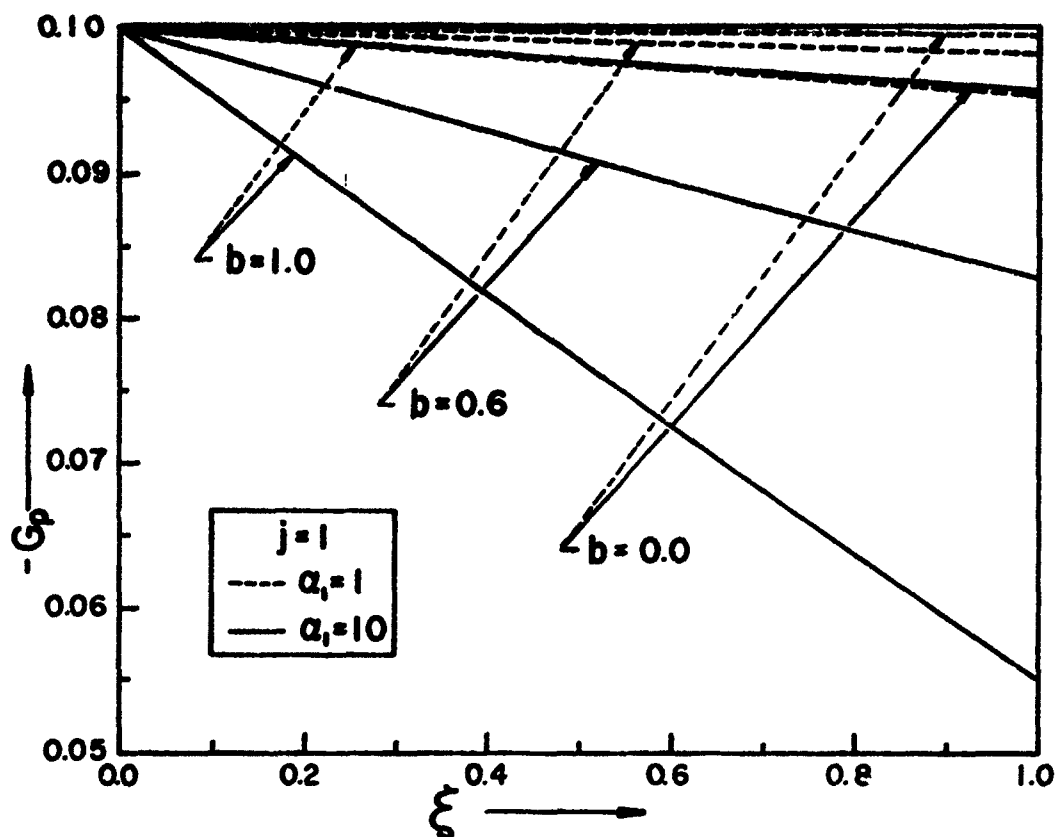
FIGURE 2.5. SURFACE DISTRIBUTIONS OF DROP-PHASE NORMAL VELOCITY AND DROP-PHASE DENSITY
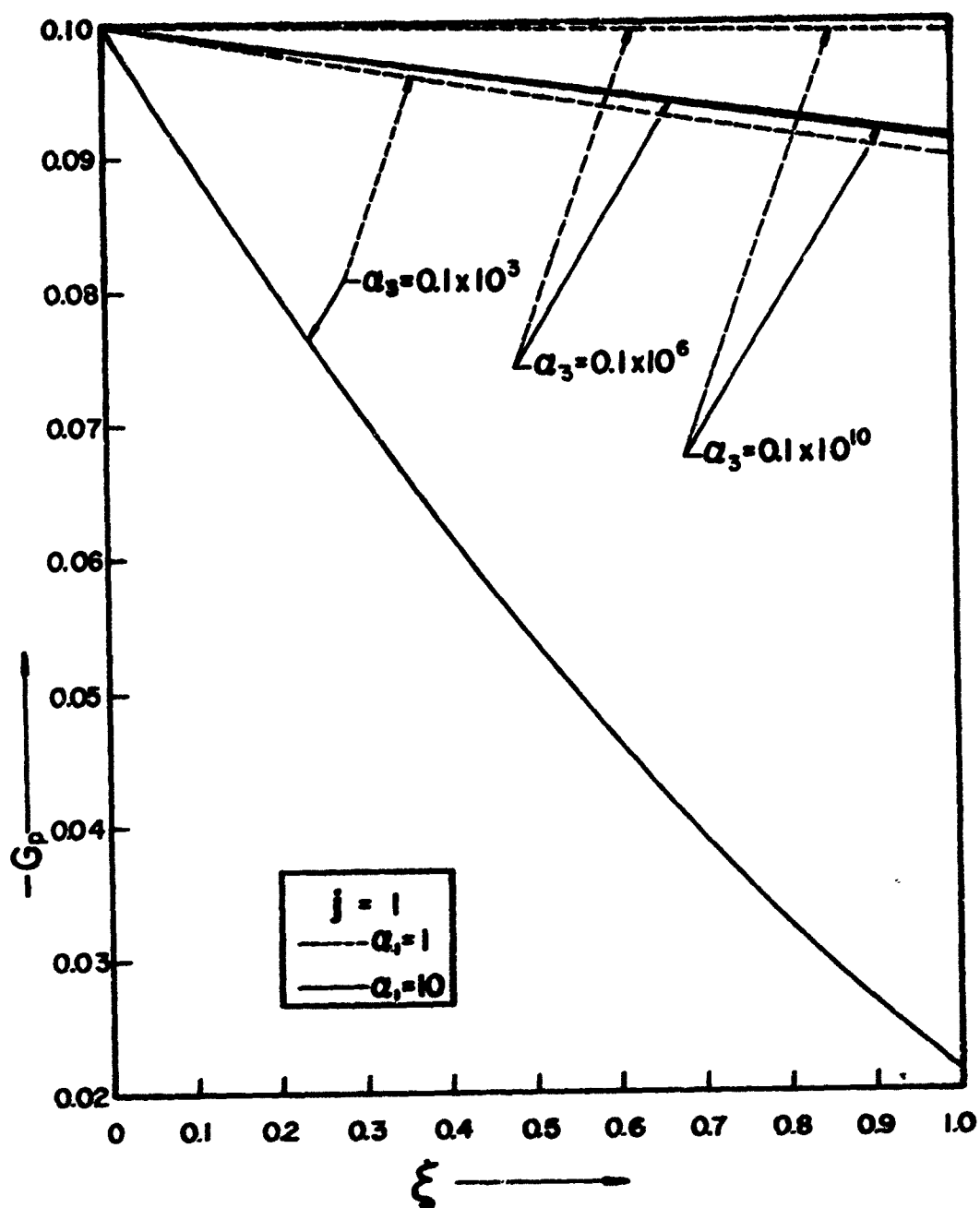
FIGURE 2.10. SURFACE DISTRIBUTION OF DROP-PHASE NORMAL VELOCITY
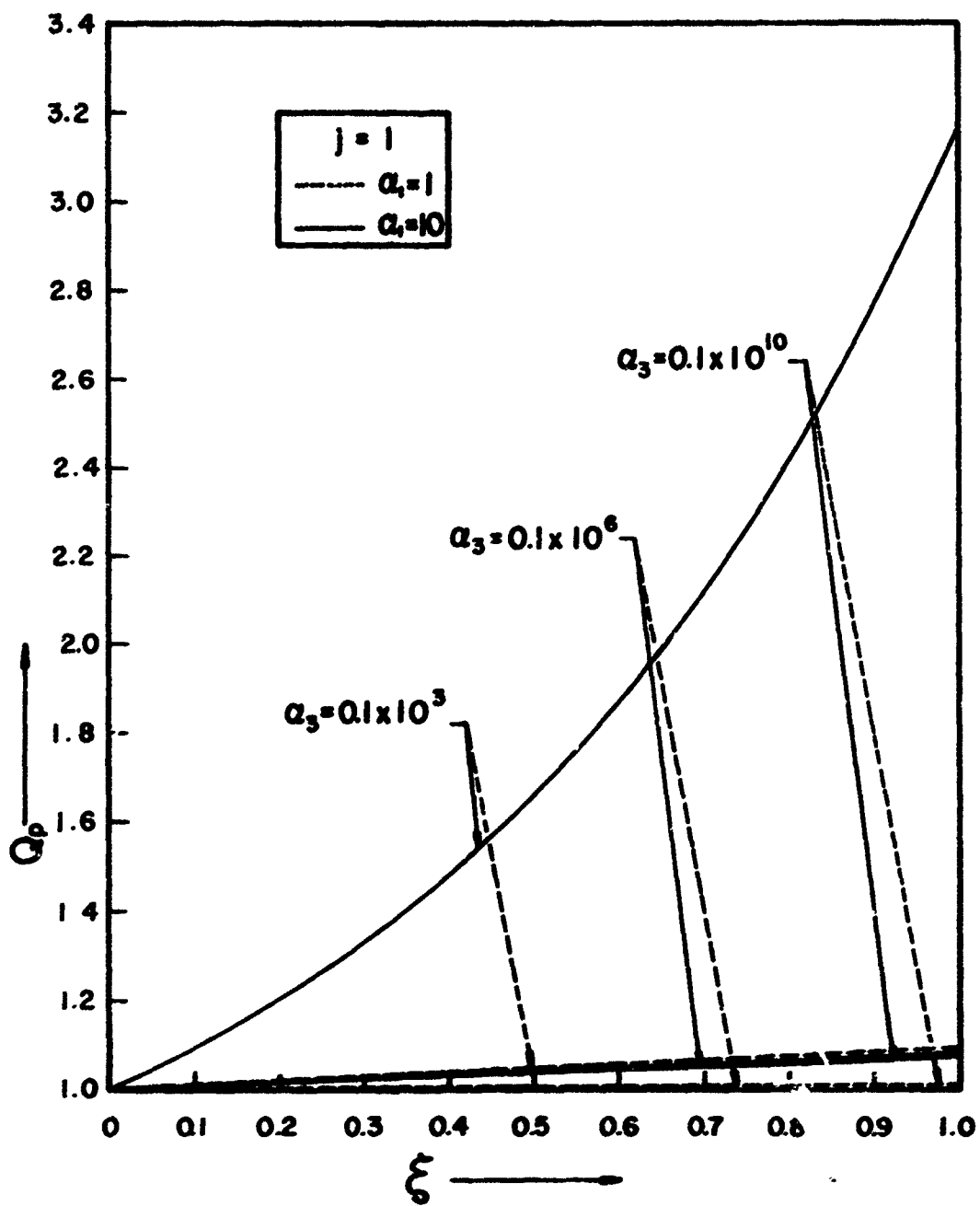
FIGURE 2.11. SURFACE DISTRIBUTION OF DROP-PHASE DENSITY
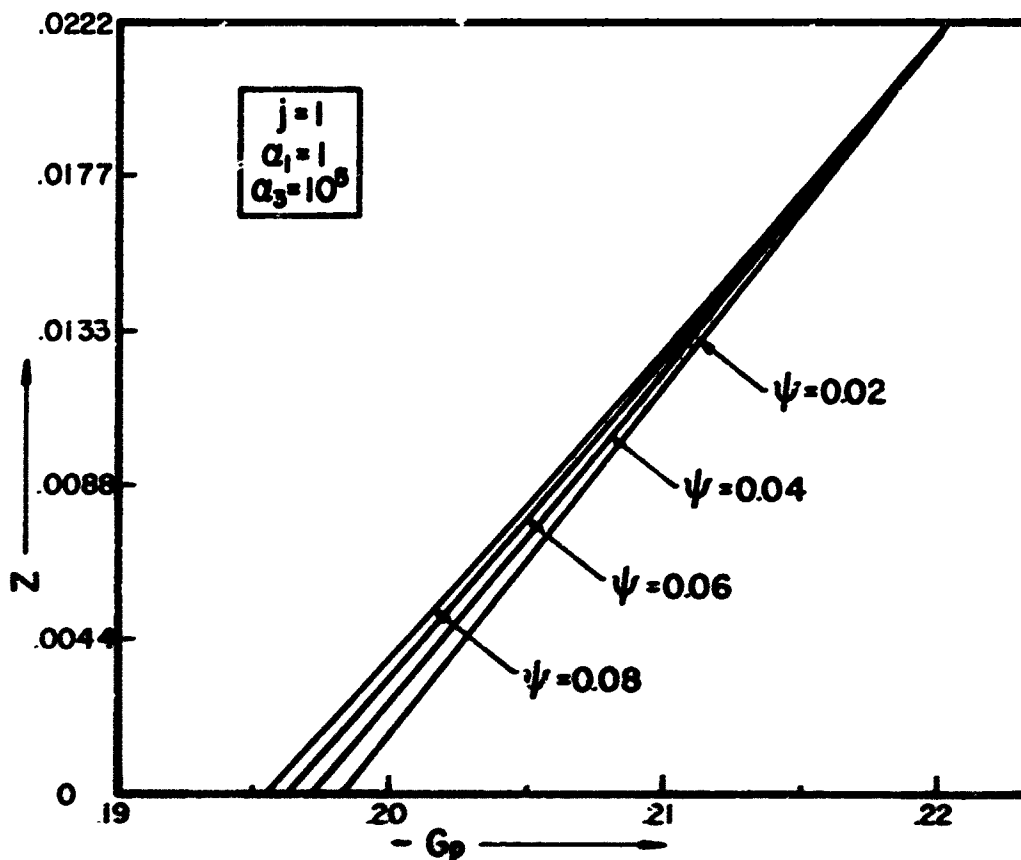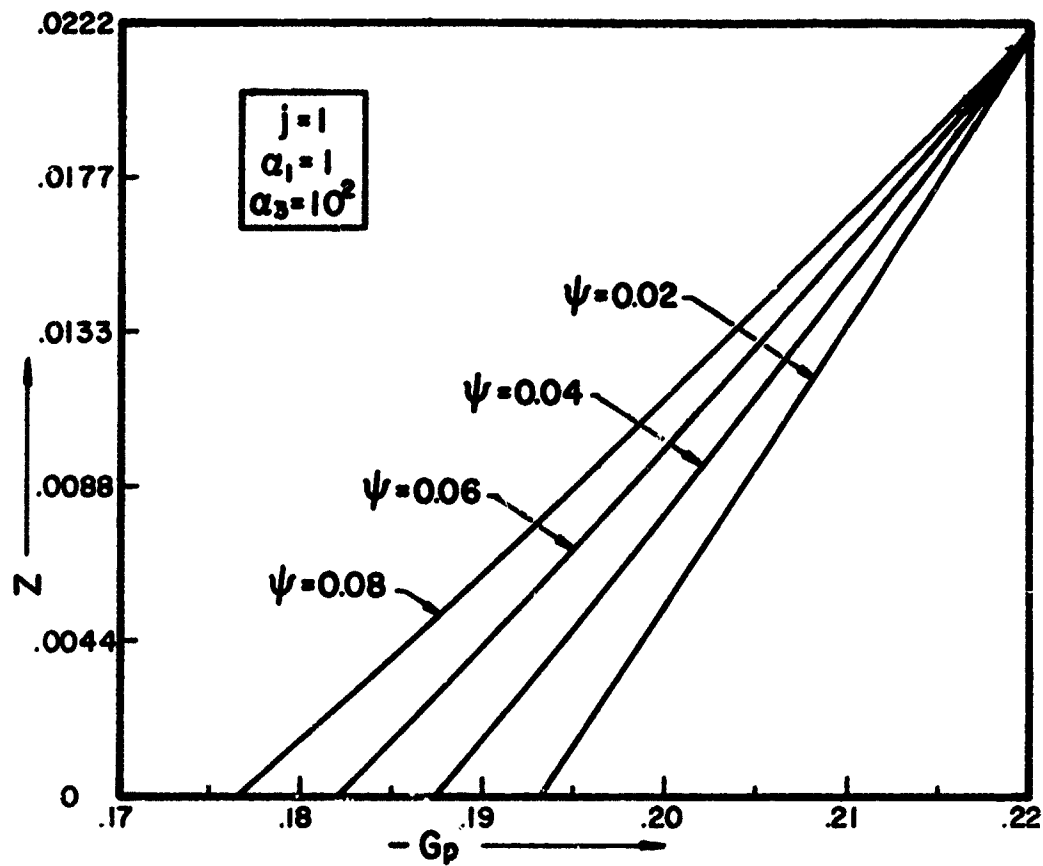
FIGURE 2.12. DROP-PHASE TRANSVERSE-VELOCITY VARIATIONS ALONG
SELECTED STREAMLINES
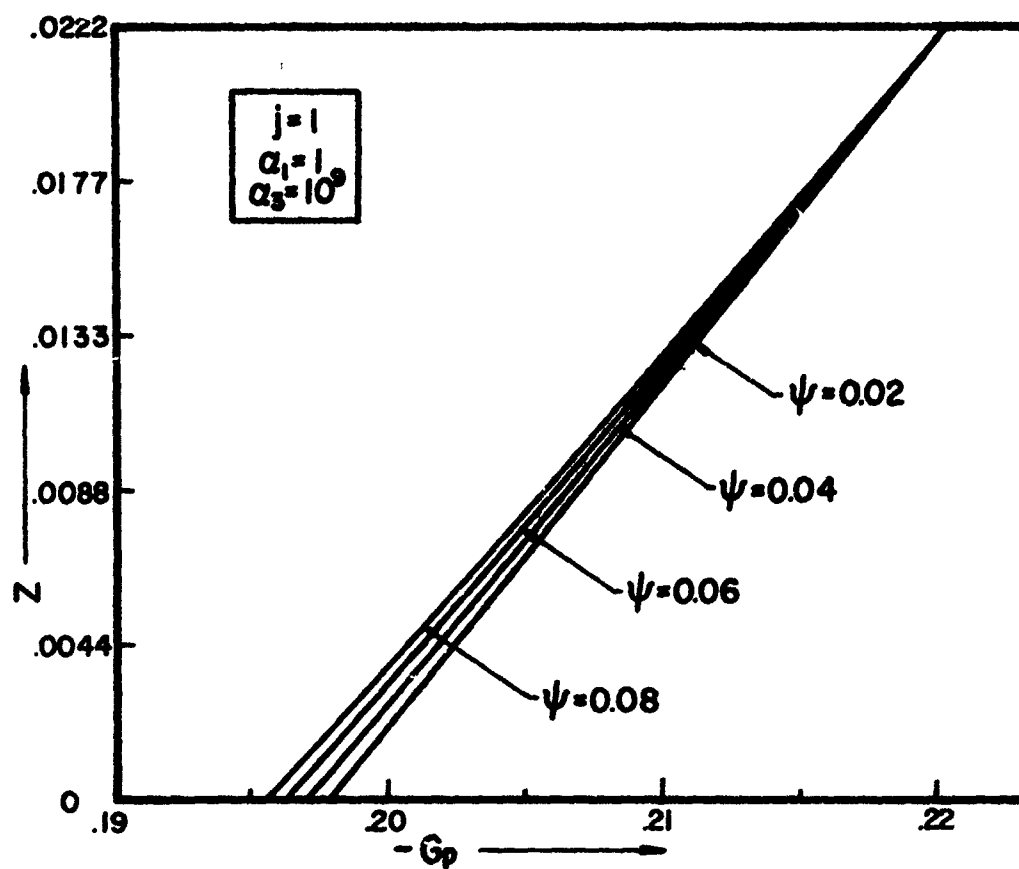
FIGURE 2.13. DROP-PHASE TRANSVERSE-VELOCITY VARIATIONS ALONG SELECTED STREAMLINES
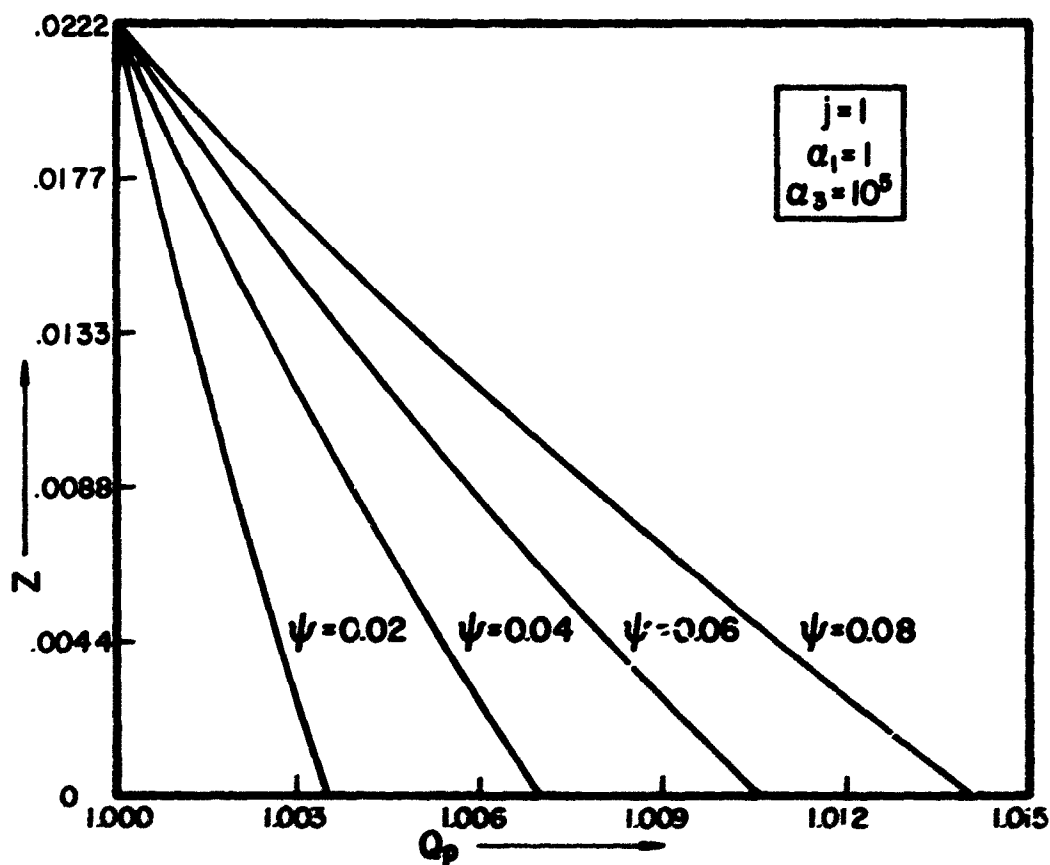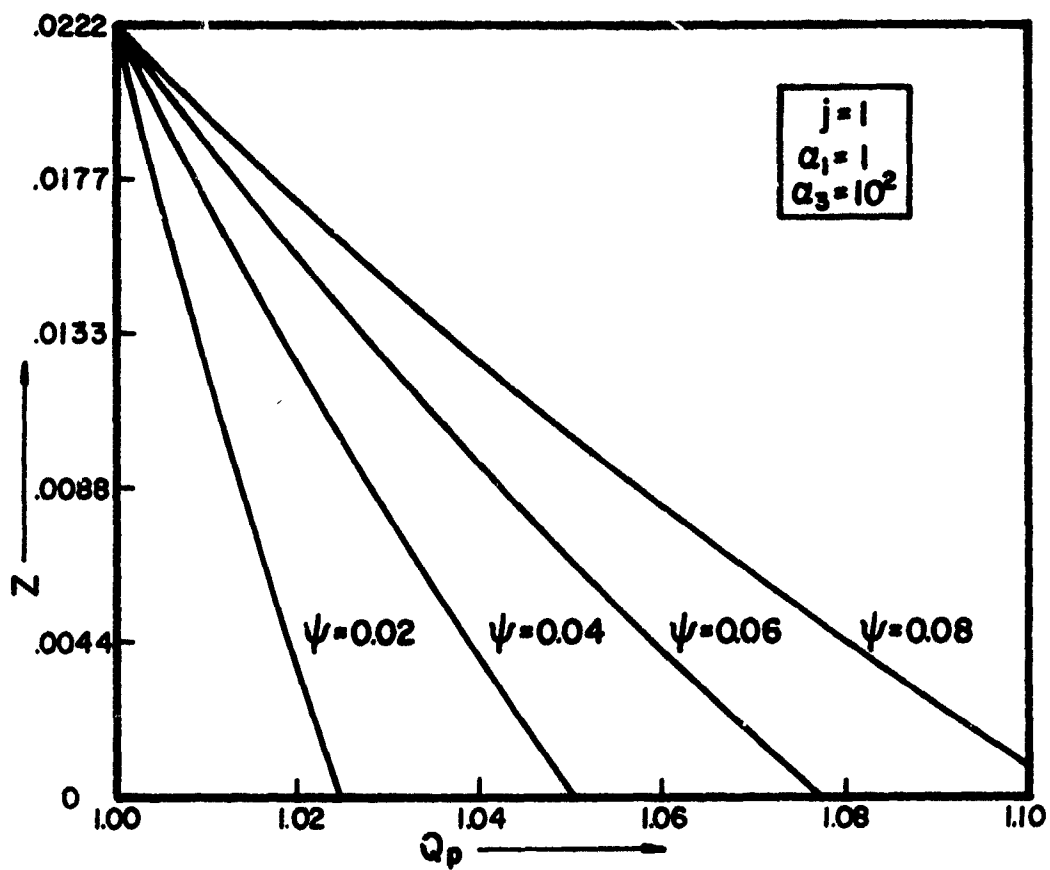
FIGURE 2.14.   DROP-PHASE DENSITY VARIATIONS ALONG SELECTED STREAMLINES
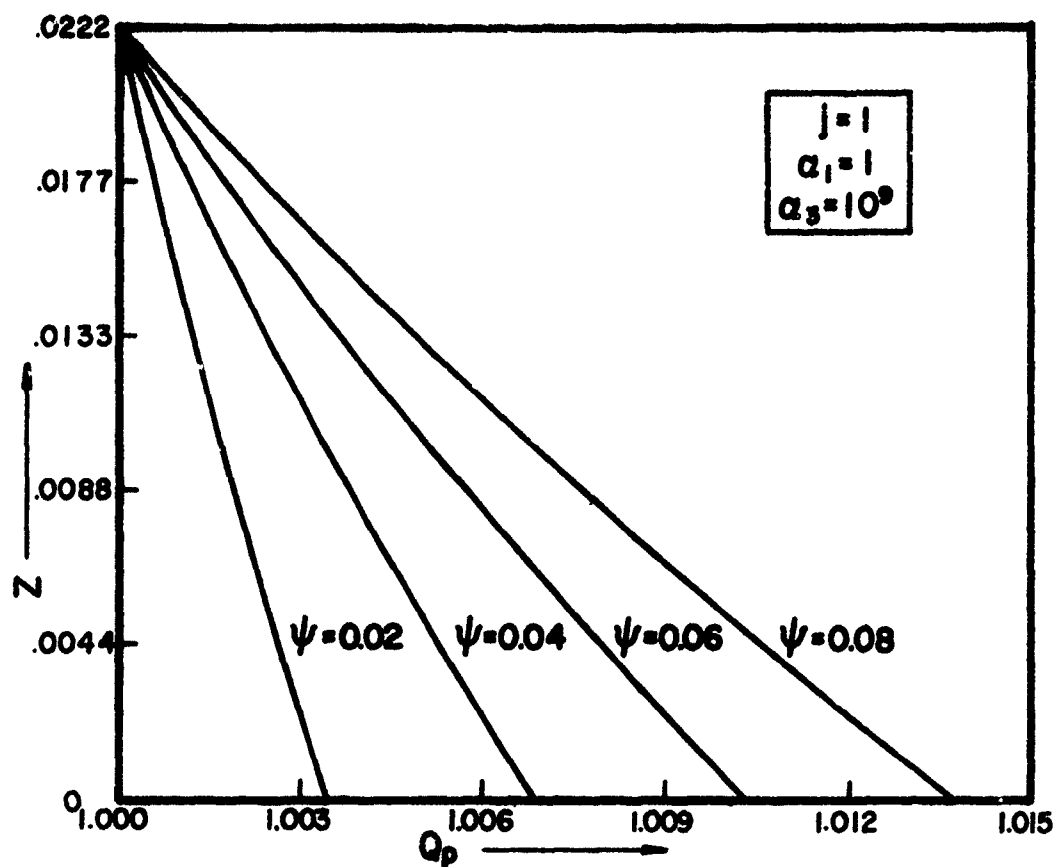
FIGURE 2.15. DROP-PHASE DENSITY VARIATIONS ALONG SELECTED STREAMLINES
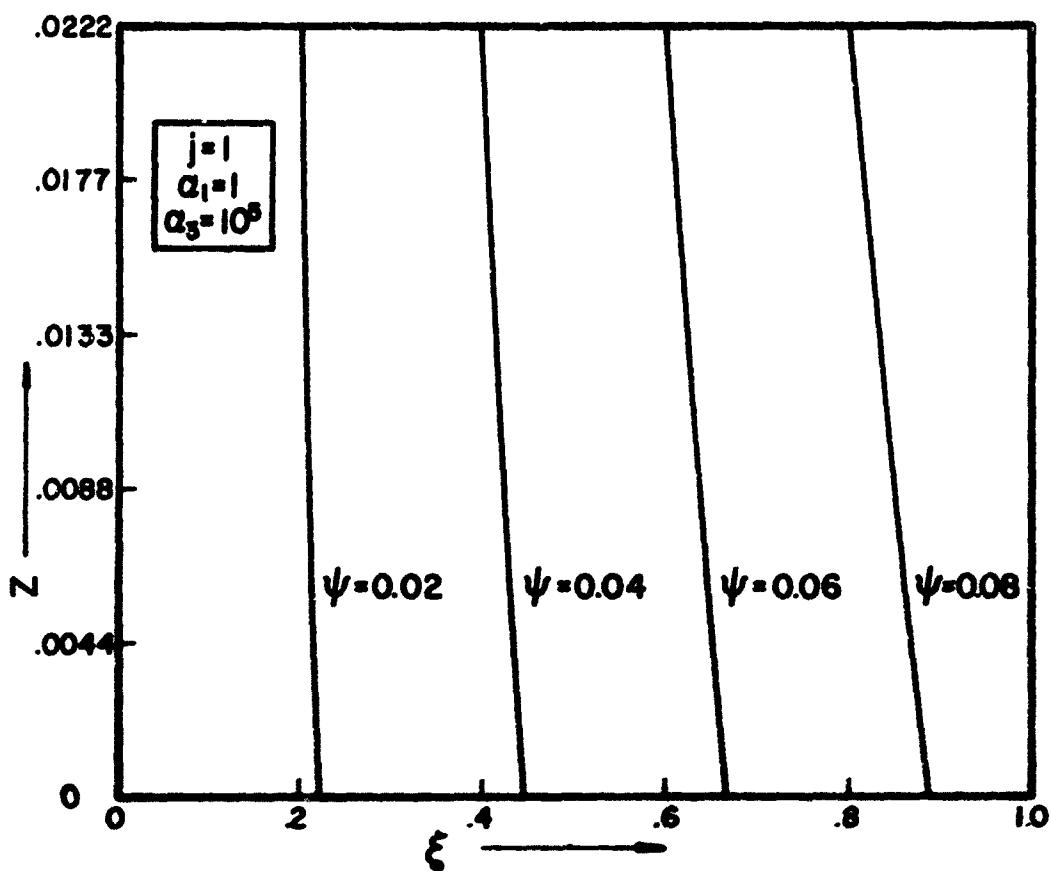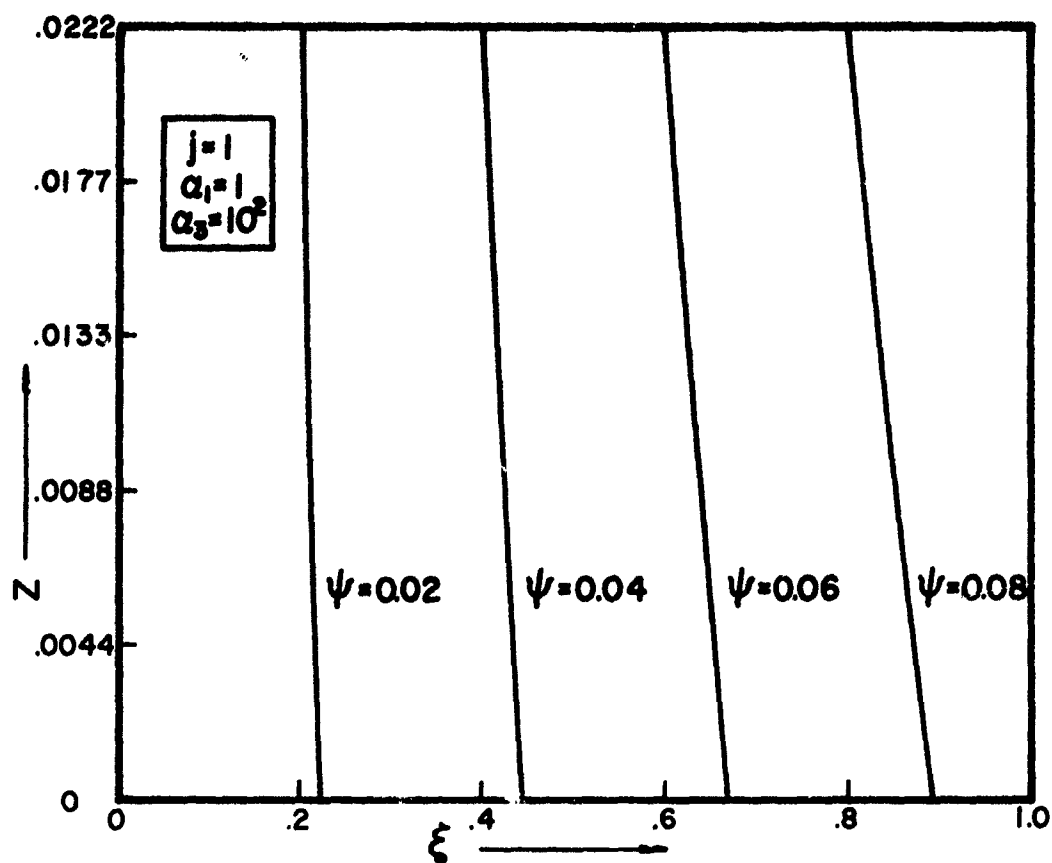
FIGURE 2.16. SELECTED DROP-PHASE STREAMLINES
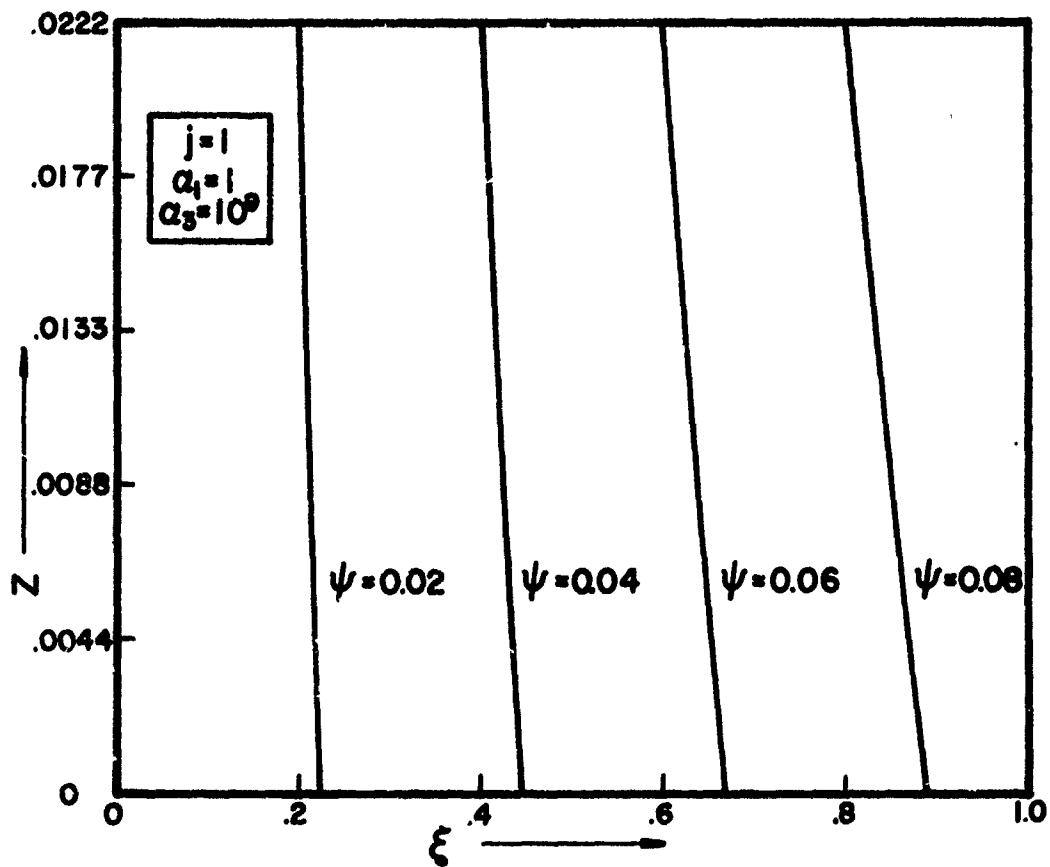
FIGURE 2.17.   SELECTED DROP-PHASE STREAMLINES
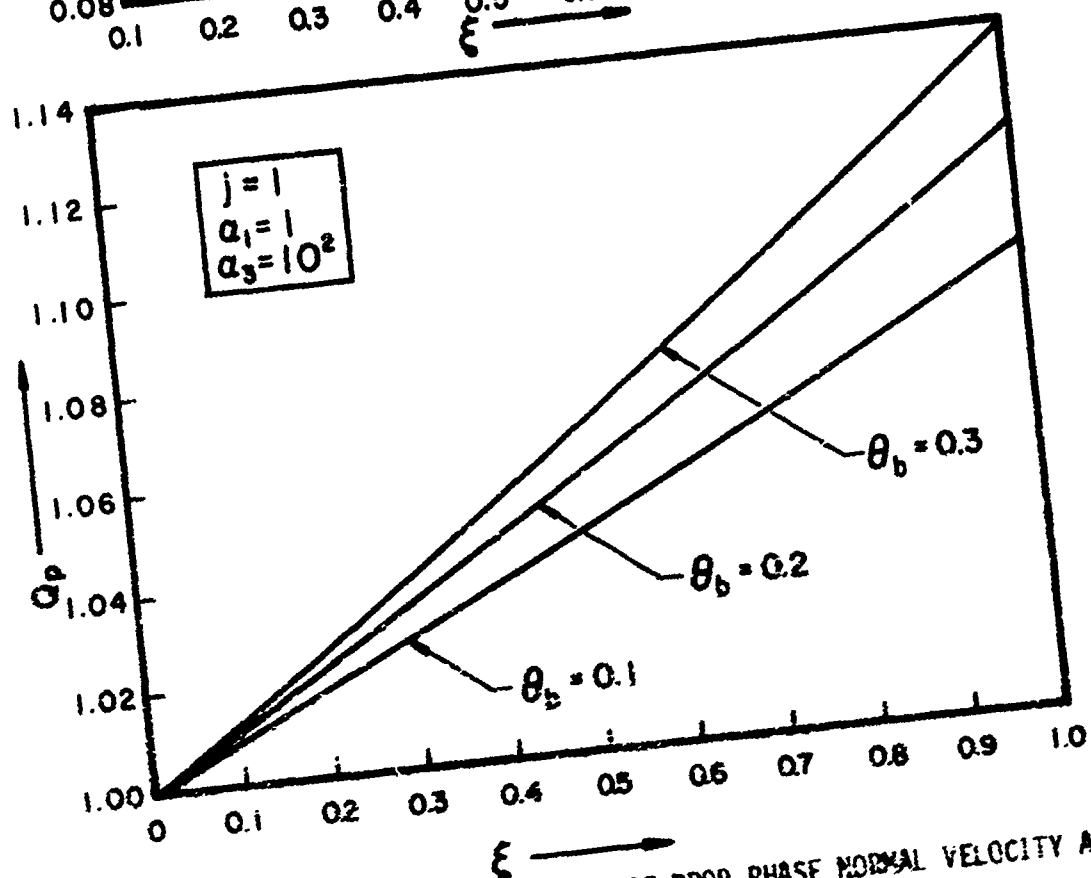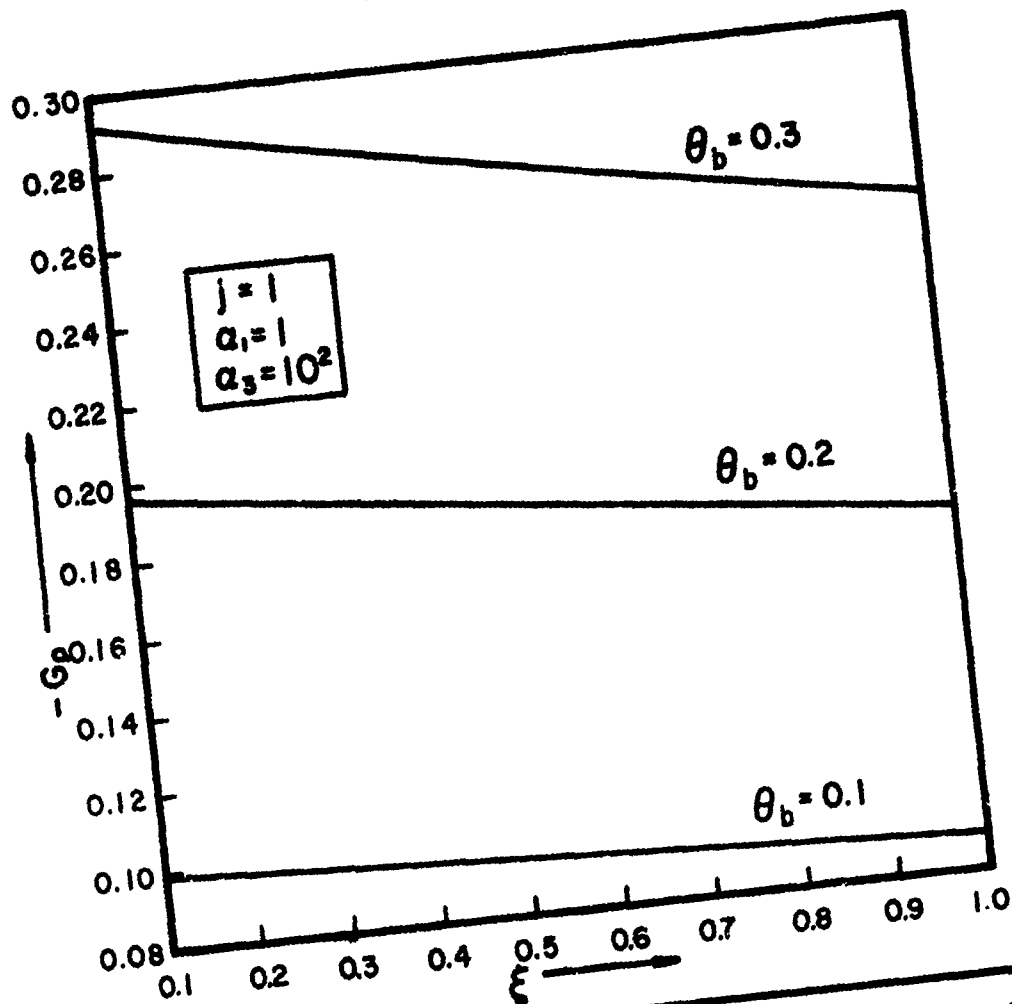
FIGURE 2.18. SURFACE DISTRIBUTIONS OF DROP-PHASE NORMAL VELOCITY AND DROP-PHASE DENSITY
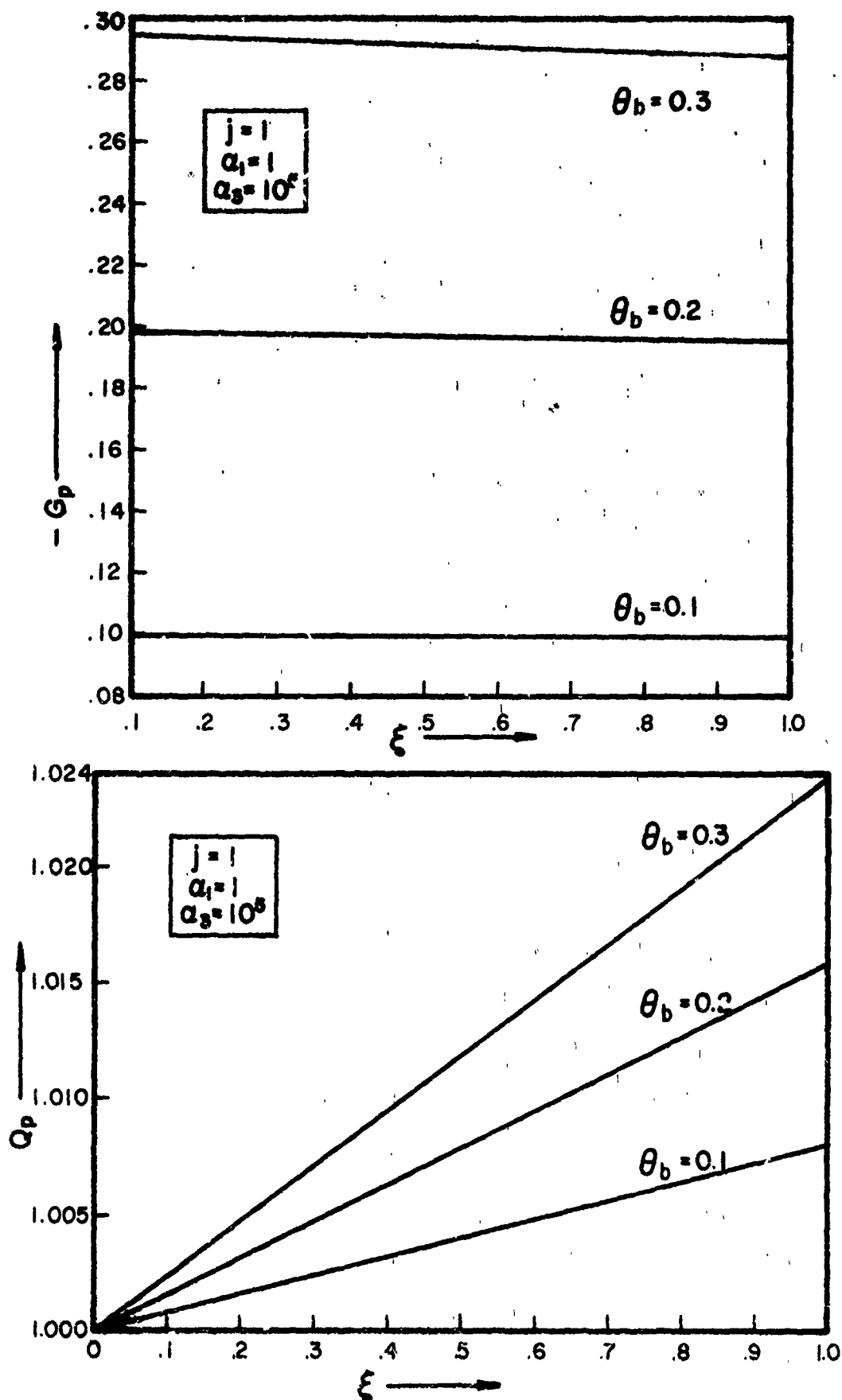
FIGURE 2.19. SURFACE DISTRIBUTIONS OF DROP-PHASE NORMAL VELOCITY
AND DROP-PHASE DENSITY
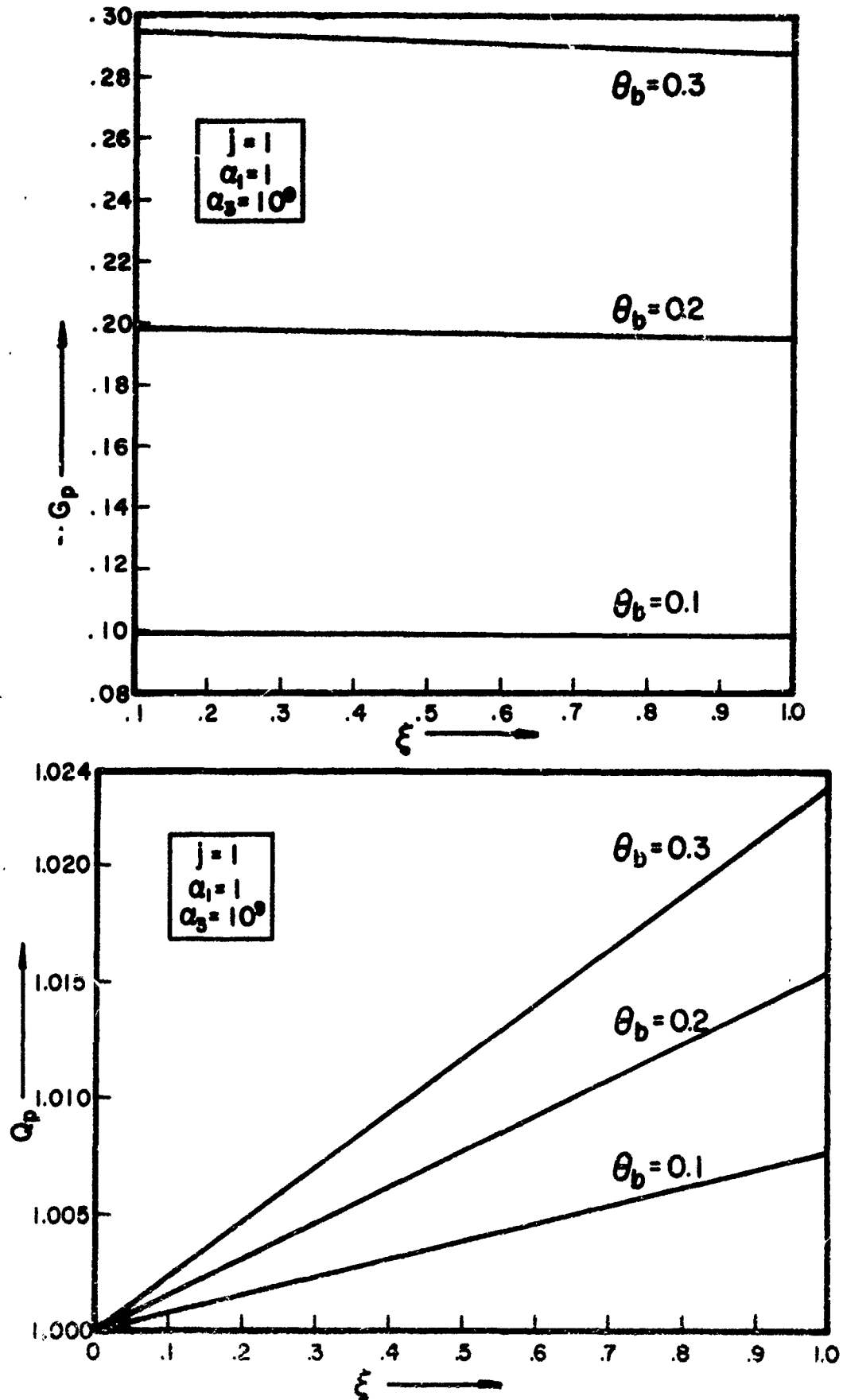
FIGURE 2.20.   SURFACE DISTRIBUTIONS OF DROP-PHASE NORMAL VELOCITY
AND DROP-PHASE DENSITY
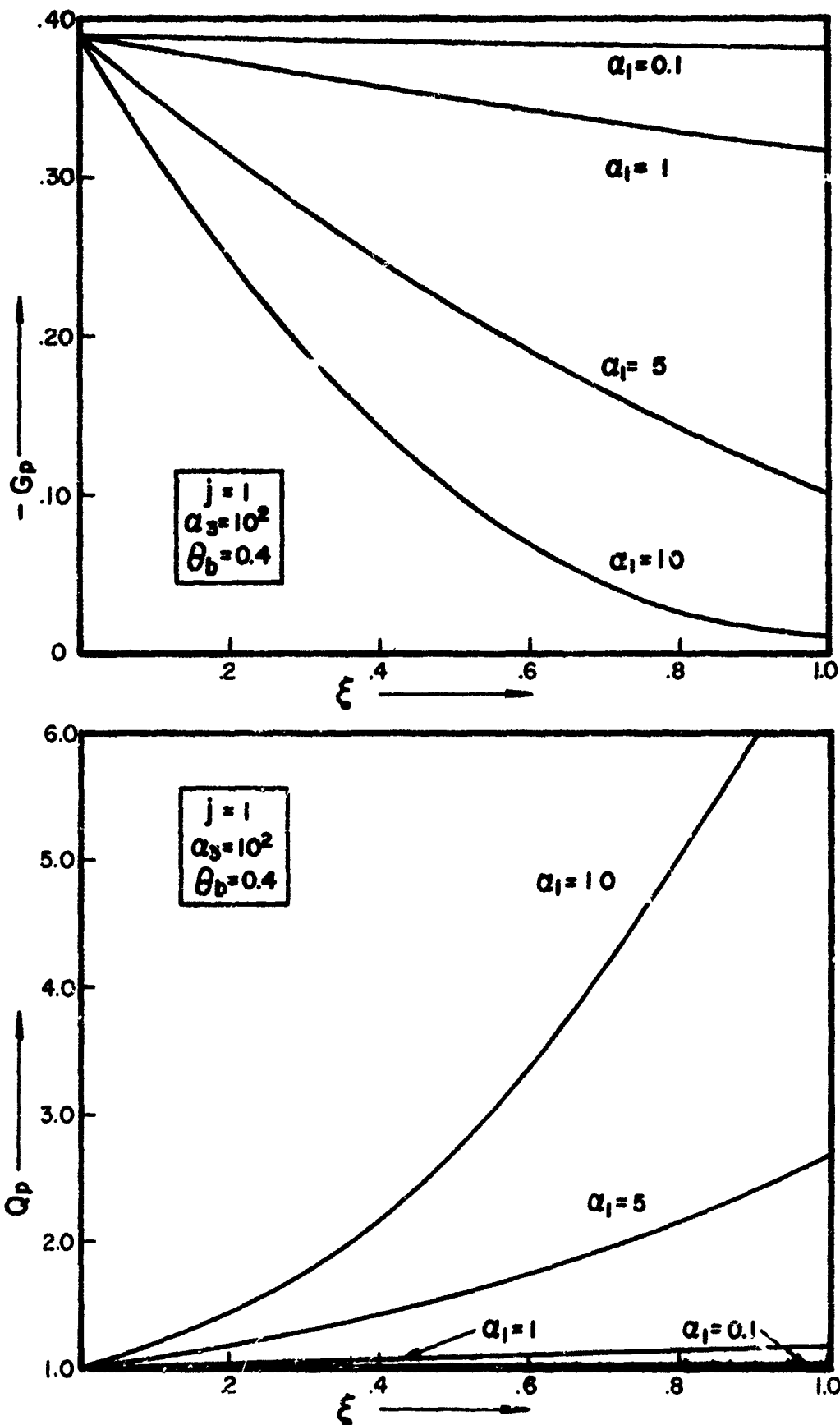
FIGURE 2.21.   SURFACE DISTRIBUTIONS OF DROP-PHASE NORMAL VELOCITY
              AND DROP-PHASE DENSITY
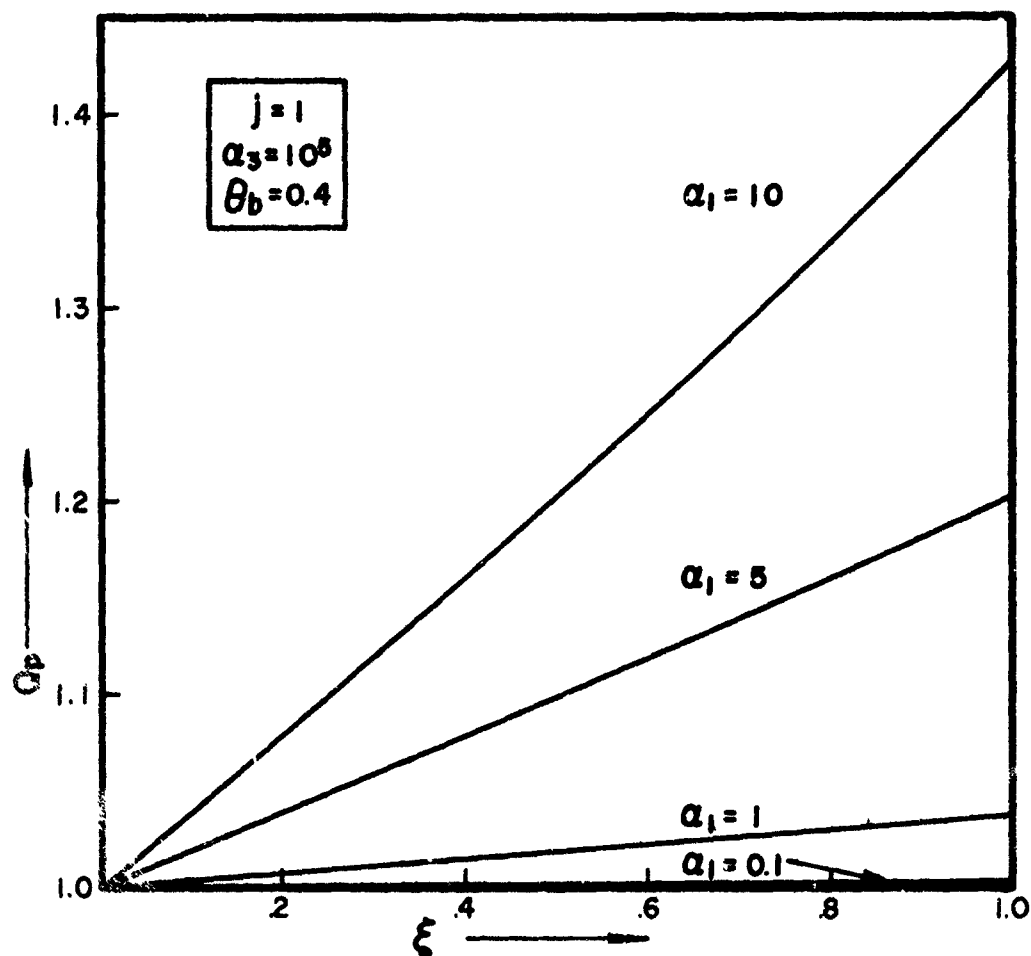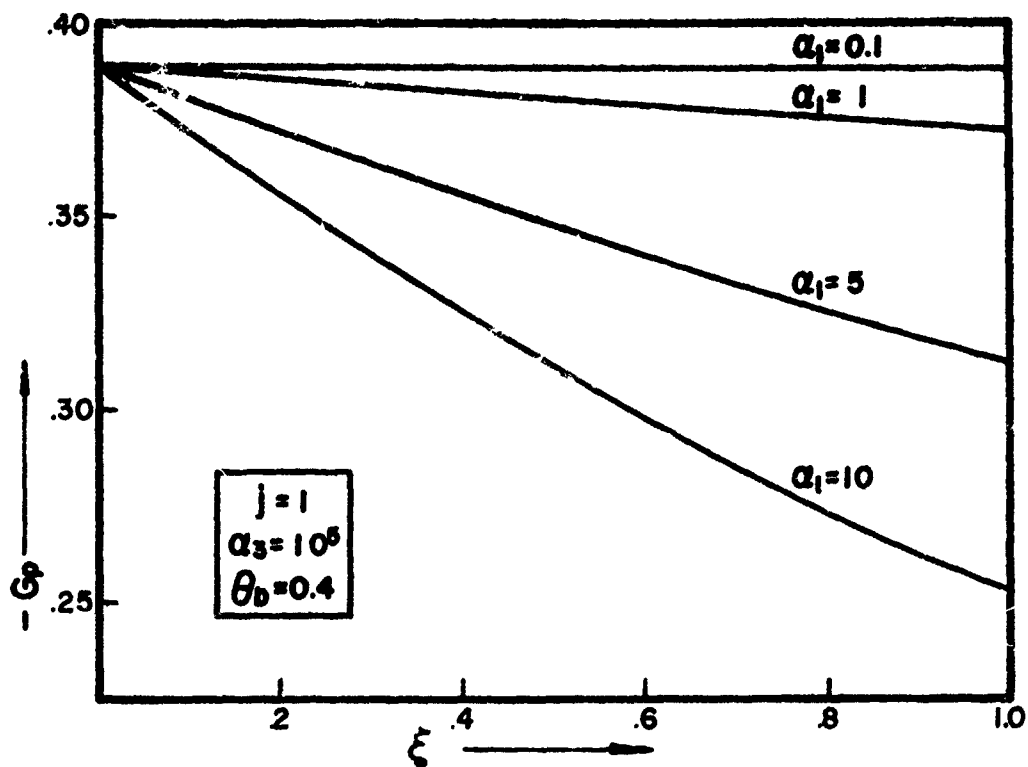
FIGURE 2.22. SURFACE DISTRIBUTIONS OF DROP-PHASE NORMAL VELOCITY
AND DROP-PHASE DENSITY

$\alpha_1 = 0.1$

$\alpha_1 = 1$

$\alpha_1 = 5$

$\alpha_1 = 10$

$j = 1$
$\alpha_3 = 10^9$
$\theta_b = 0.4$

$-G_P$

.40

.35

.30

.25

ξ

.2 .4 .6 .8 1.0

$j = 1$
$\alpha_3 = 10^9$
$\theta_b = 0.4$

$\alpha_1 = 10$

$\alpha_1 = 5$

$\alpha_1 = 1$

$\alpha_1 = 0.1$

Q_P

1.4

1.3

1.2

1.1

1.0

ξ

.2 .4 .6 .8 1.0
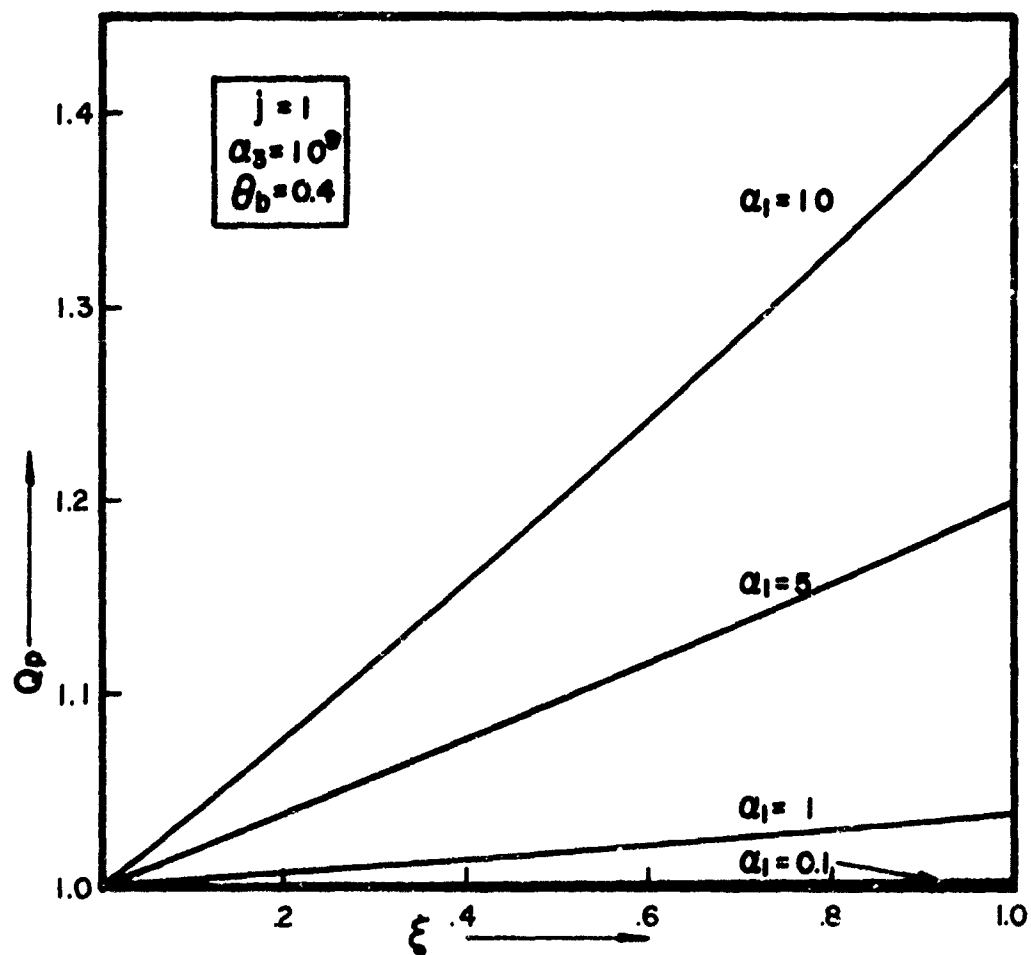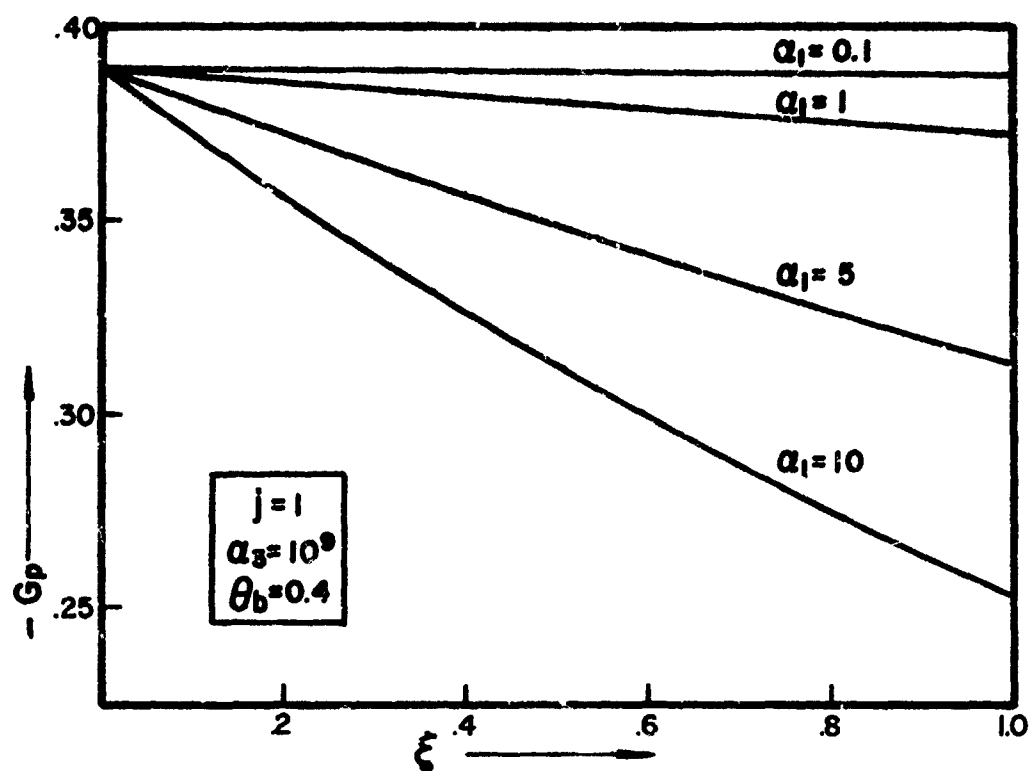
FIGURE 2.23. SURFACE DISTRIBUTIONS OF DROP-PHASE NORMAL VELOCITY
AND DROP-PHASE DENSITY
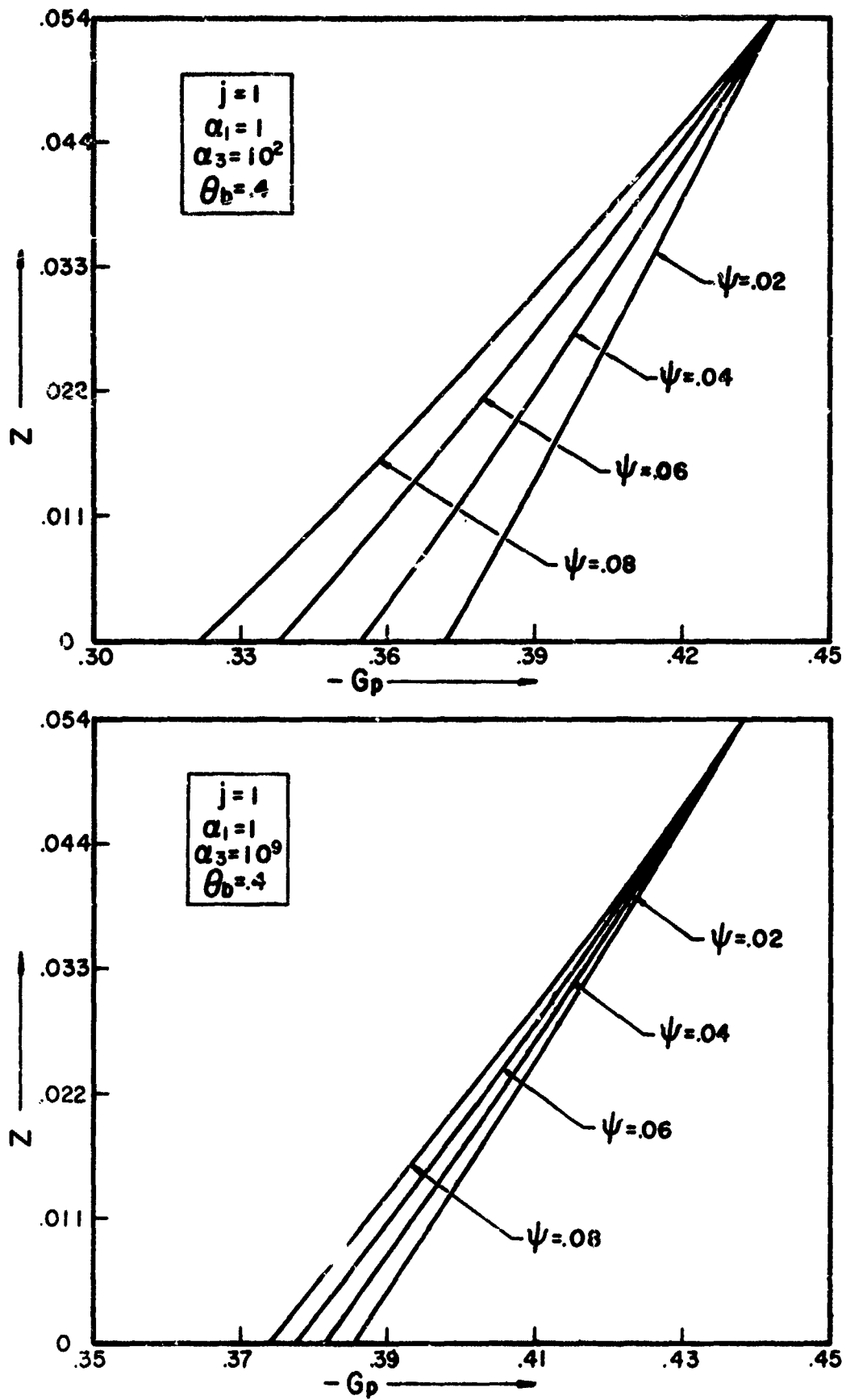
FIGURE 2.24.   DROP-PHASE TRANSVERSE-VELOCITY VARIATIONS ALONG
SELECTED STREAMLINES
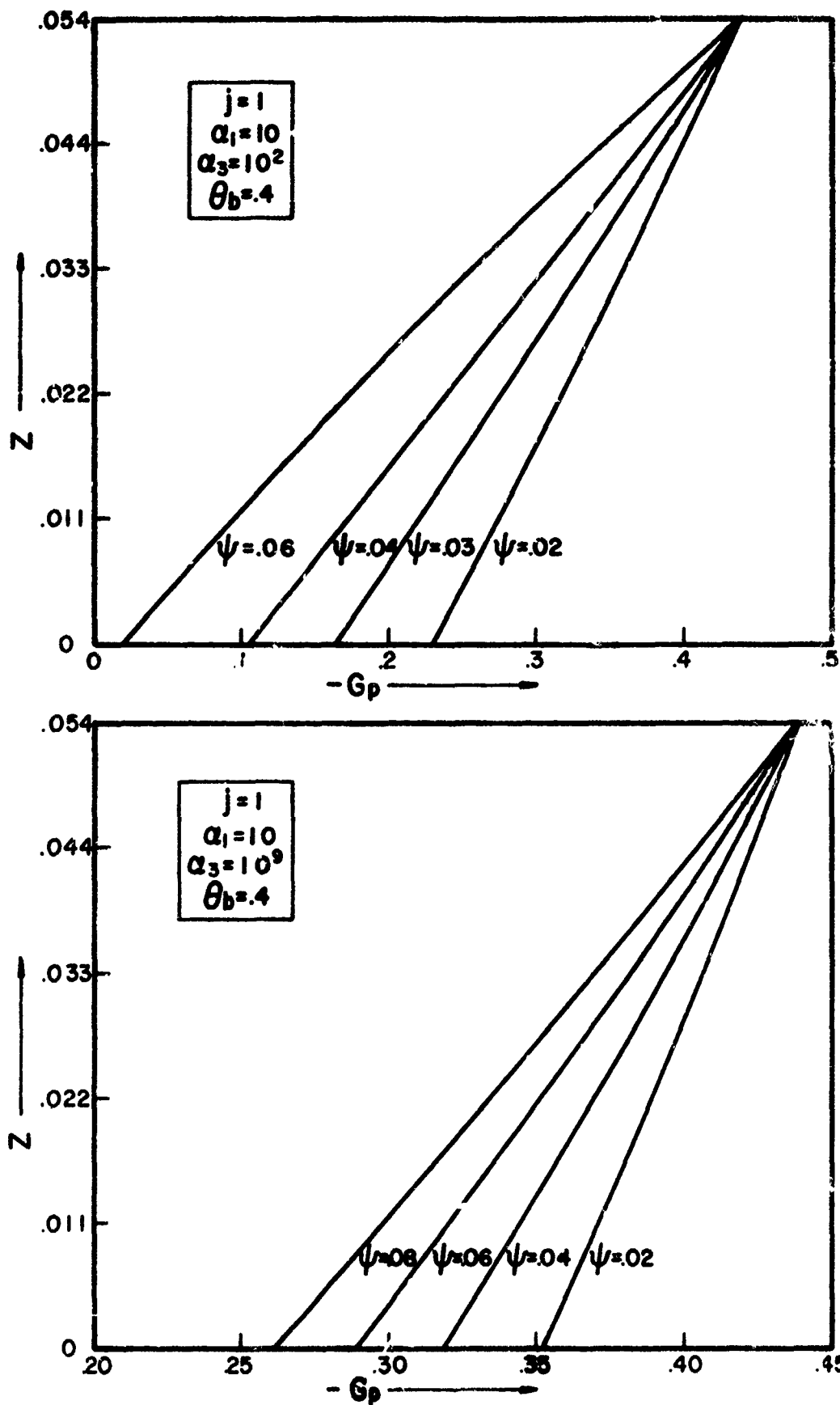
FIGURE 2.25.   DROP-PHASE TRANSVERSE-VELOCITY VARIATIONS ALONG
              SELECTED STREAMLINES
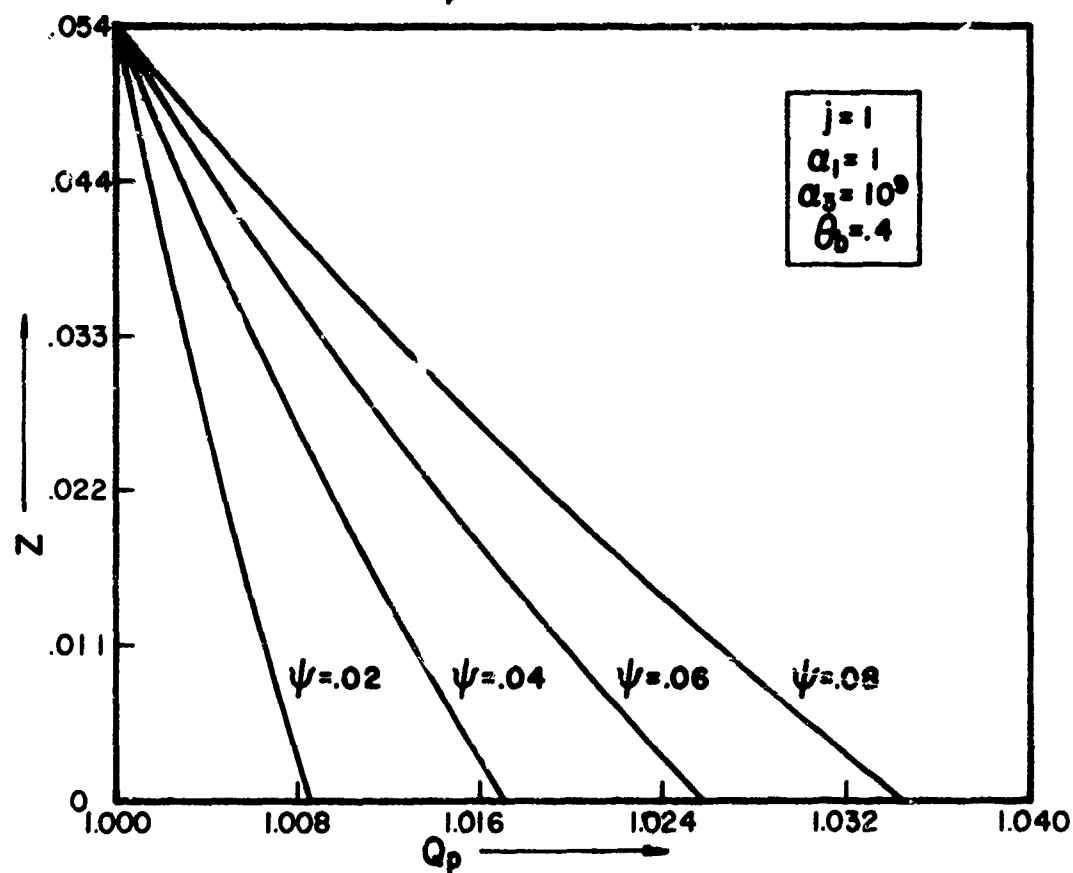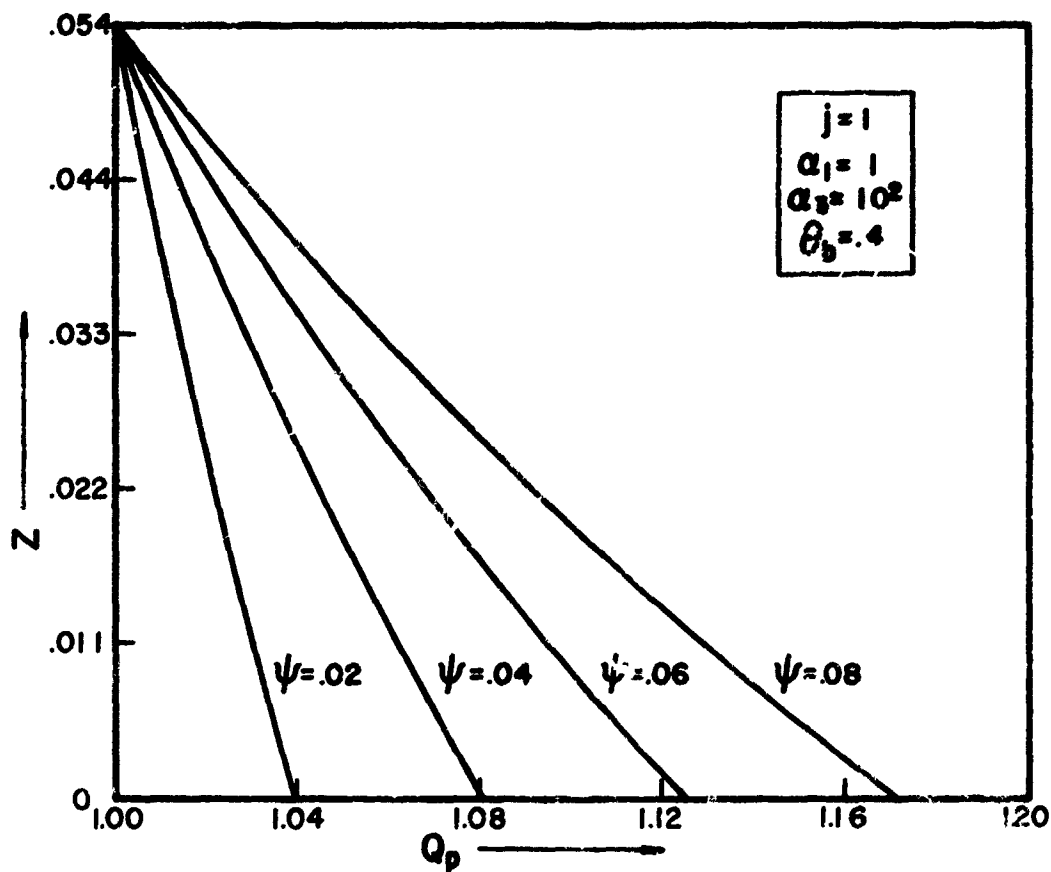
FIGURE 2.26. DROP-PHASE DENSITY VARIATIONS ALONG SELECTED STREAMLINES
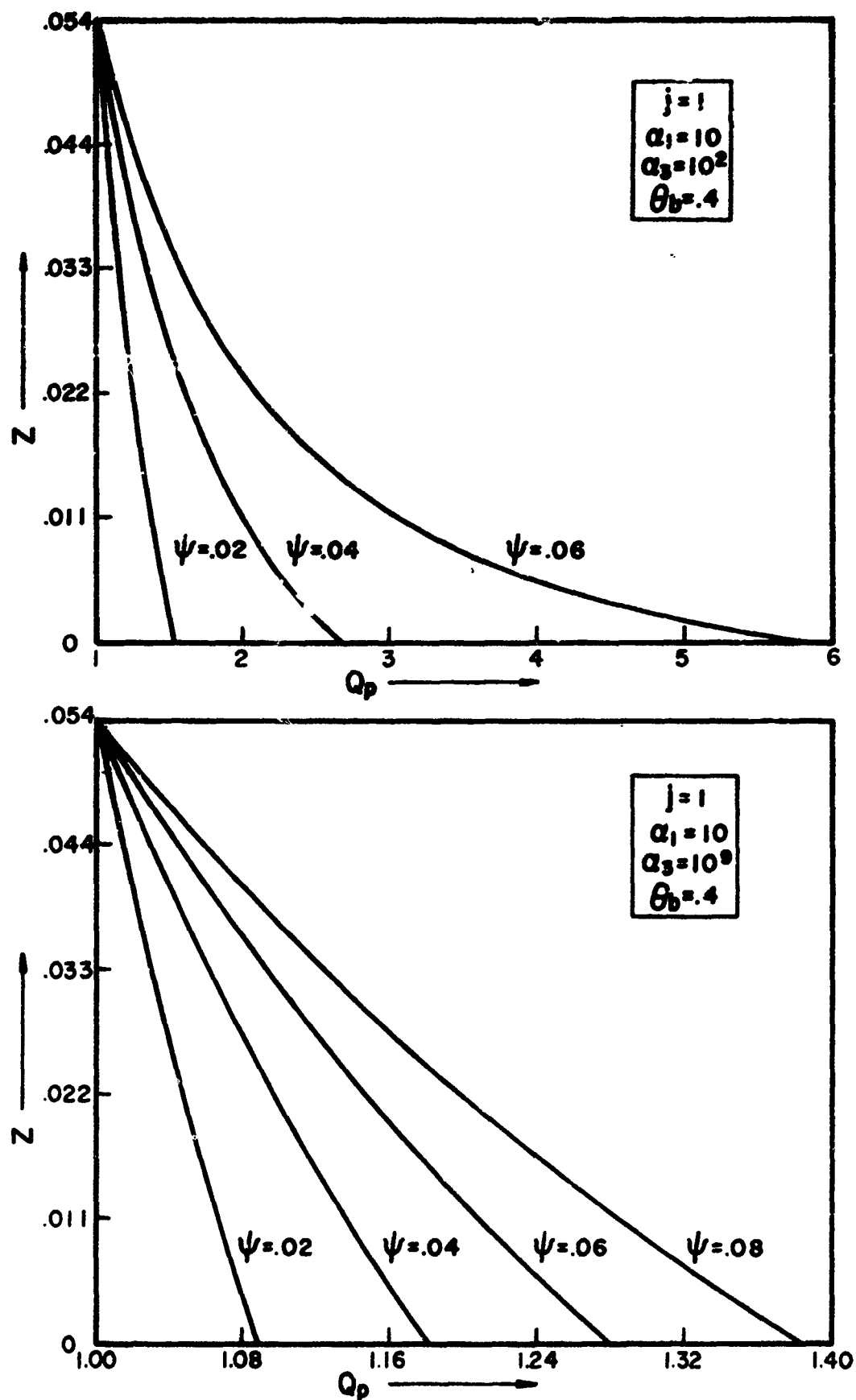
FIGURE 2.27.   DROP-PHASE DENSITY VARIATIONS ALONG SELECTED STREAMLINES
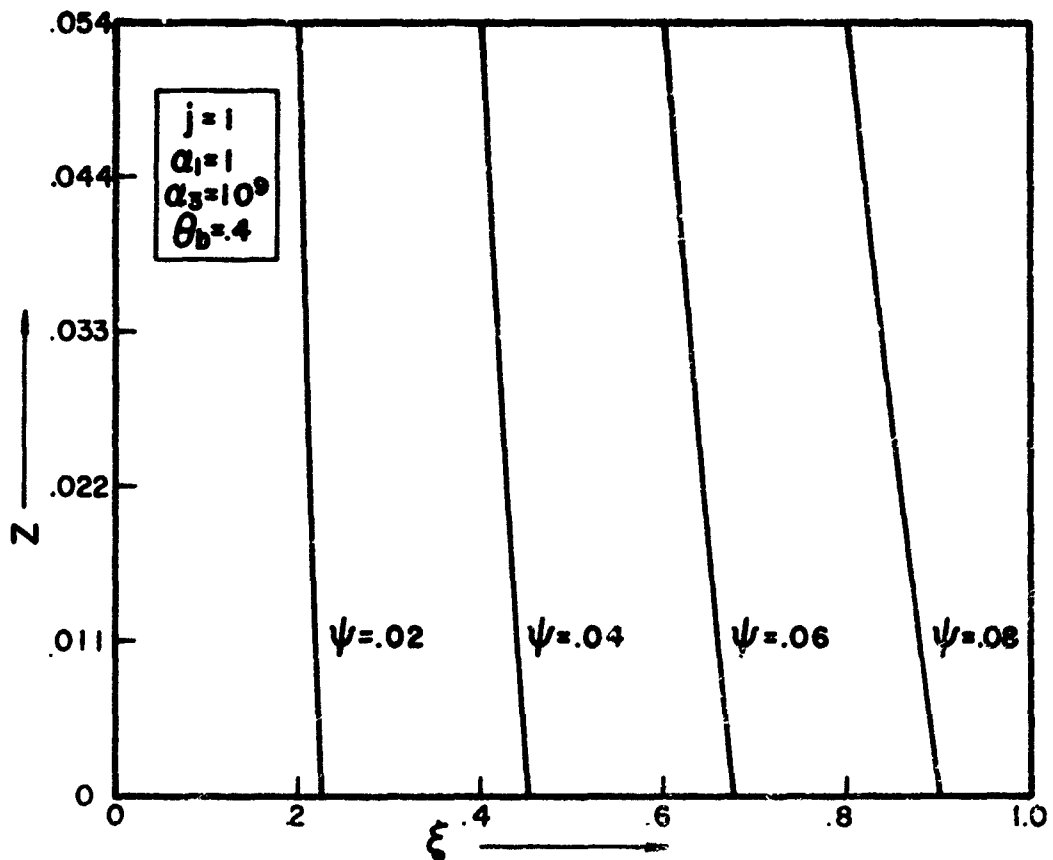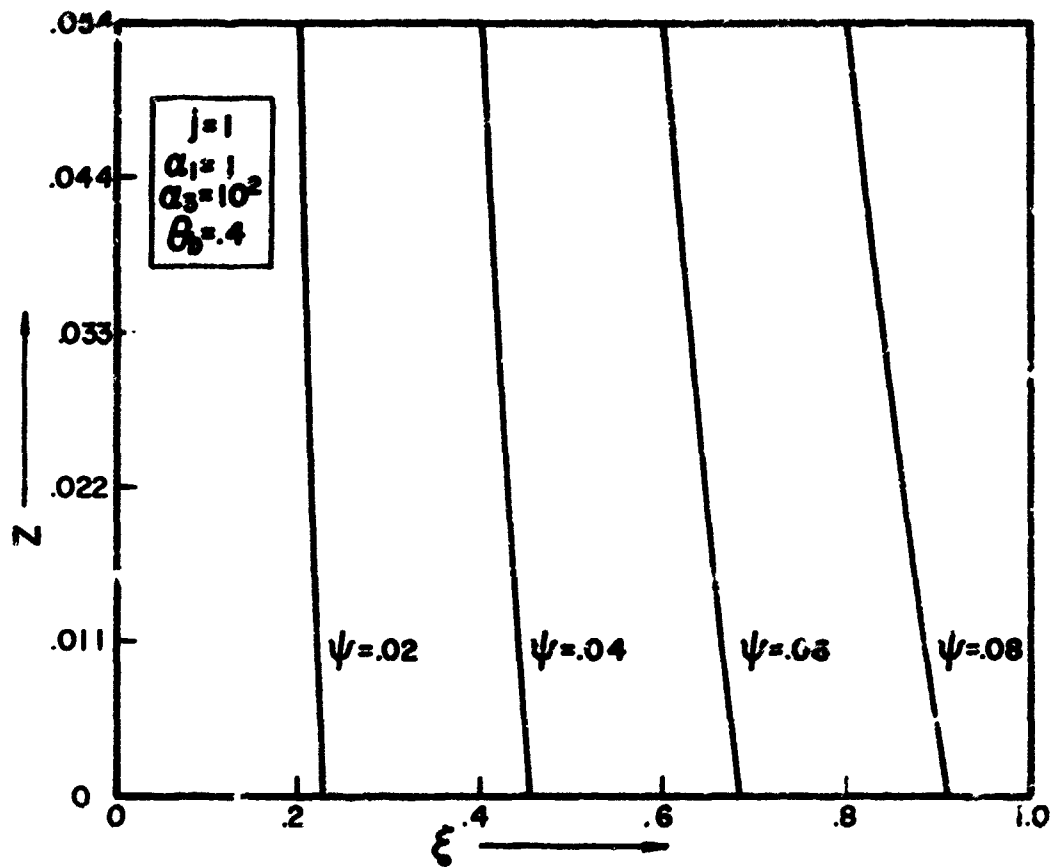
FIGURE 2.28. SELECTED DROP-PHASE STREAMLINES
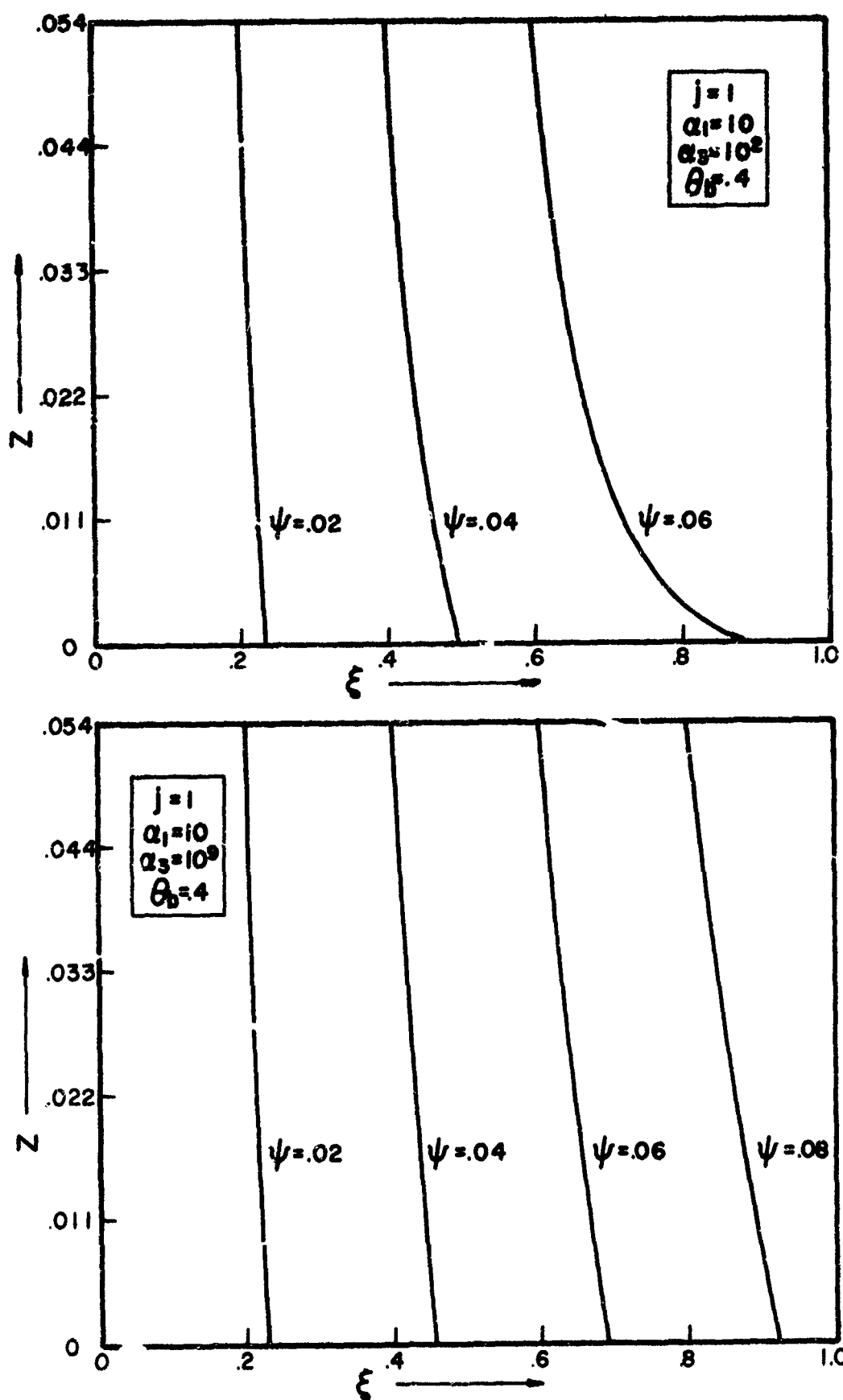
FIGURE 2.29. SELECTED DROP-PHASE STREAMLINES
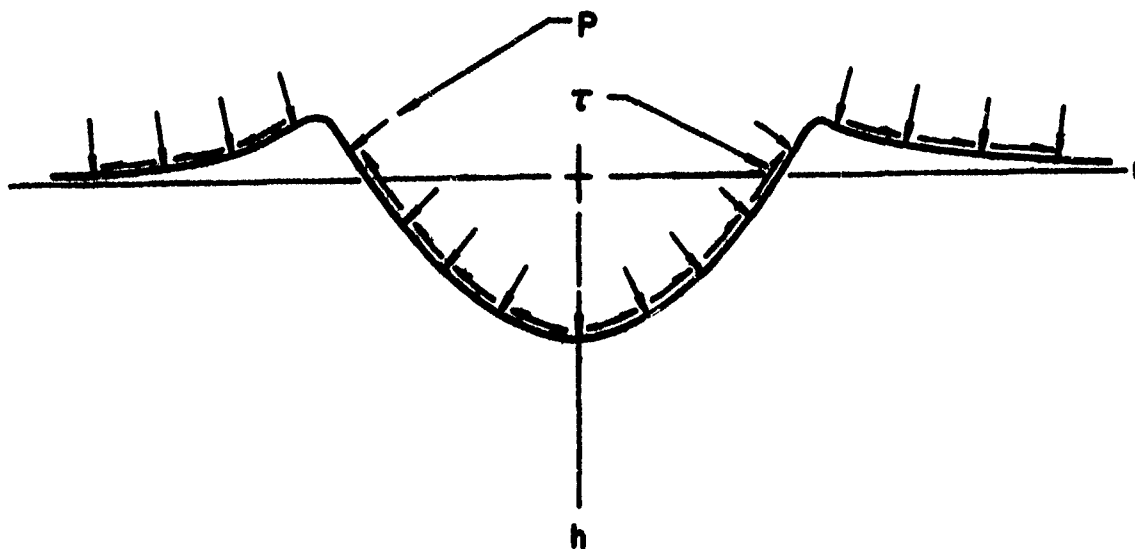
FIGURE 3.1. CAVITY CONFIGURATION
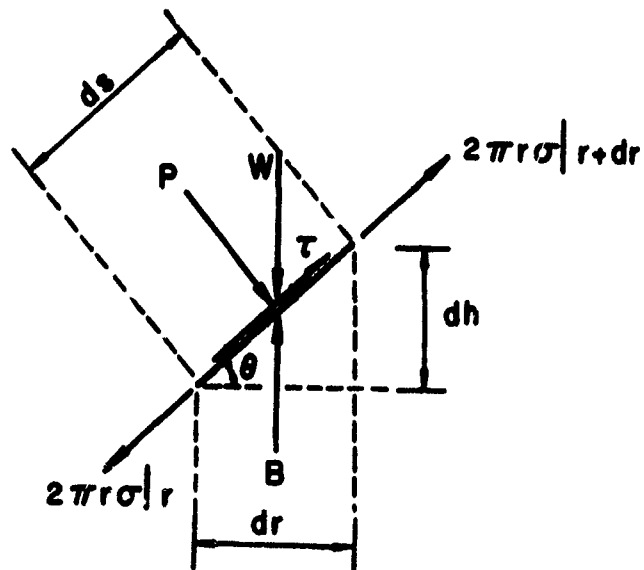
FIGURE 3.2. FORCE BALANCE ON AN INFINITESIMAL ELEMENT
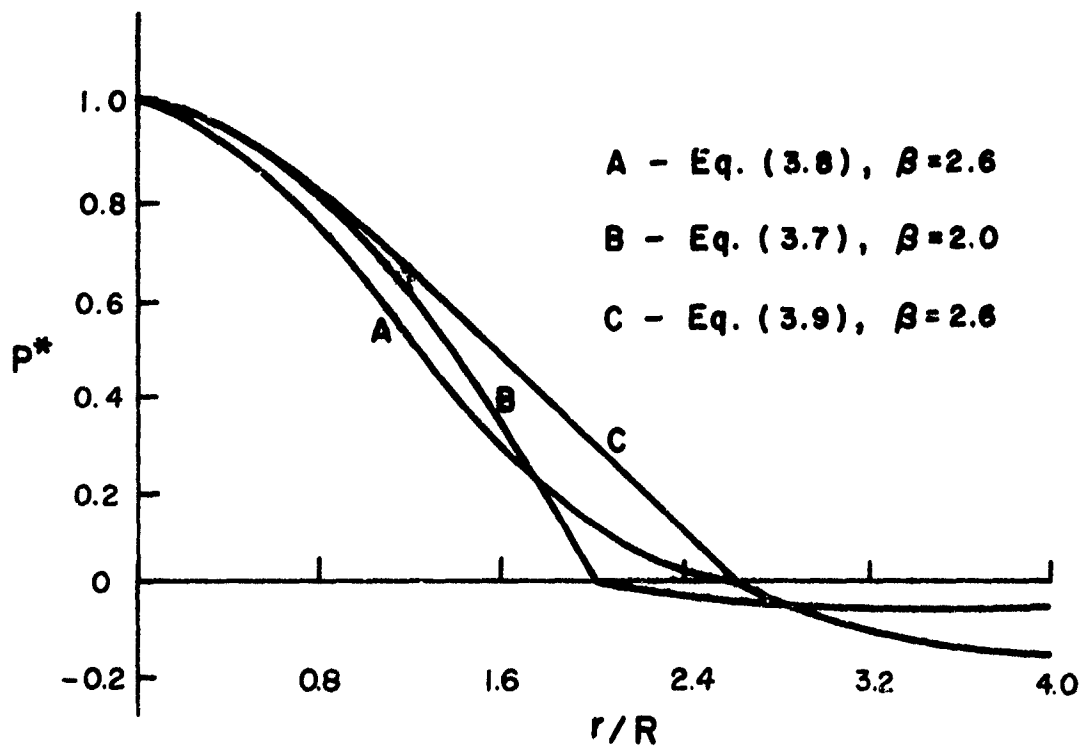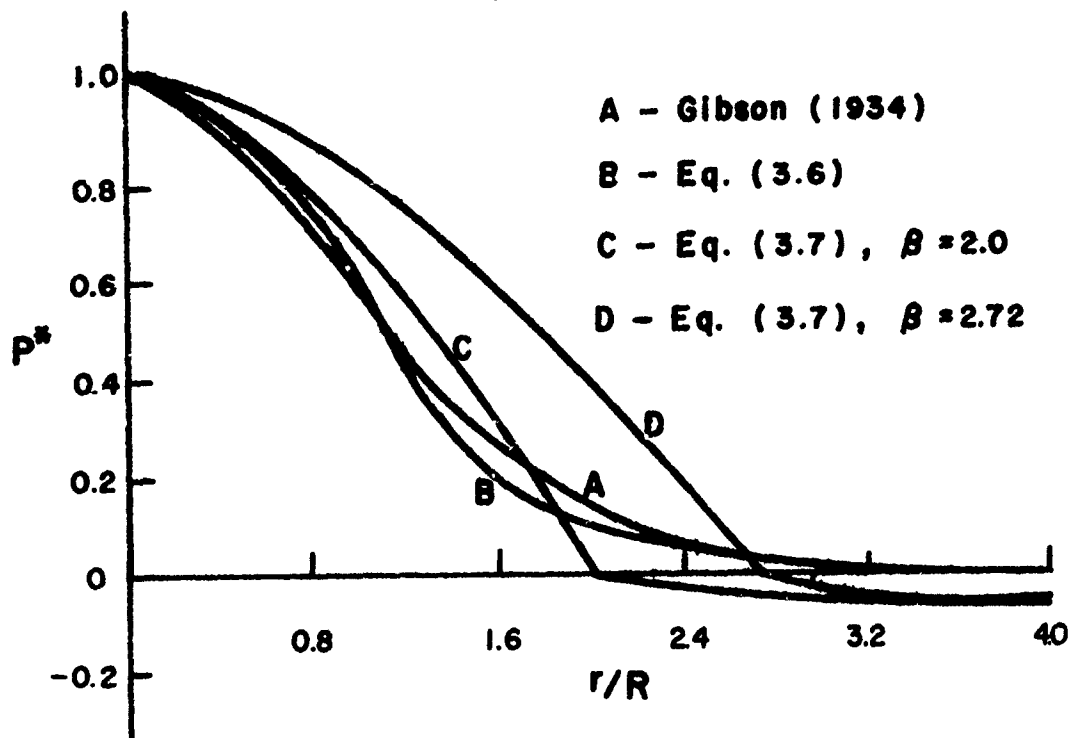
FIGURE 3.3. PRESSURE DISTRIBUTIONS
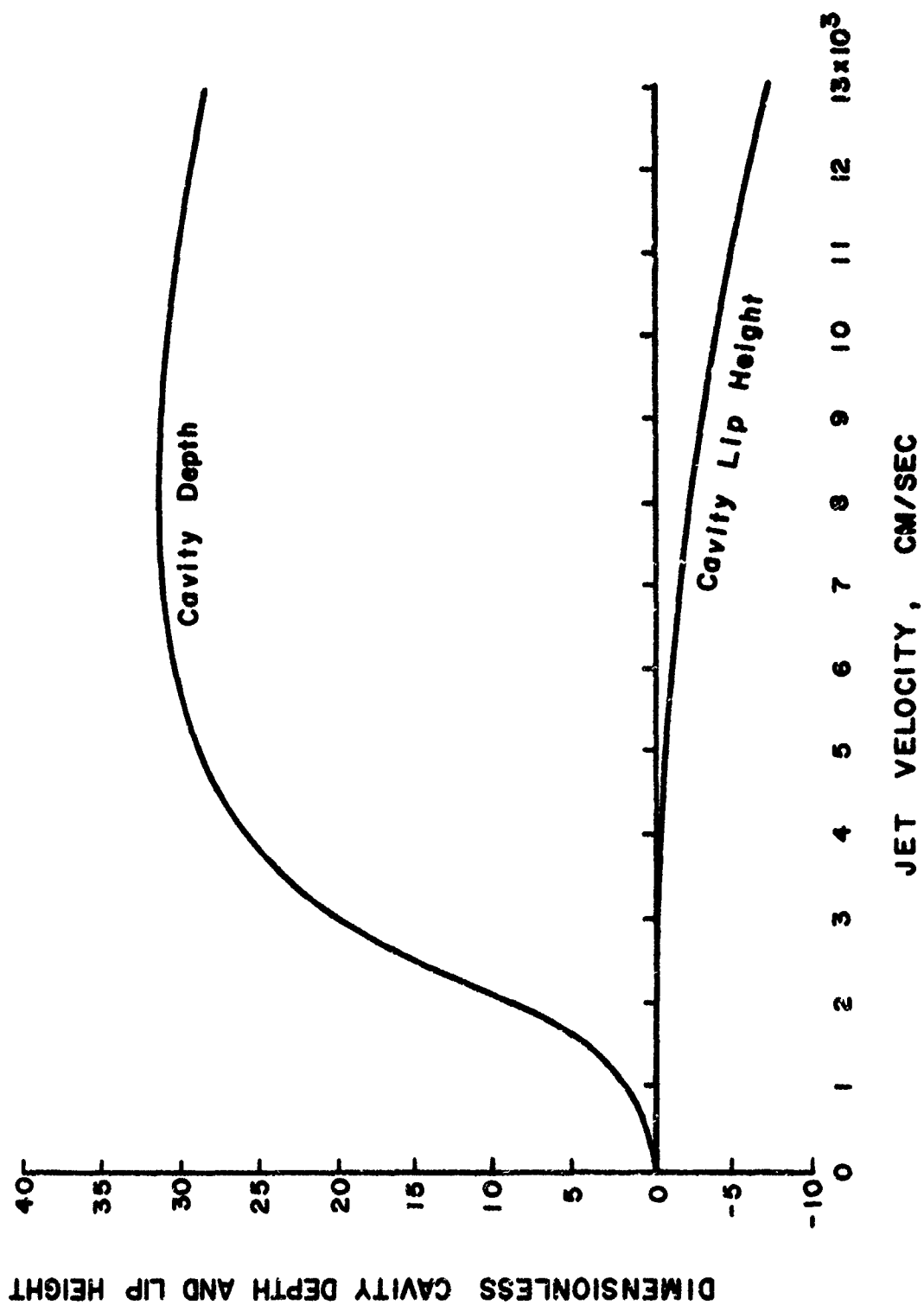
FIGURE 3.4. VELOCITY EFFECT

JET VELOCITY, CM/SEC

DIMENSIONLESS CAVITY DEPTH AND LIP HEIGHT

Cavity Depth

Cavity Lip Height
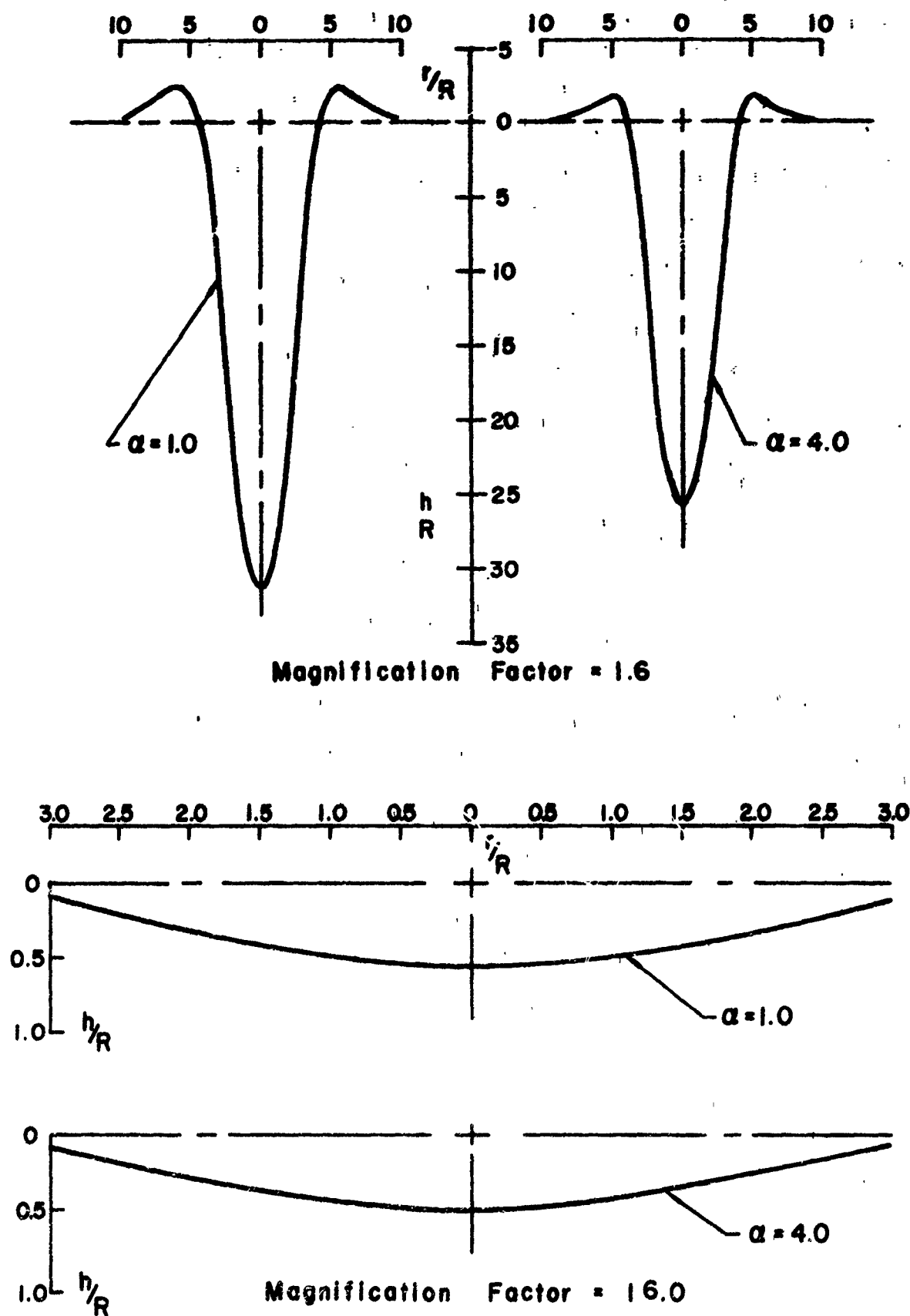
FIGURE 3.5. SHEAR FACTOR EFFECTS IN STRONG PENETRATION (V=8000 CM/SEC)
AND WEAK PENETRATION (V=600 CM/SEC)
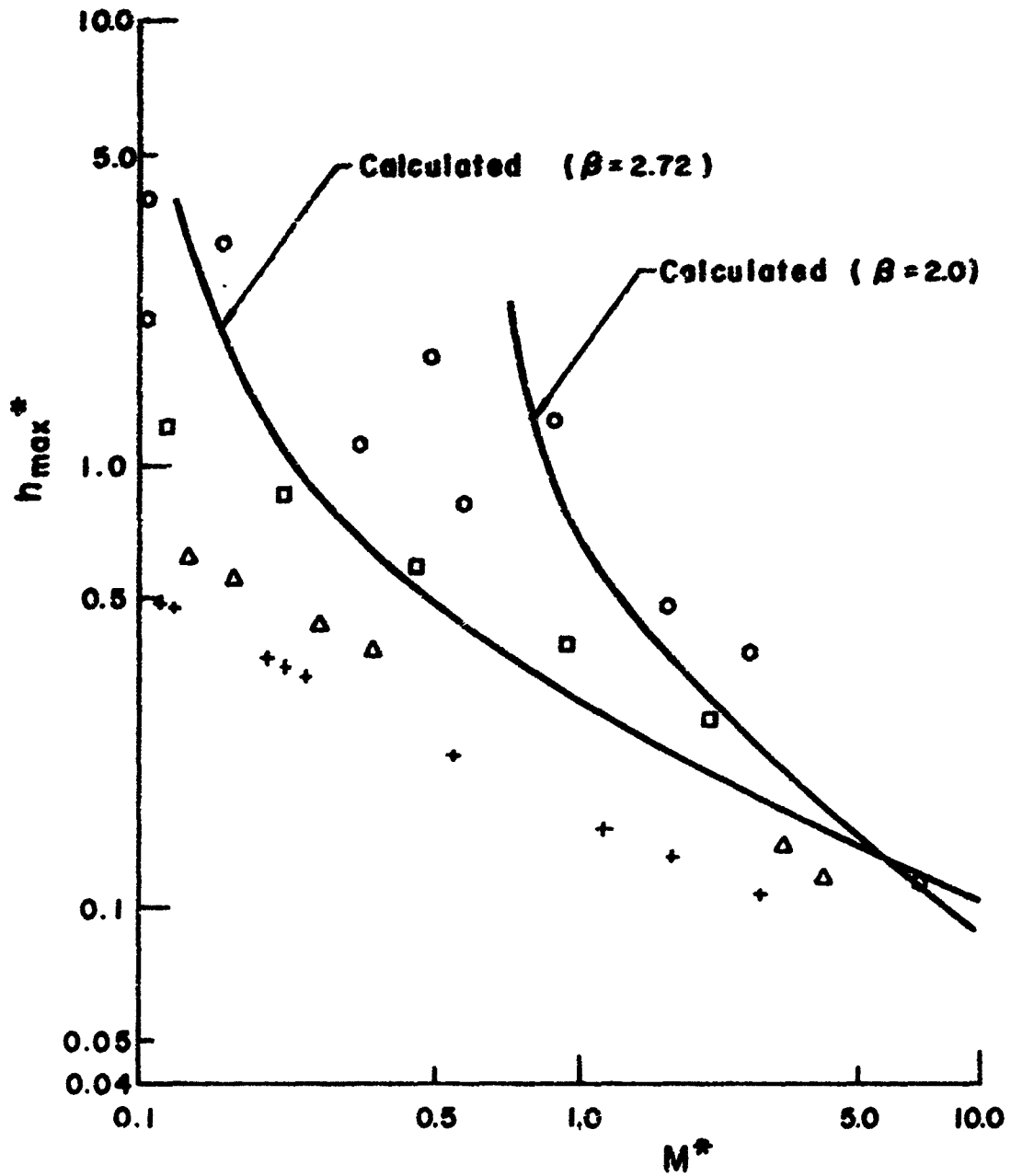
FIGURE 3.6.   IMPACT OF OIL JET ON WATER SURFACE
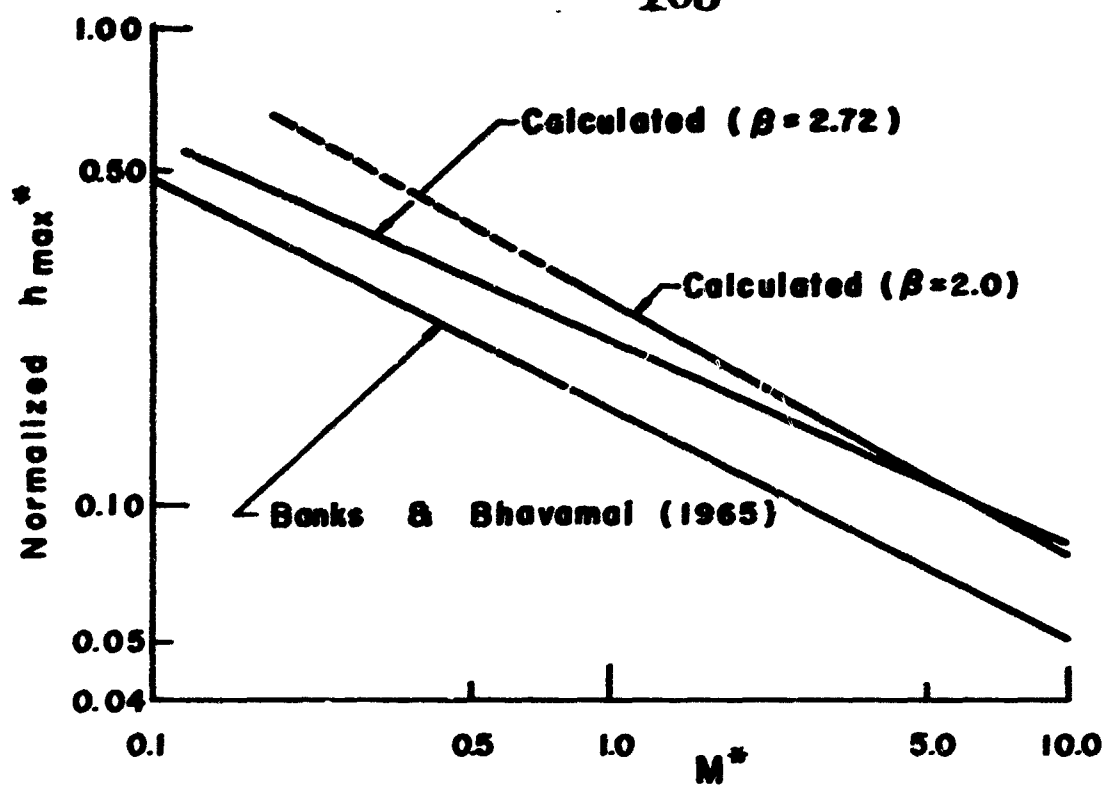
FIGURE 3.7.   IMPACT OF OIL JET ON WATER SURFACE
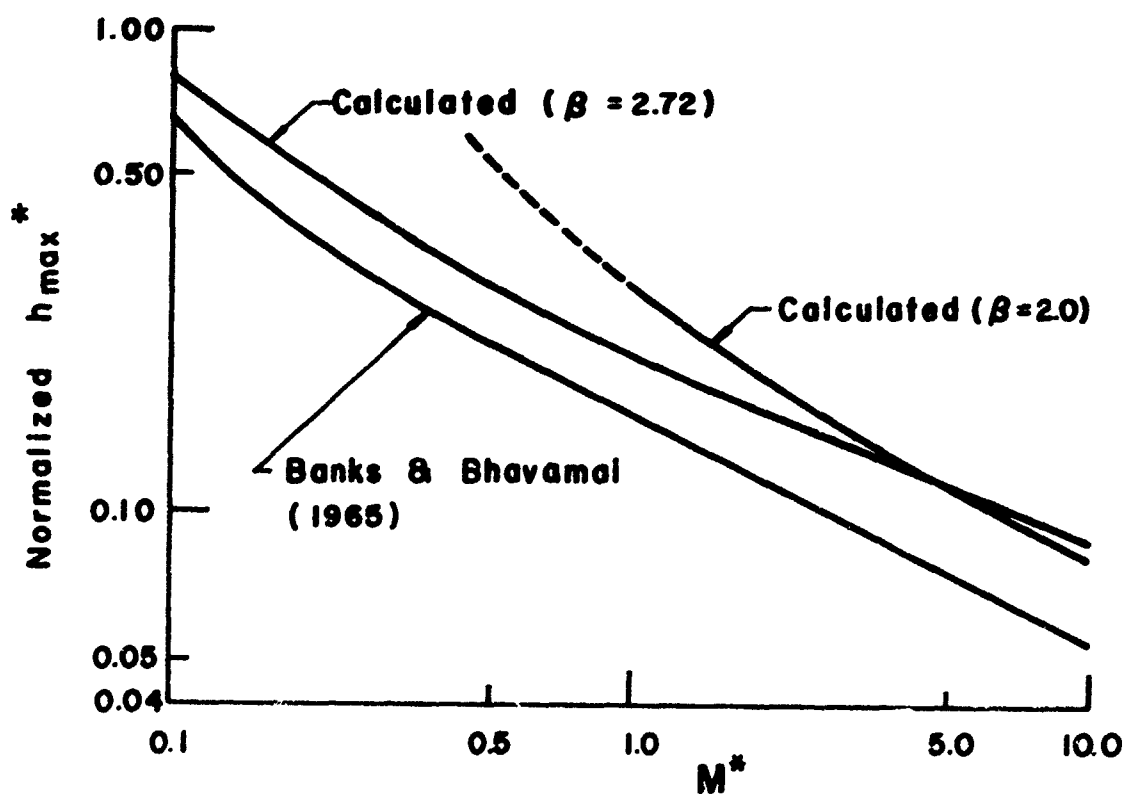
FIGURE 3.8.   IMPACT OF WATER JET ON CARBON TETRACHLORIDE SURFACE
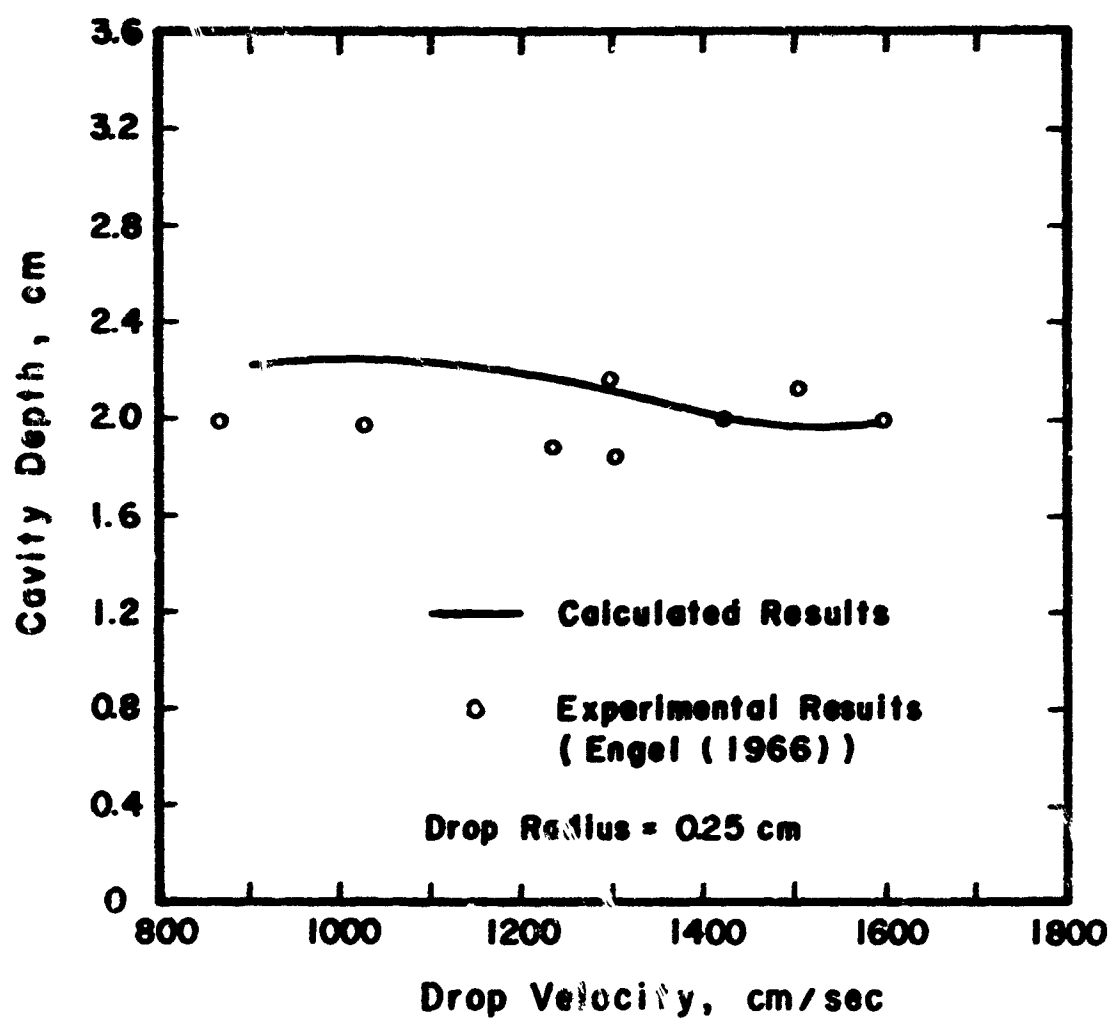
FIGURE 3.9.   MAXIMUM CAVITY DEPTH PRODUCED B' IMPACT OF A WATER DROP
AGAINST WATER
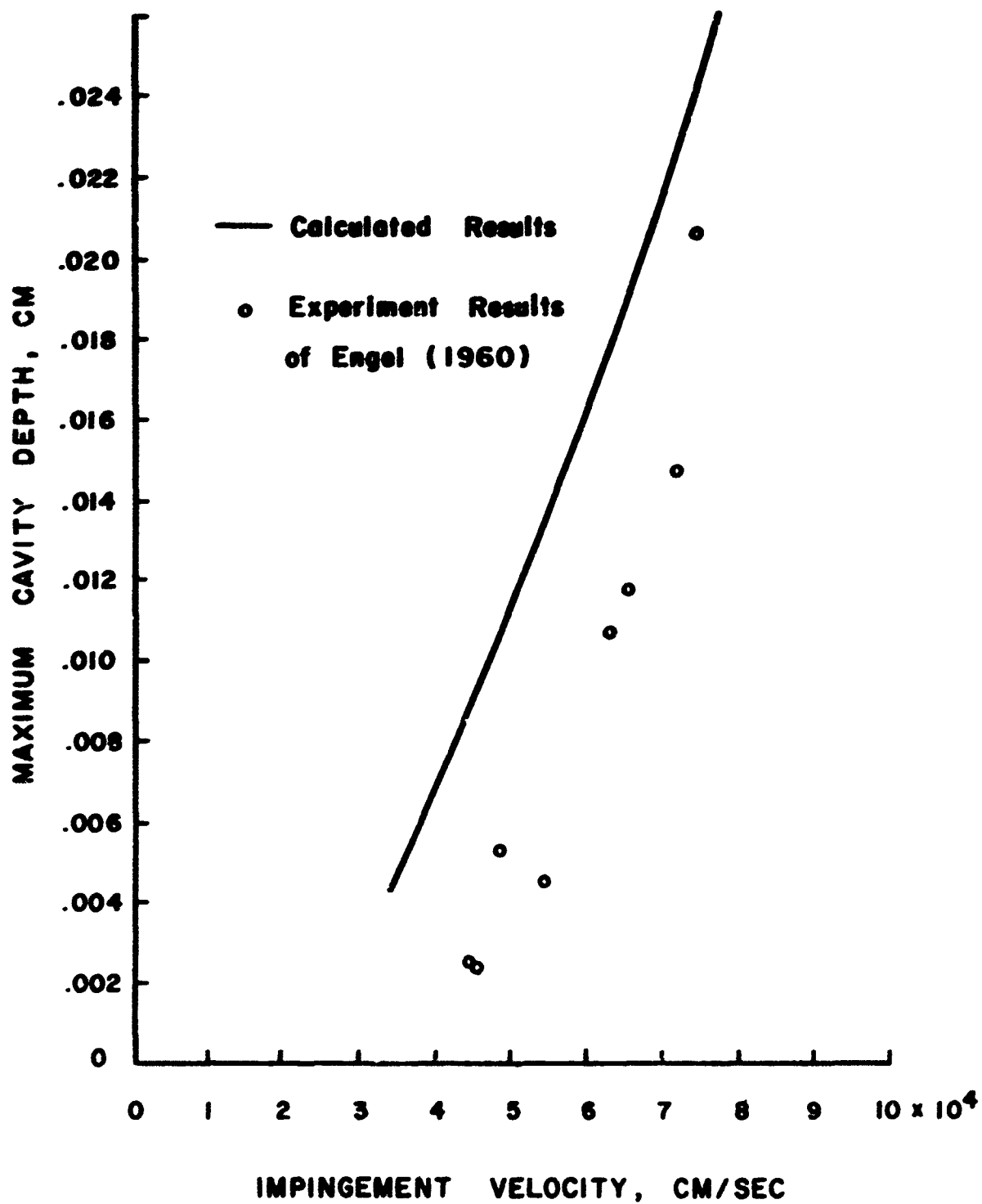
FIGURE 3.10.   IMPACT OF WATER DROPS ON 2024-0 ALUMINUM
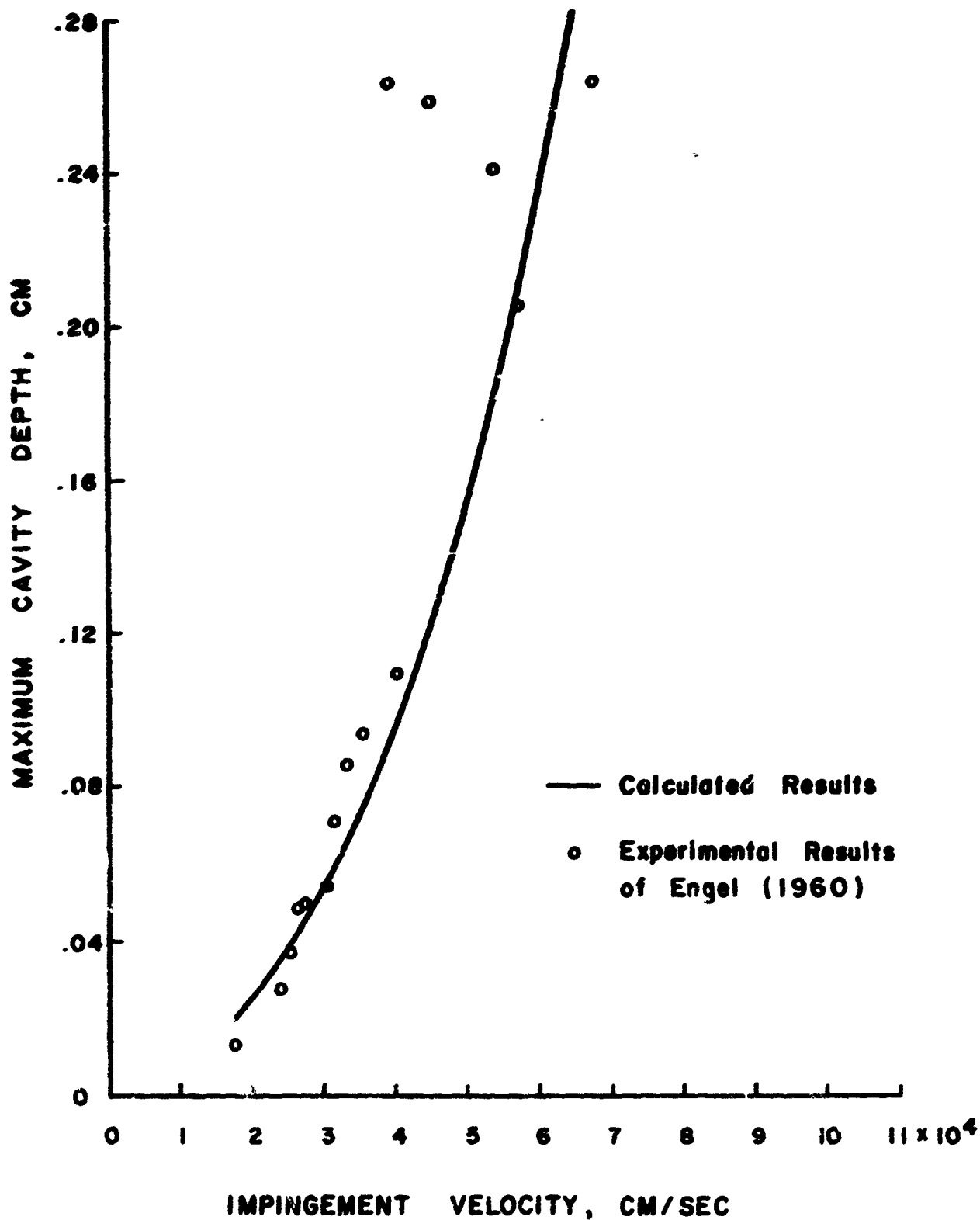
FIGURE 3.11. IMPACT OF MERCURY DROPS ON 2024-0 ALUMINUM
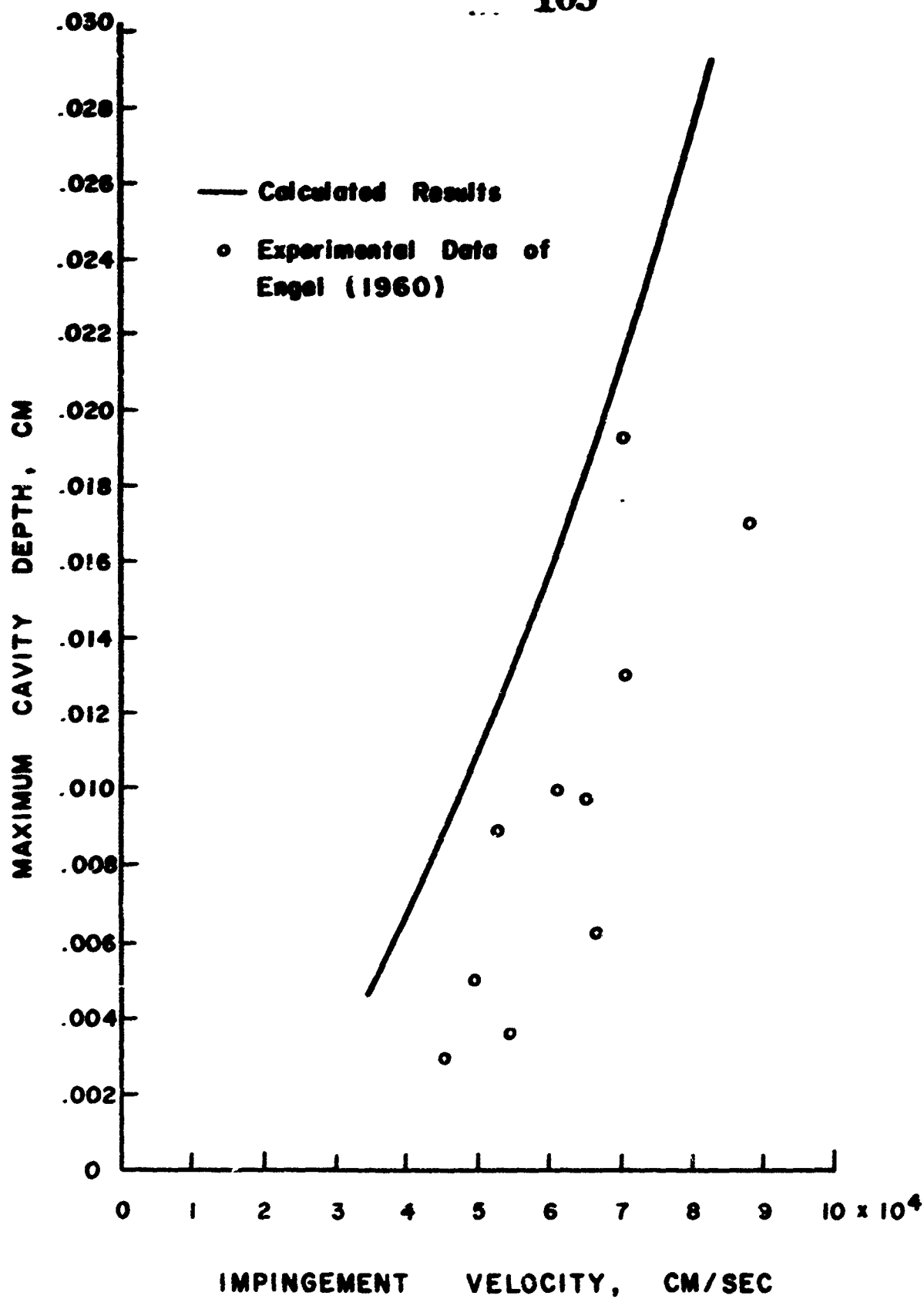
FIGURE 3.12. IMPACT OF WATER DROPS ON COPPER
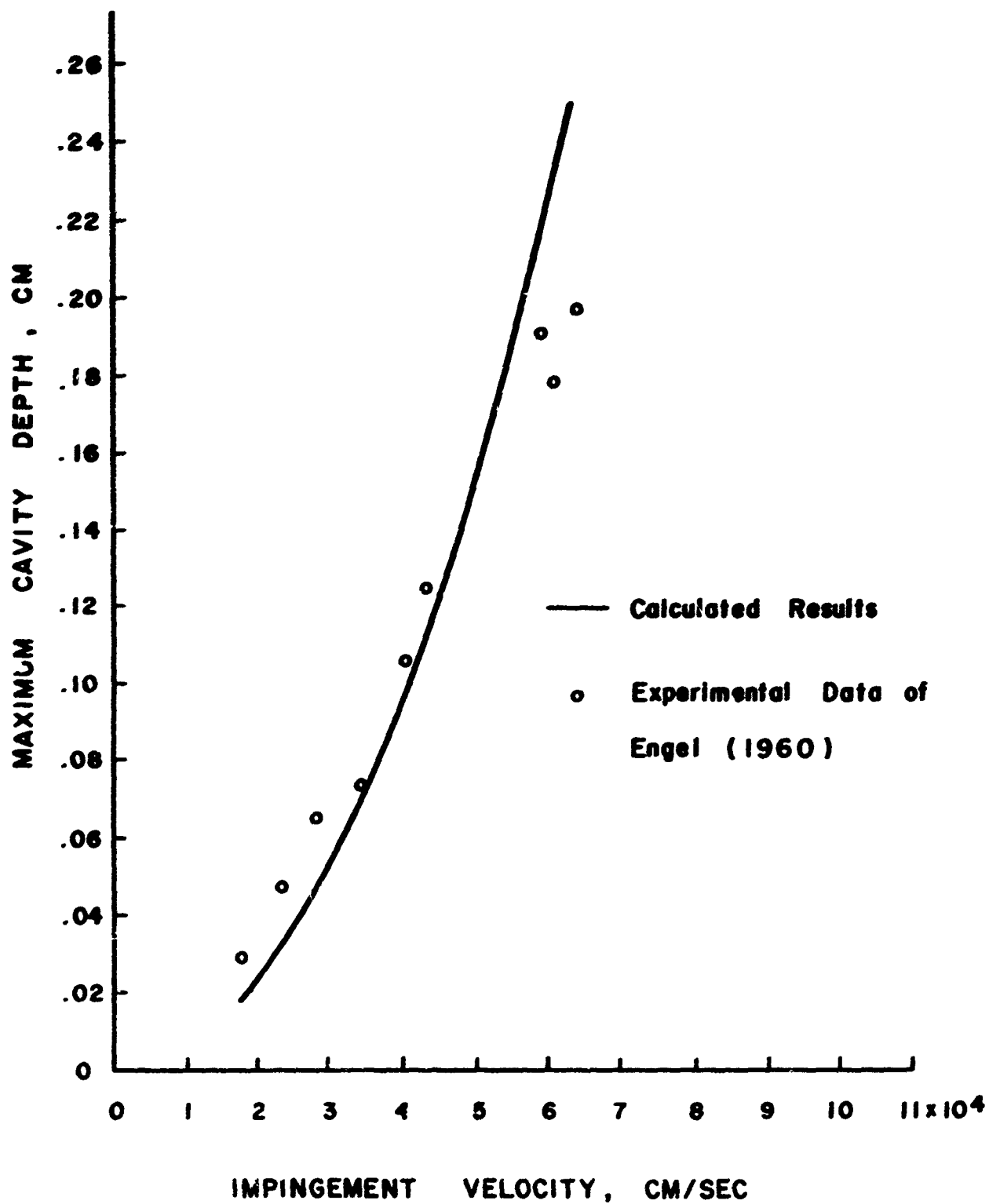
FIGURE 3.13. IMPACT OF MERCURY DROPS ON COPPER
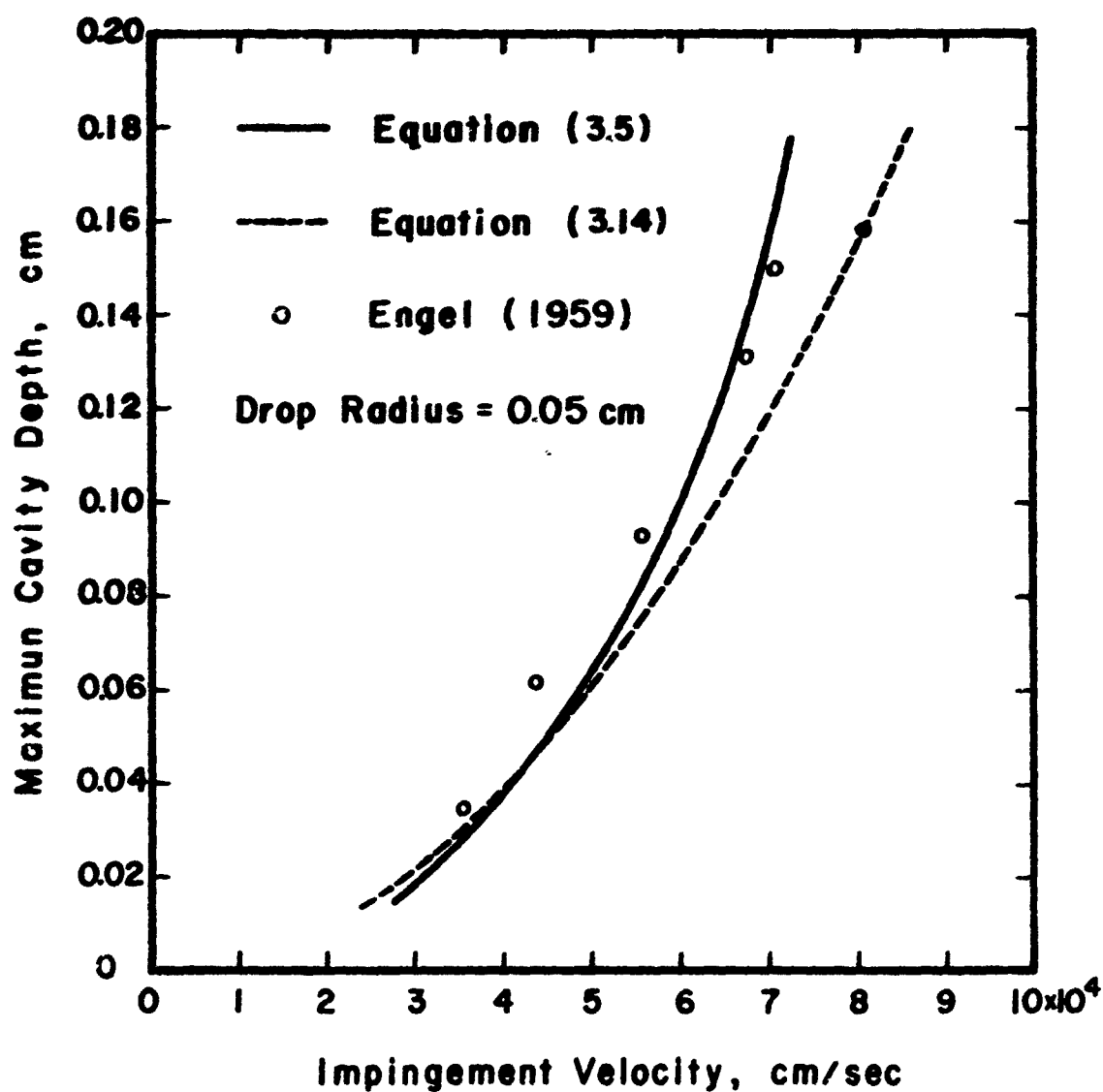
FIGURE 3.14. IMPACT OF MERCURY DROPS AGAINST 2024-0 ALUMINUM
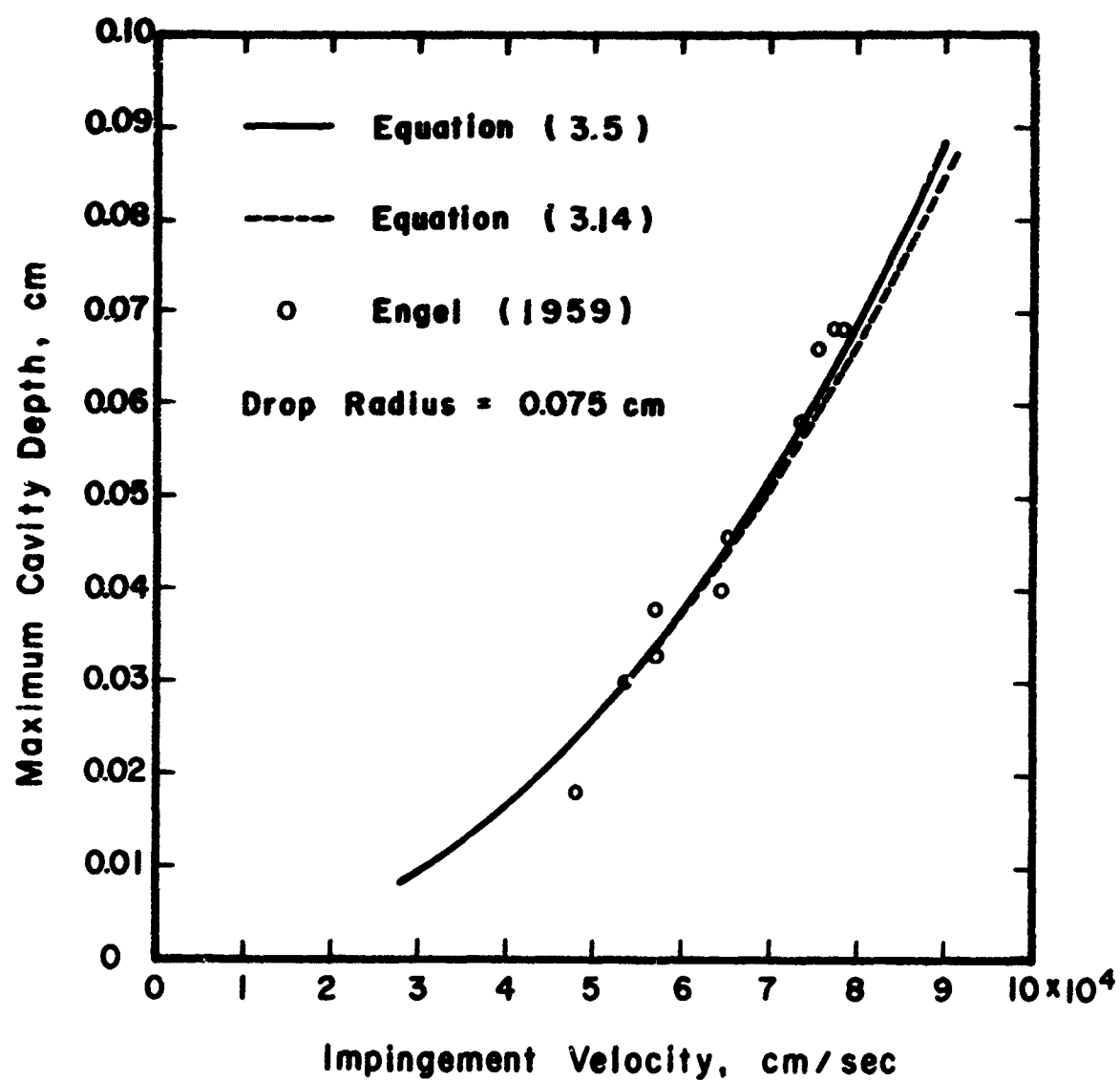
FIGURE 3.15.   IMPACT OF MERCURY DROPS AGAINST STEEL
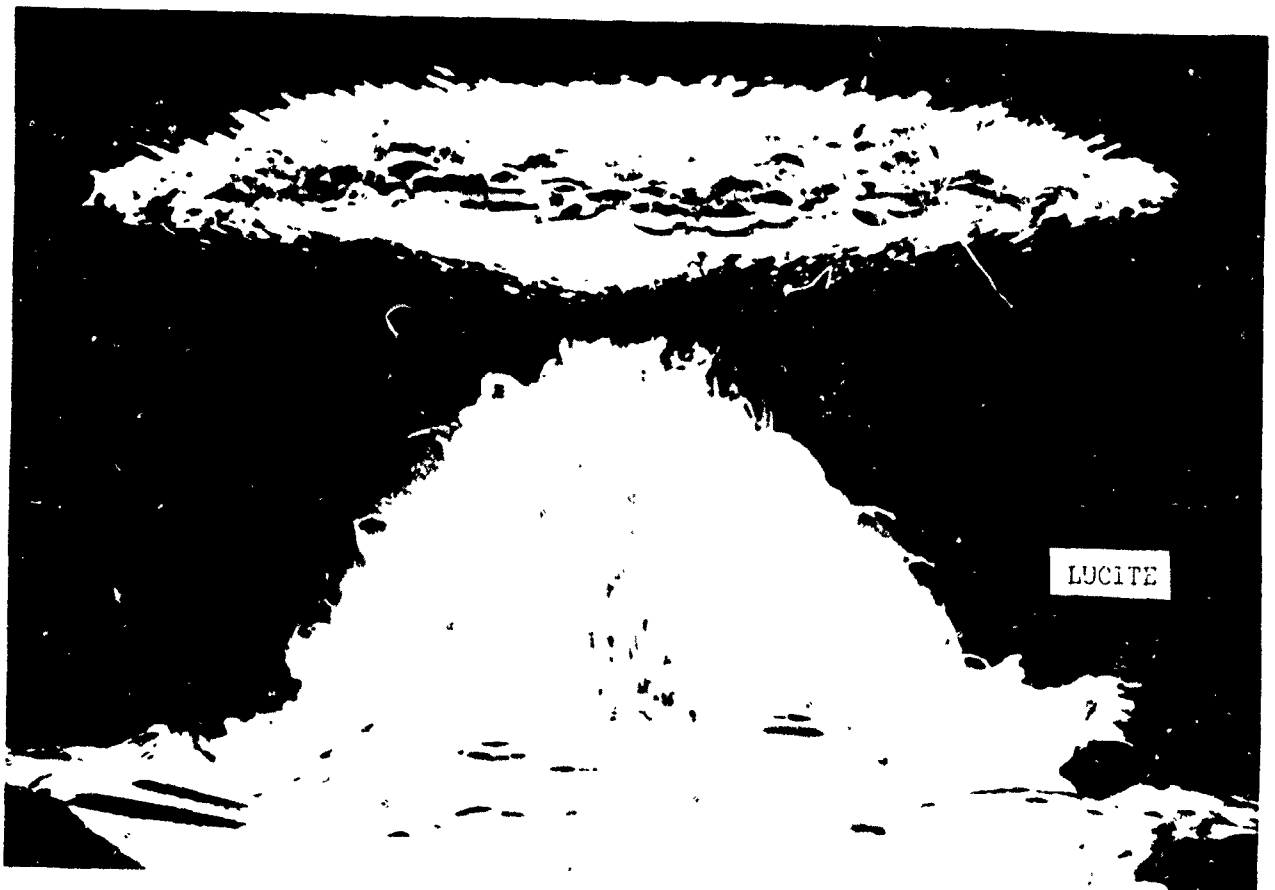
FIGURE 4.1   FRACTURES CAUSED BY REFLECTED STRESS WAVES
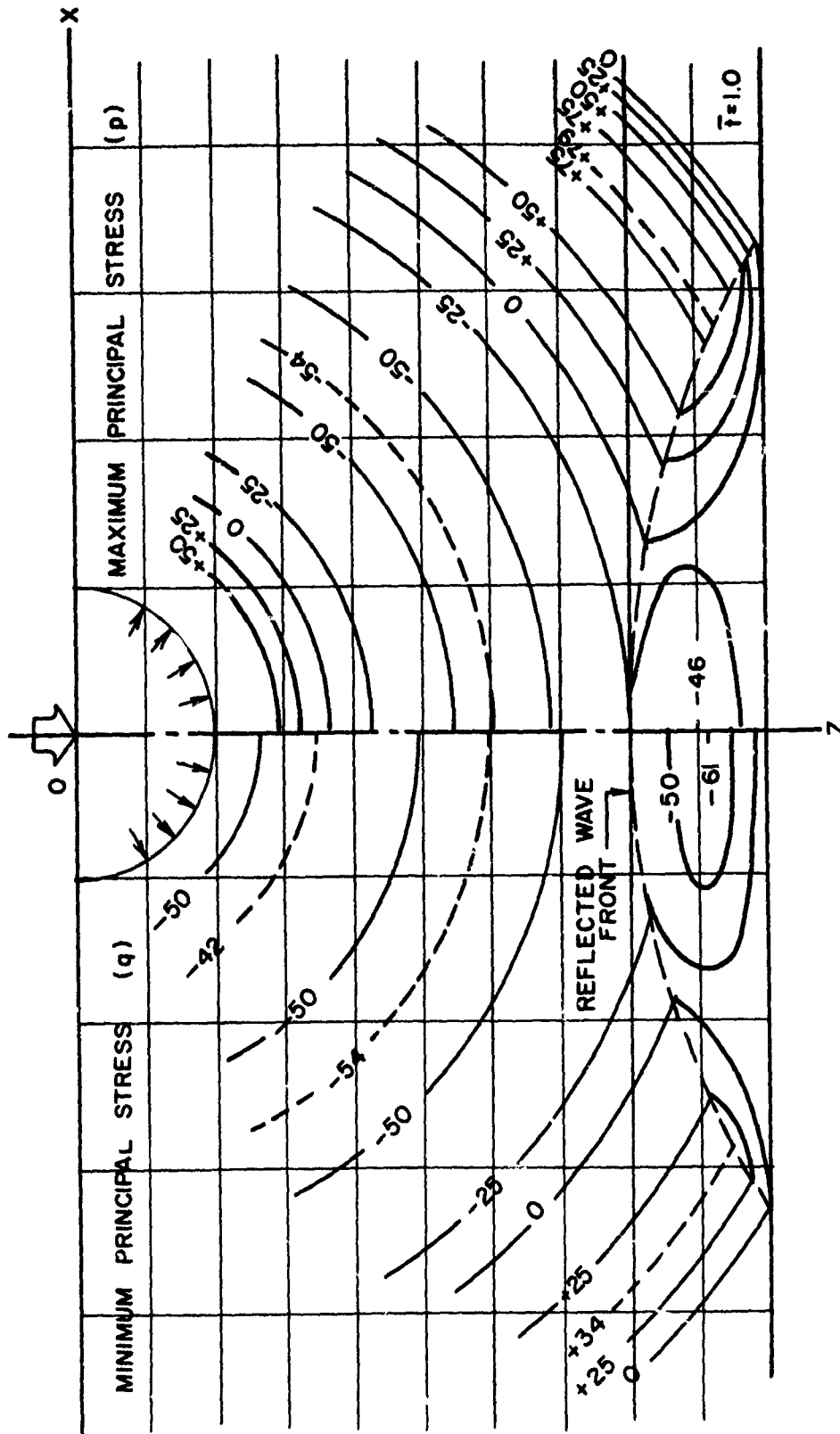
FIGURE 4.2 PRINCIPAL STRESSES PRODUCED BY IMPACT
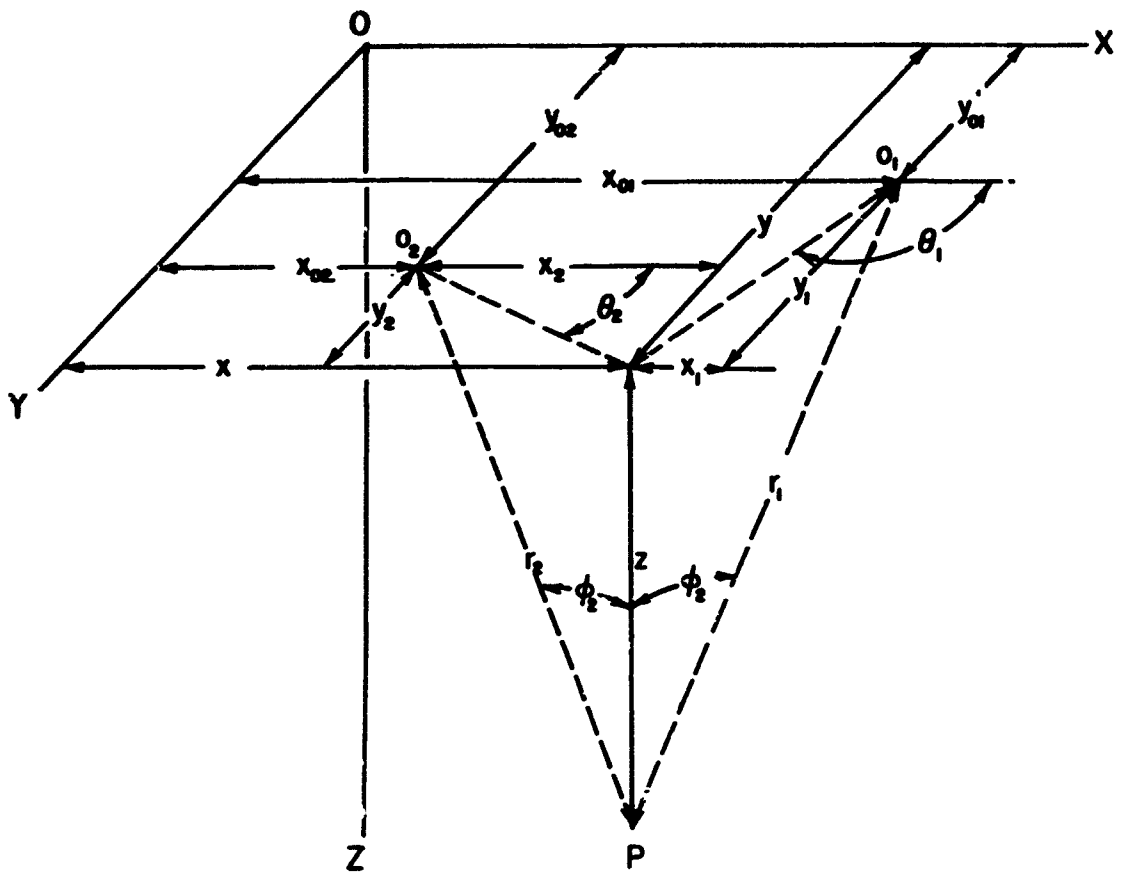
FIGURE 4.3 COORDINATE SYSTEM
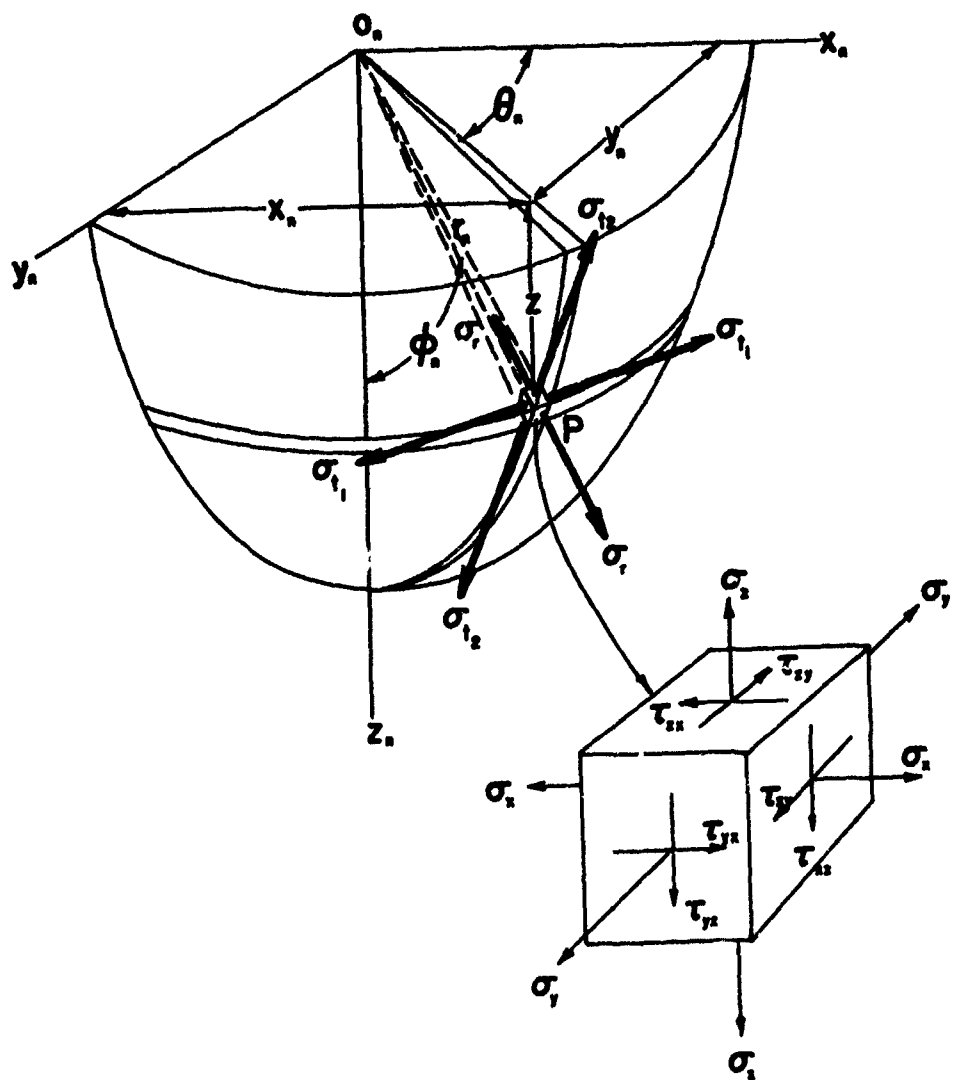
FIGURE 4.4 STRESSES CREATED BY SPHERICAL STRESS WAVES
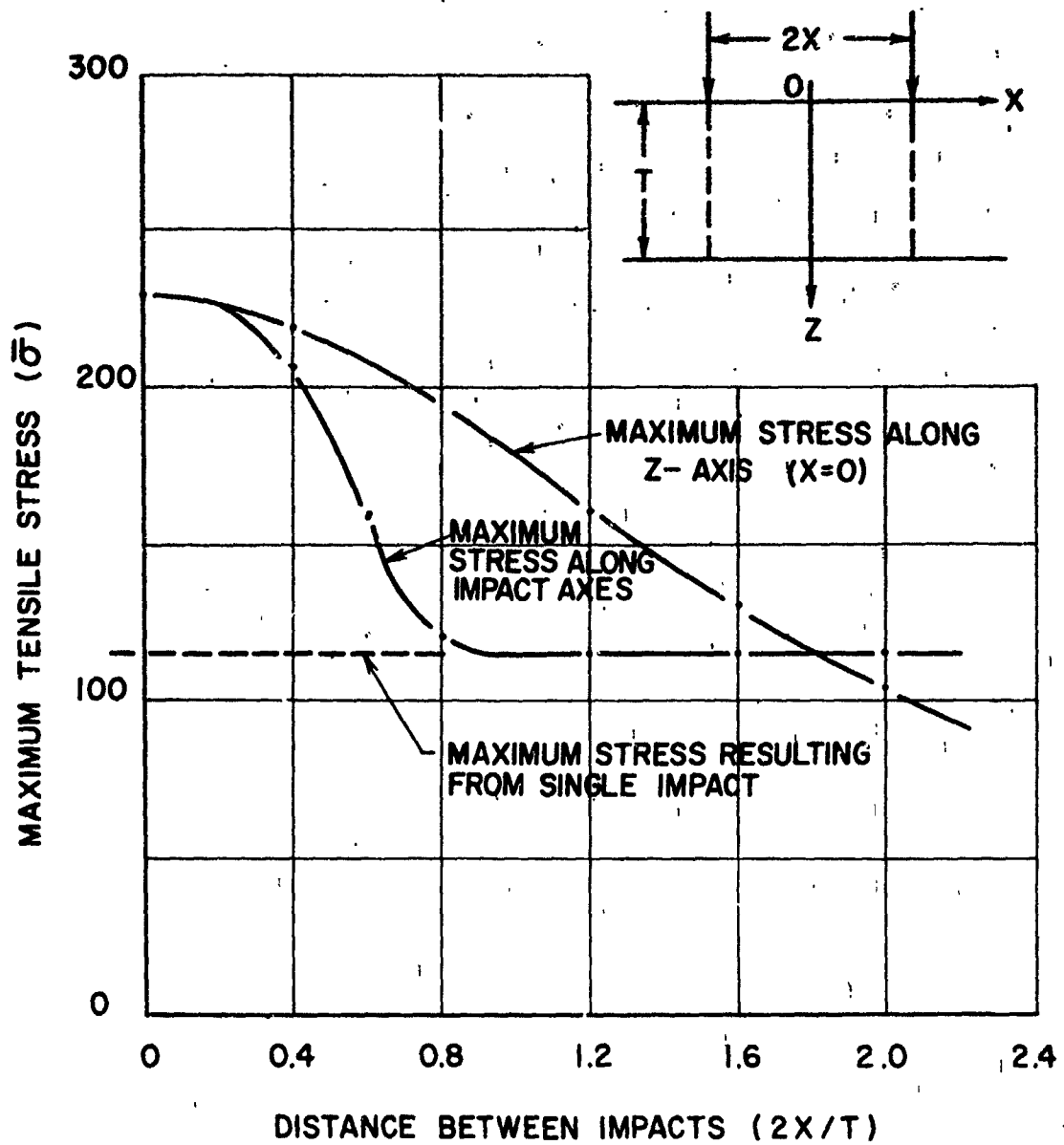
FIGURE 4.5   MAXIMUM TENSILE STRESS DUE TO REFLECTED WAVES
RESULTING FROM SIMULTANEOUS IMPACTS
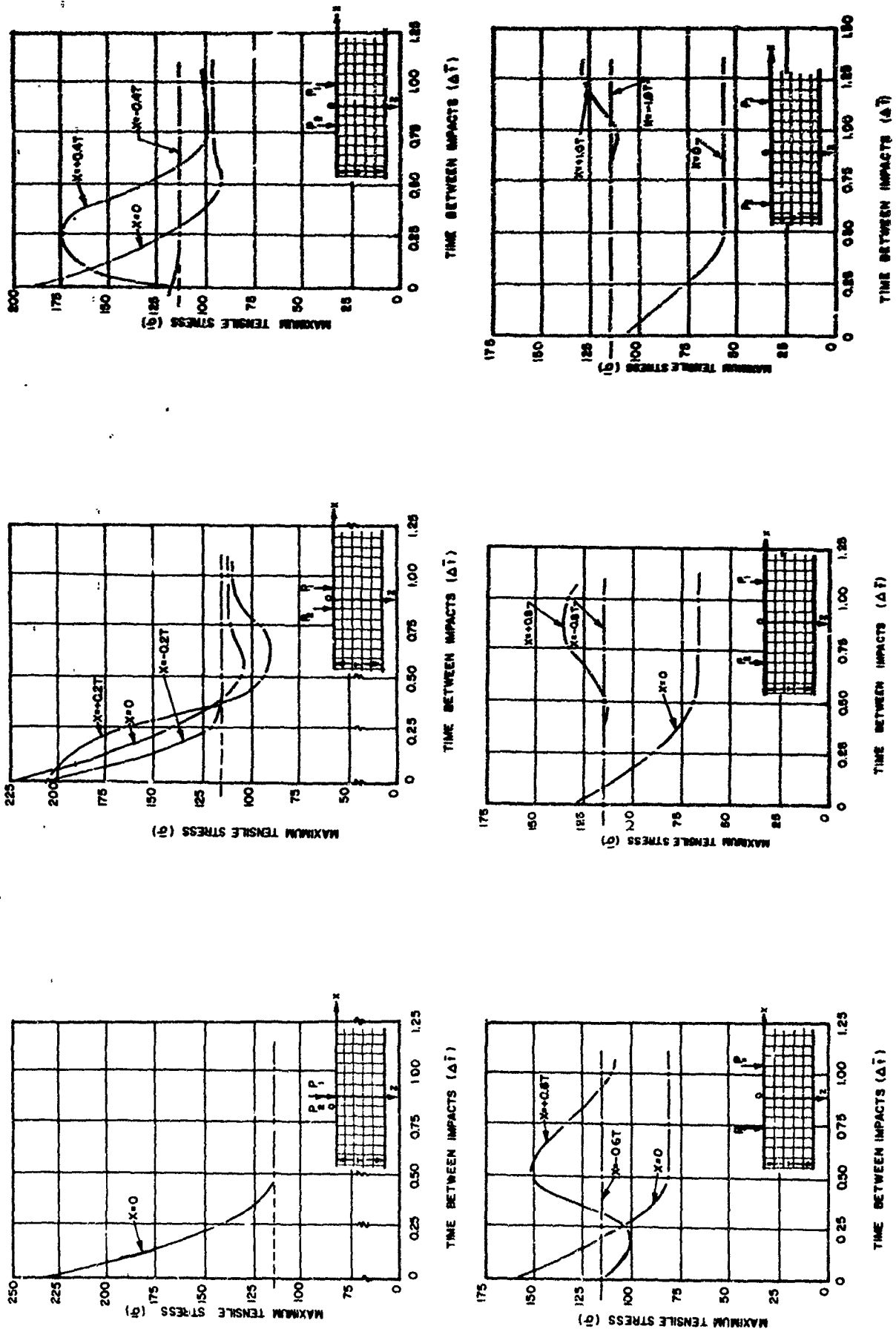
FIGURE 4.6   DEPENDENCE OF MAXIMUM STRESS UPON DISTANCE AND TIME BETWEEN IMPACTS
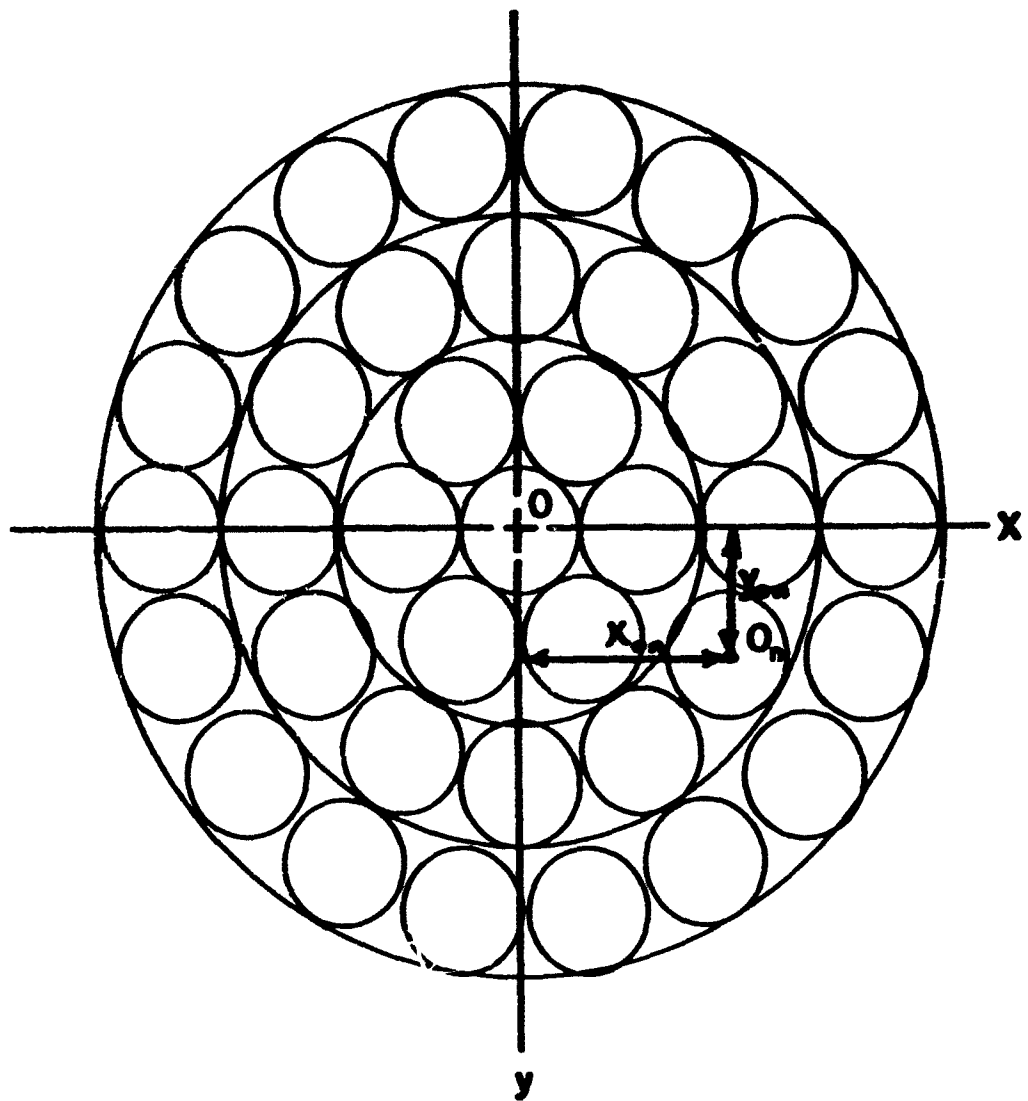
FIGURE 4.7   MULTIPLE STRESS WAVE SOURCES
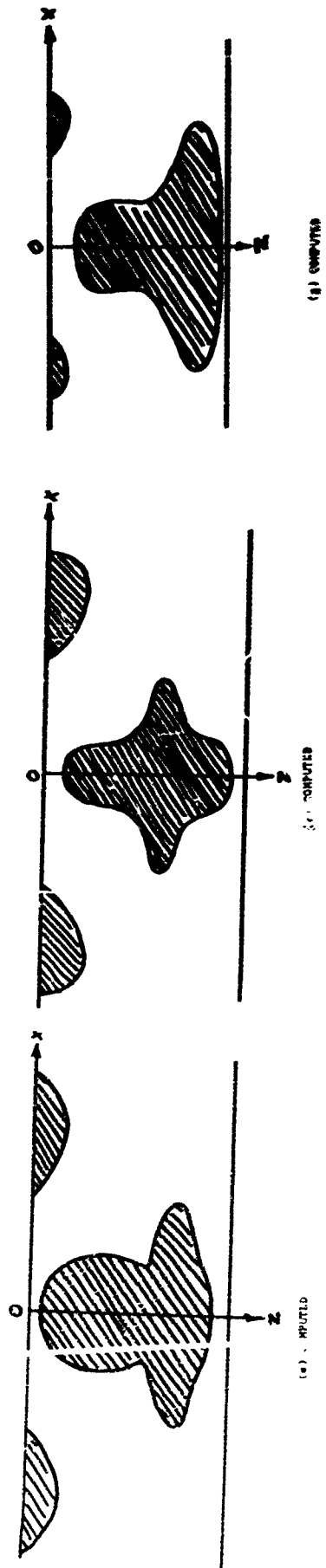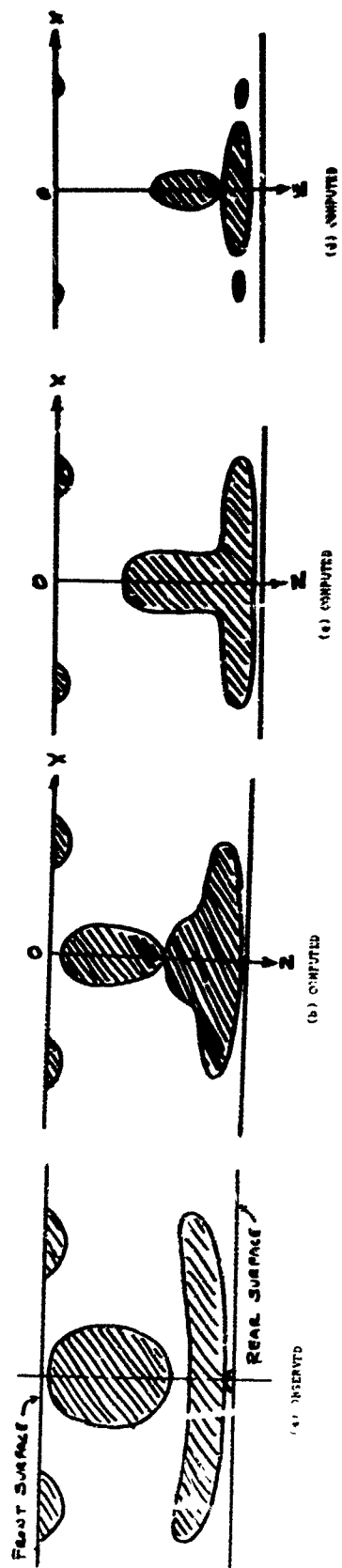
FIGURE 4.8   FRACTURES IN PLACTIC TARGETS FOR
VARIOUS IMPACT PARAMETERS
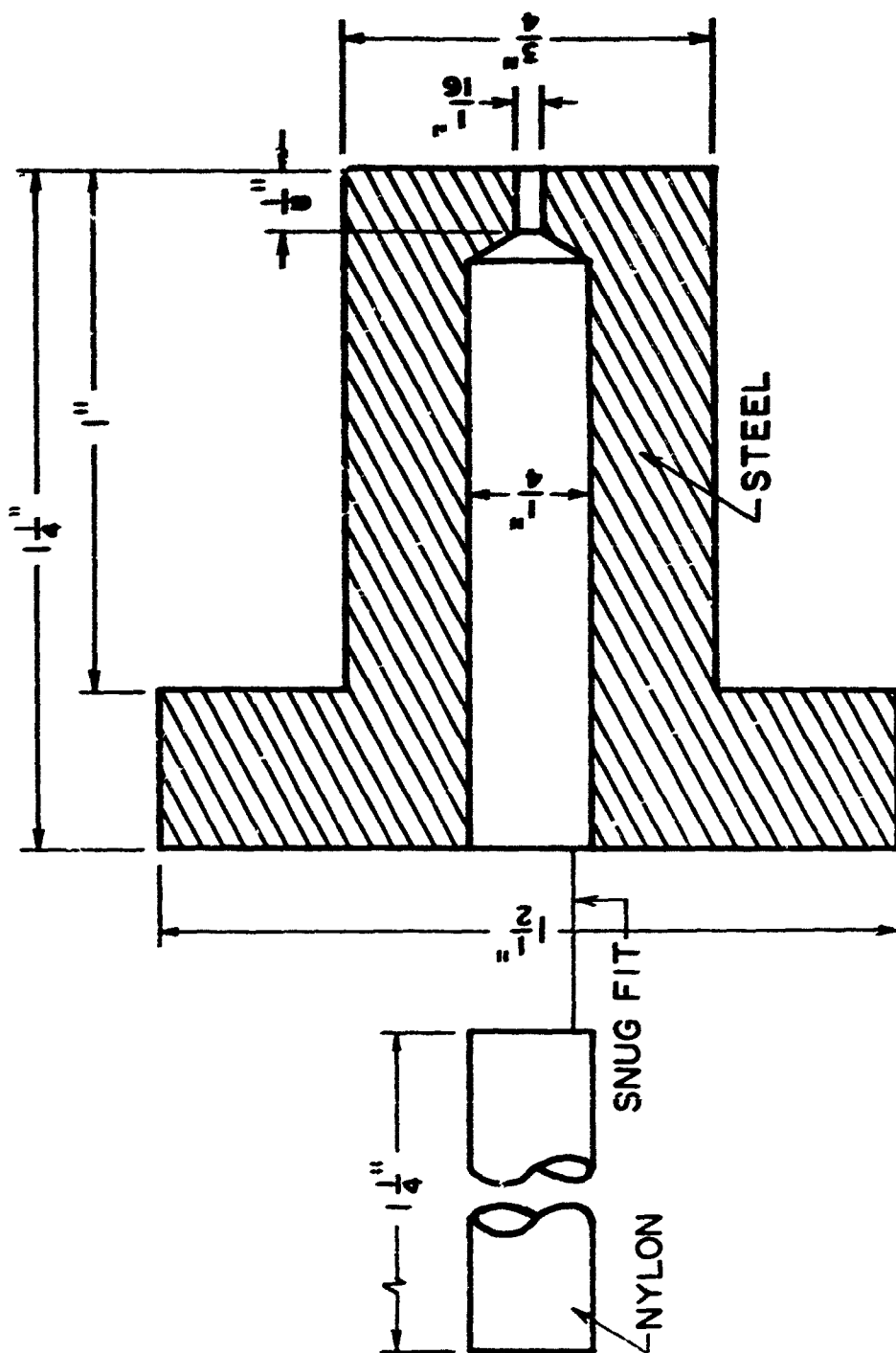
FIGURE 5.1 WATER JET ACCELERATOR
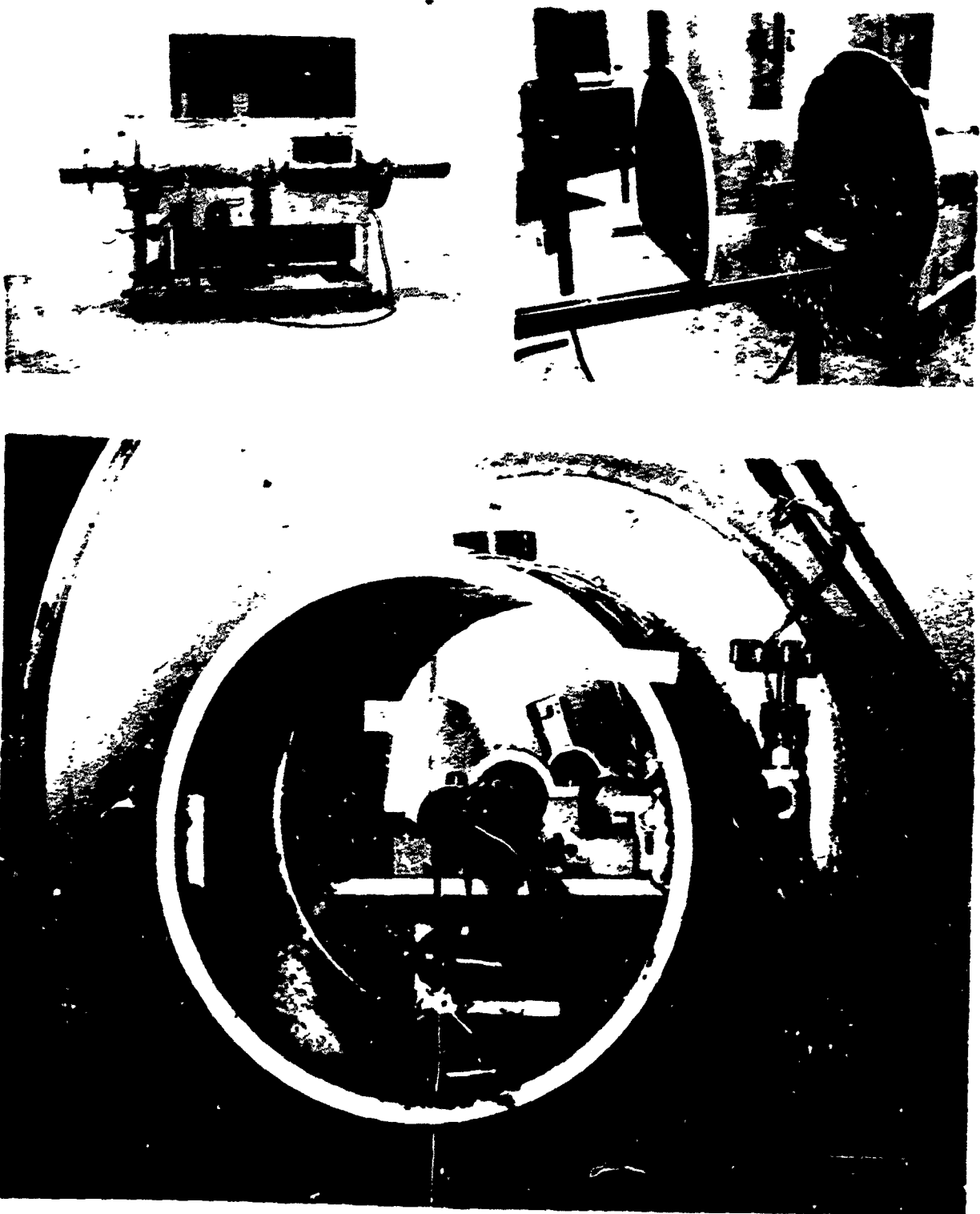
FIGURE 5.2 IMPACT RANGE
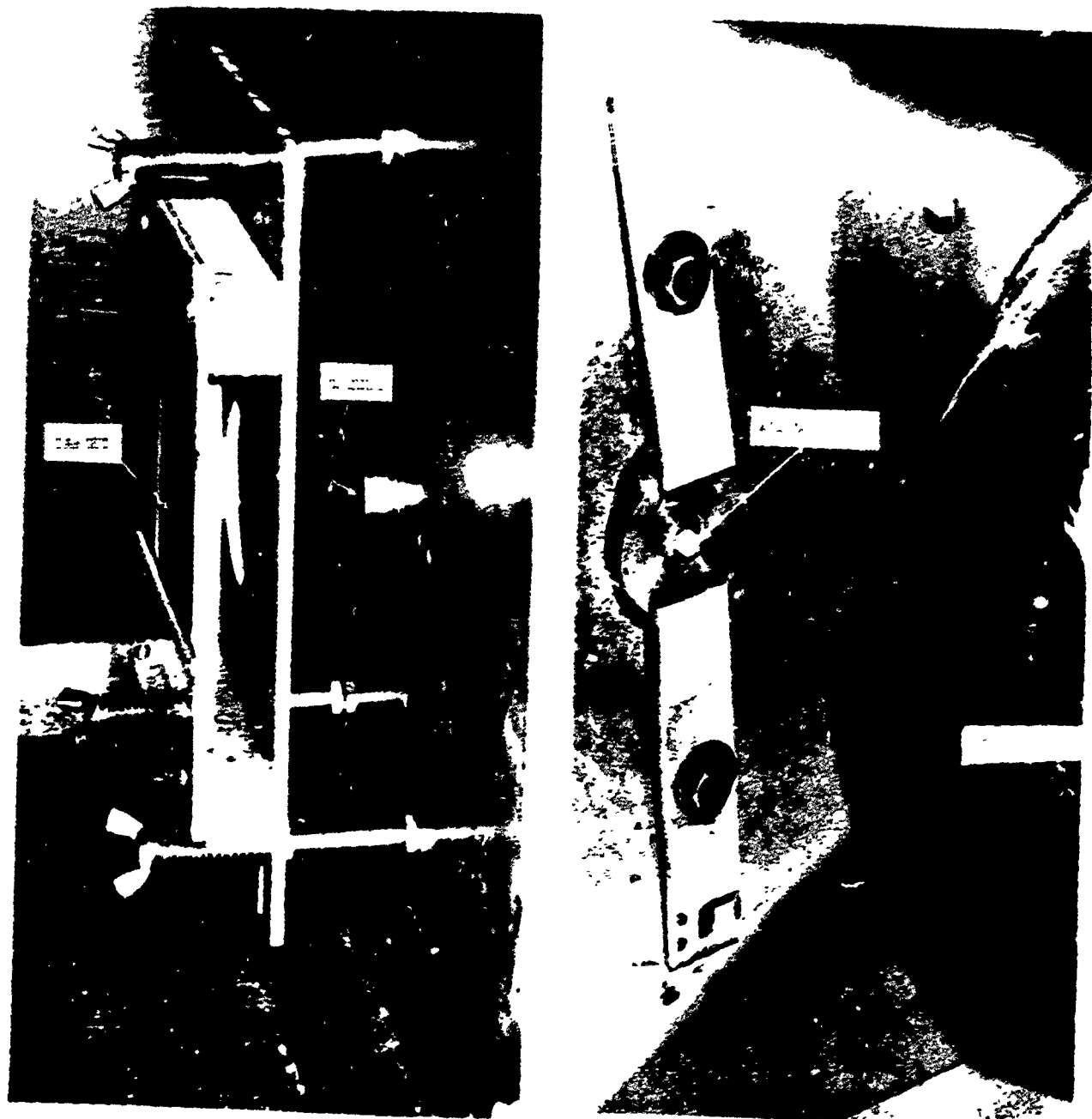
FIGURE 5.2 — CONTINUED

FIGURE 5.3 HIGH-SPEED WATER JET

FIGURE 5.4 WATER IMPACT DAMAGE TO LUCITE TARGETS
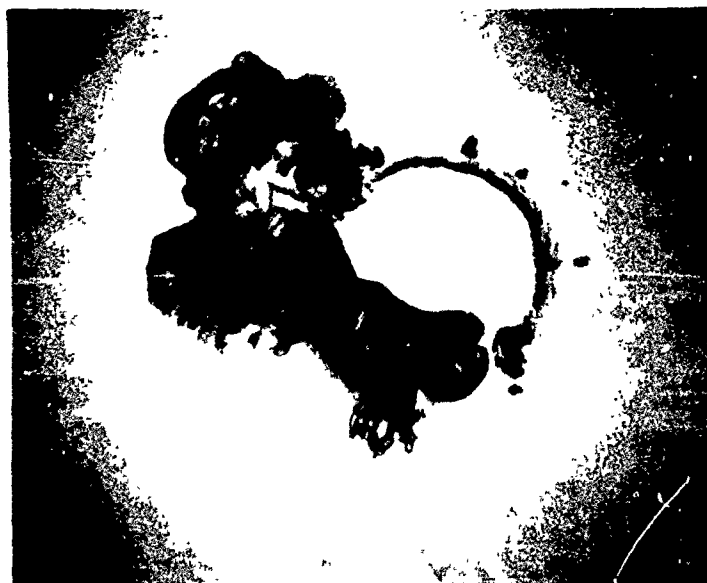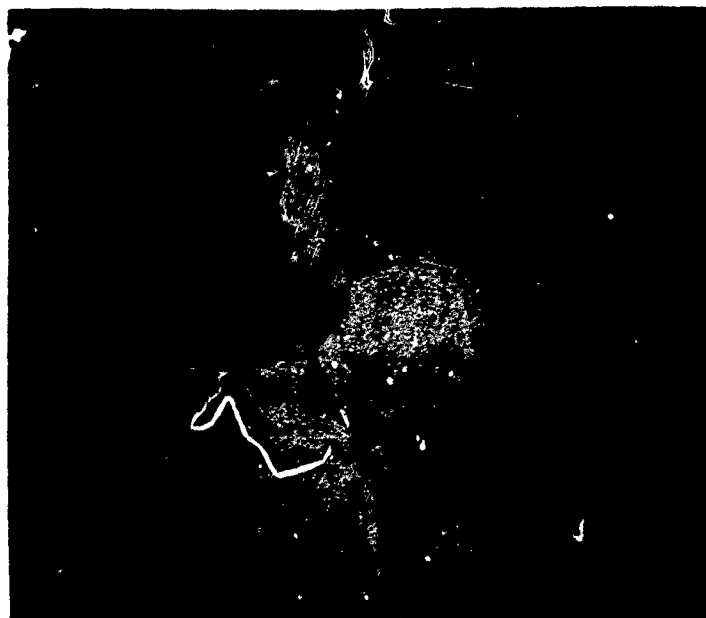
FIGURE 5.4   CONTINUED
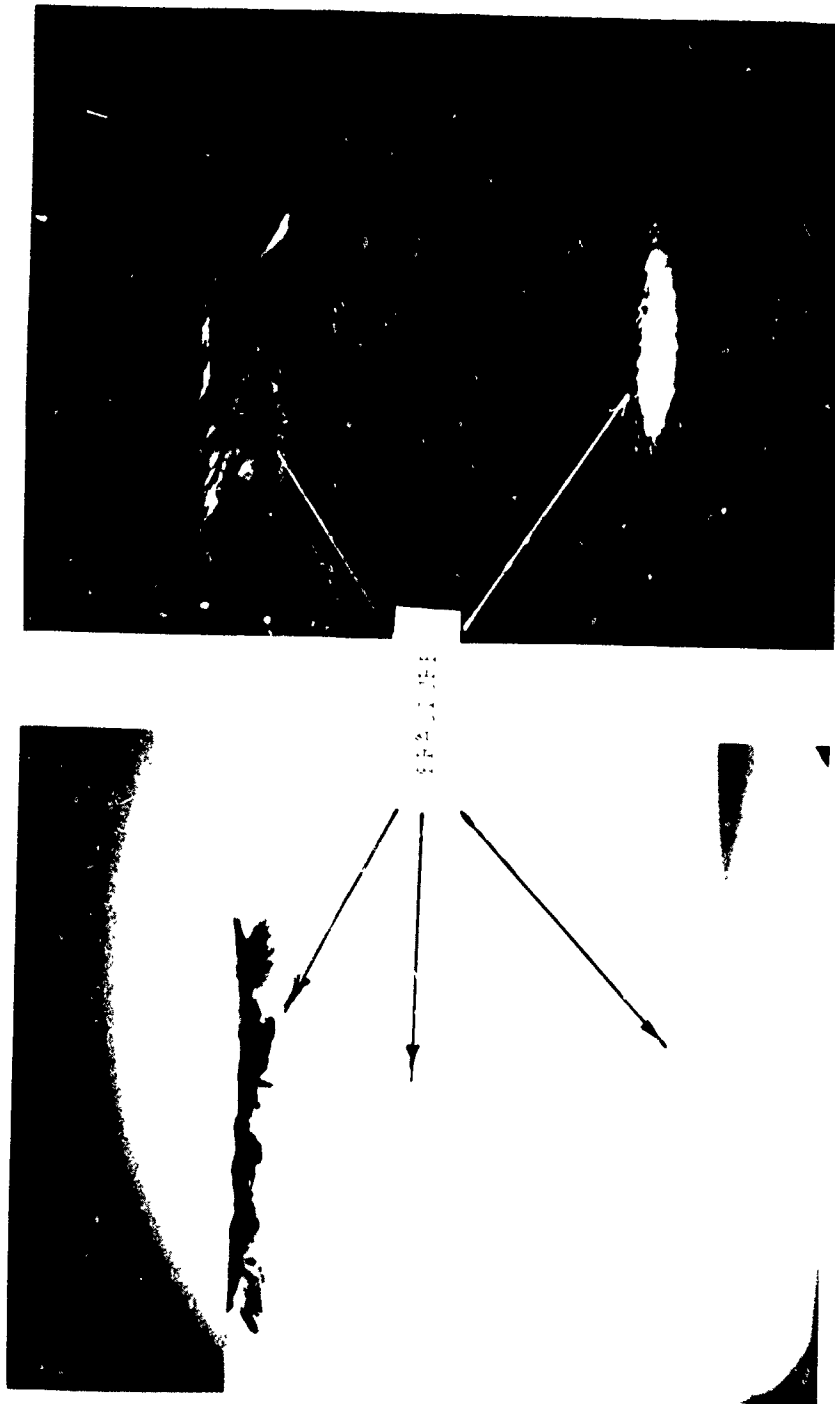
FIGURE 5.5   SIDE VIEW OF LUCITE TARGETS
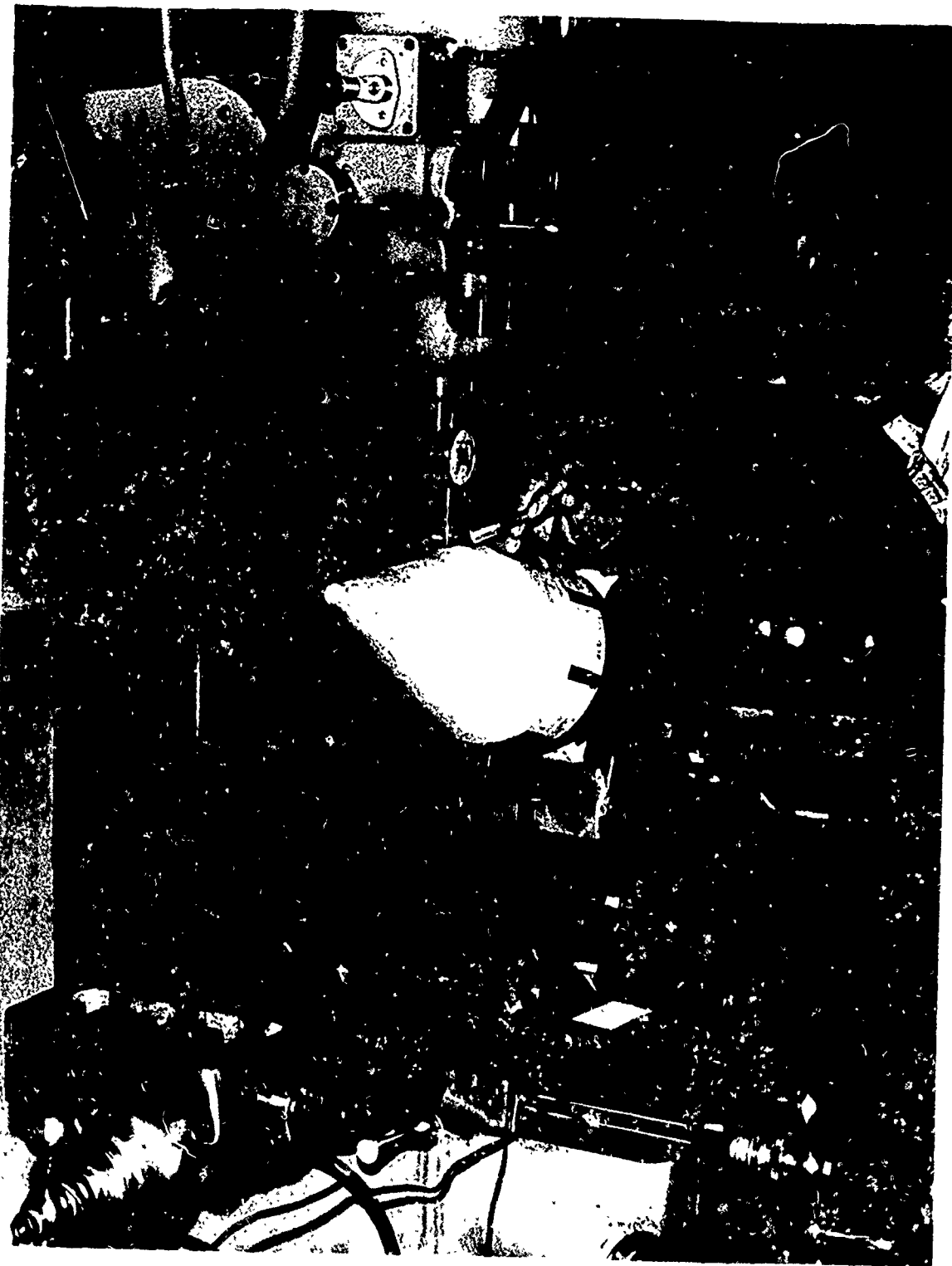
FIGURE 5.6 MEASURING CRATER DEPTHS
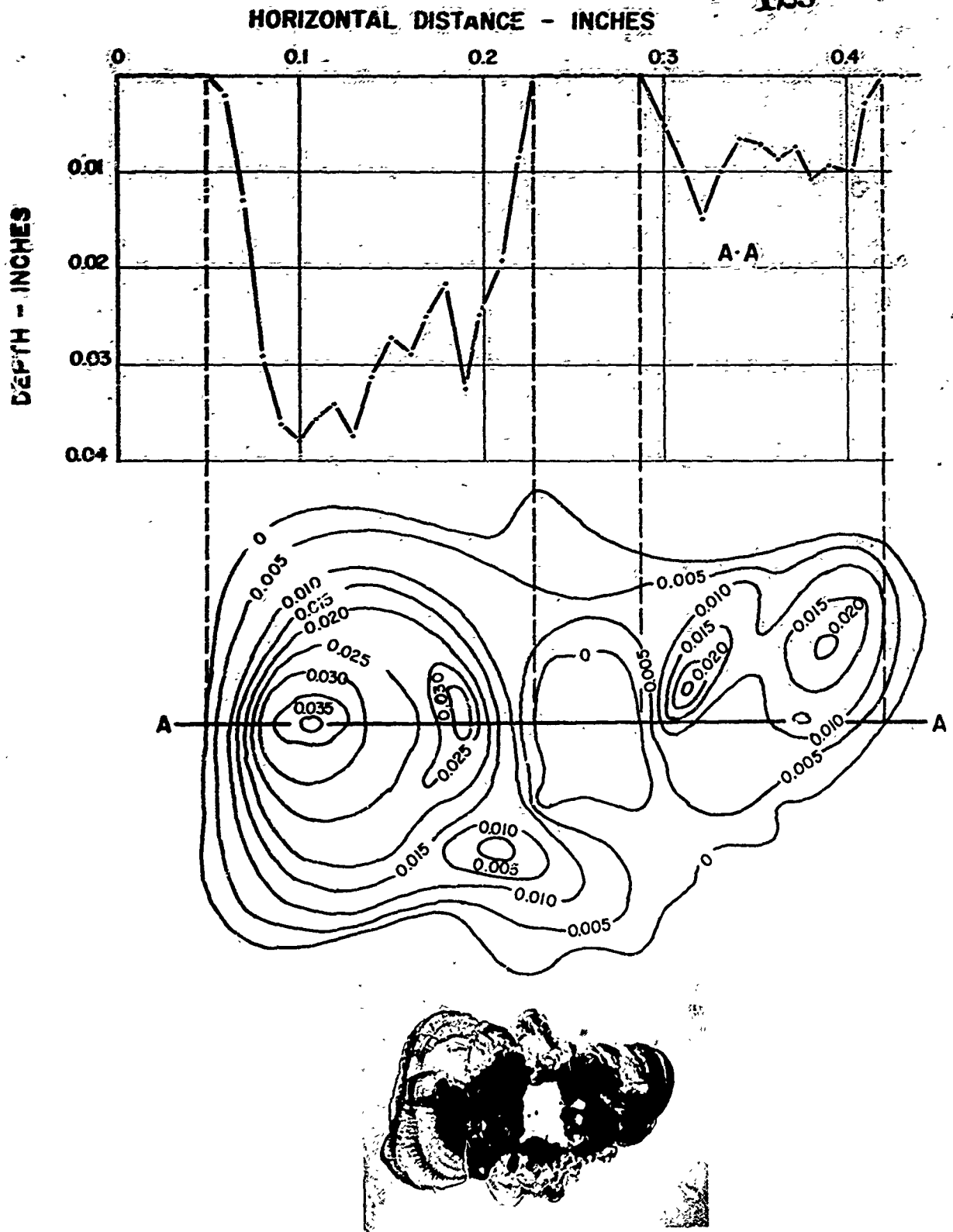
FIGURE 5.7 PROFILE AND DEPTH CONTOURS OF CRATER IN LUCITE
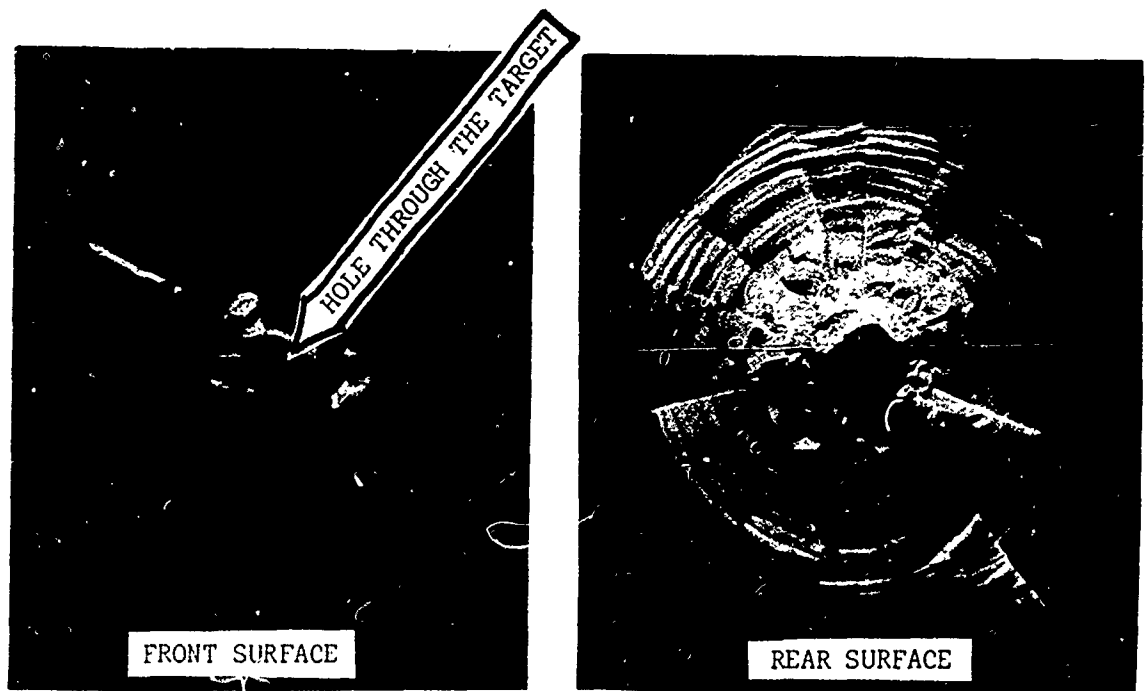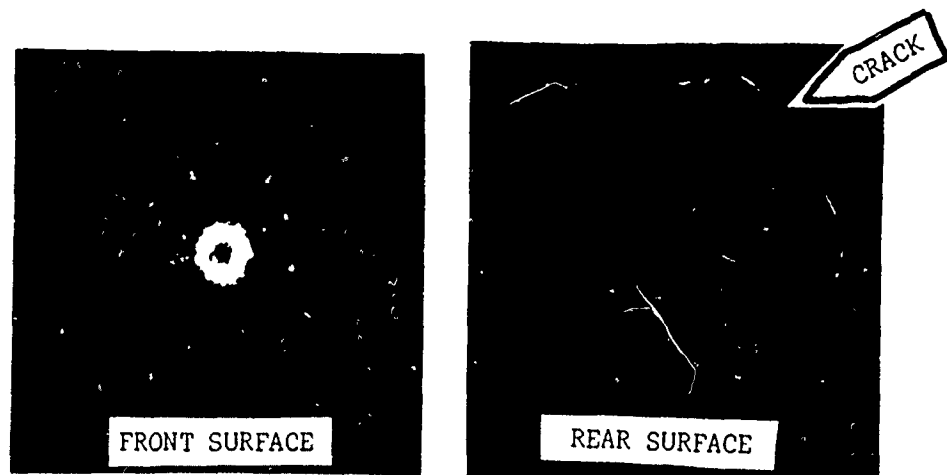
FIGURE 5.8 WATER IMPACT DAMAGE TO FUSED SILICA TARGETS
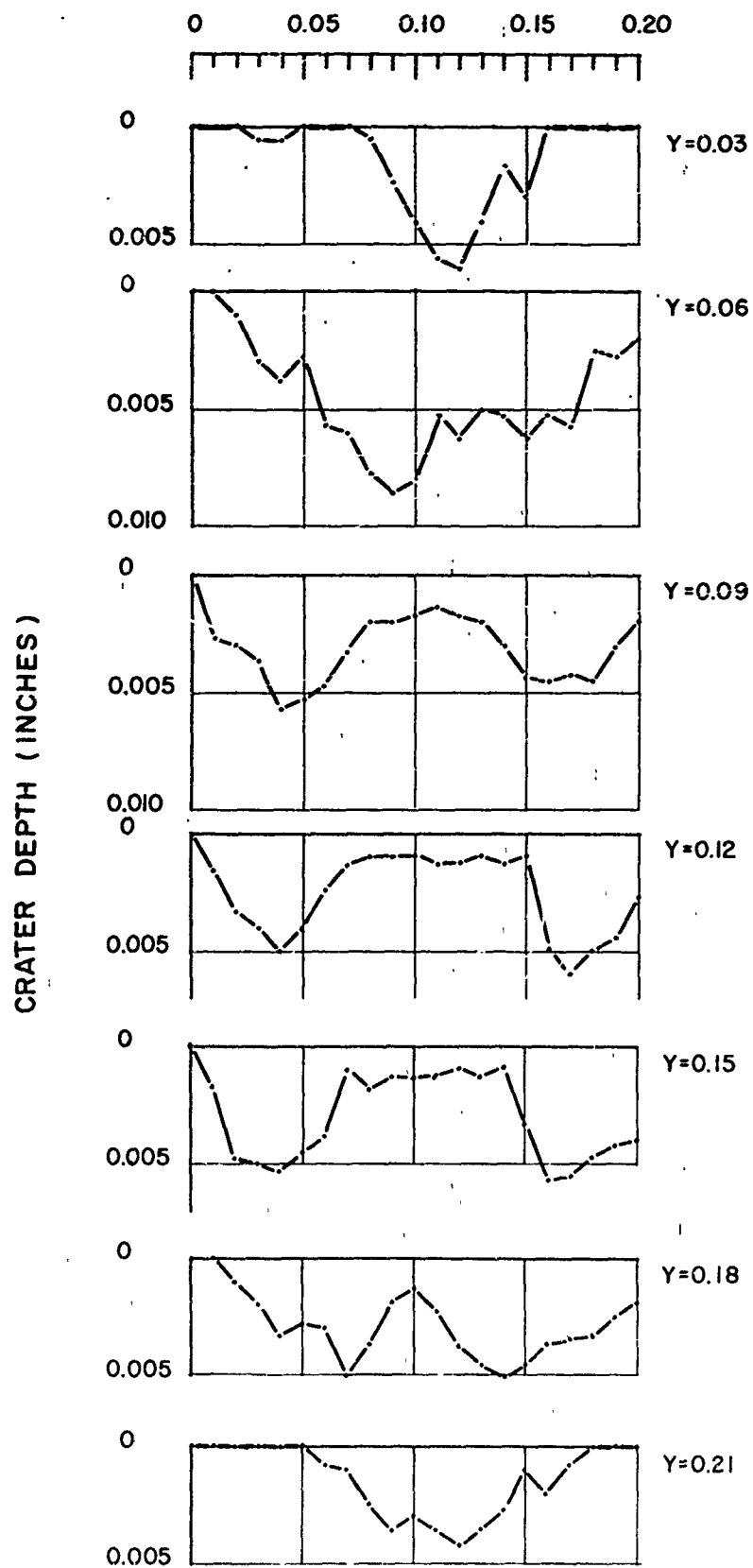
FIGURE 5.9   CRATER CROSS SECTIONS (FUSED SILICA)

X (INCHES)
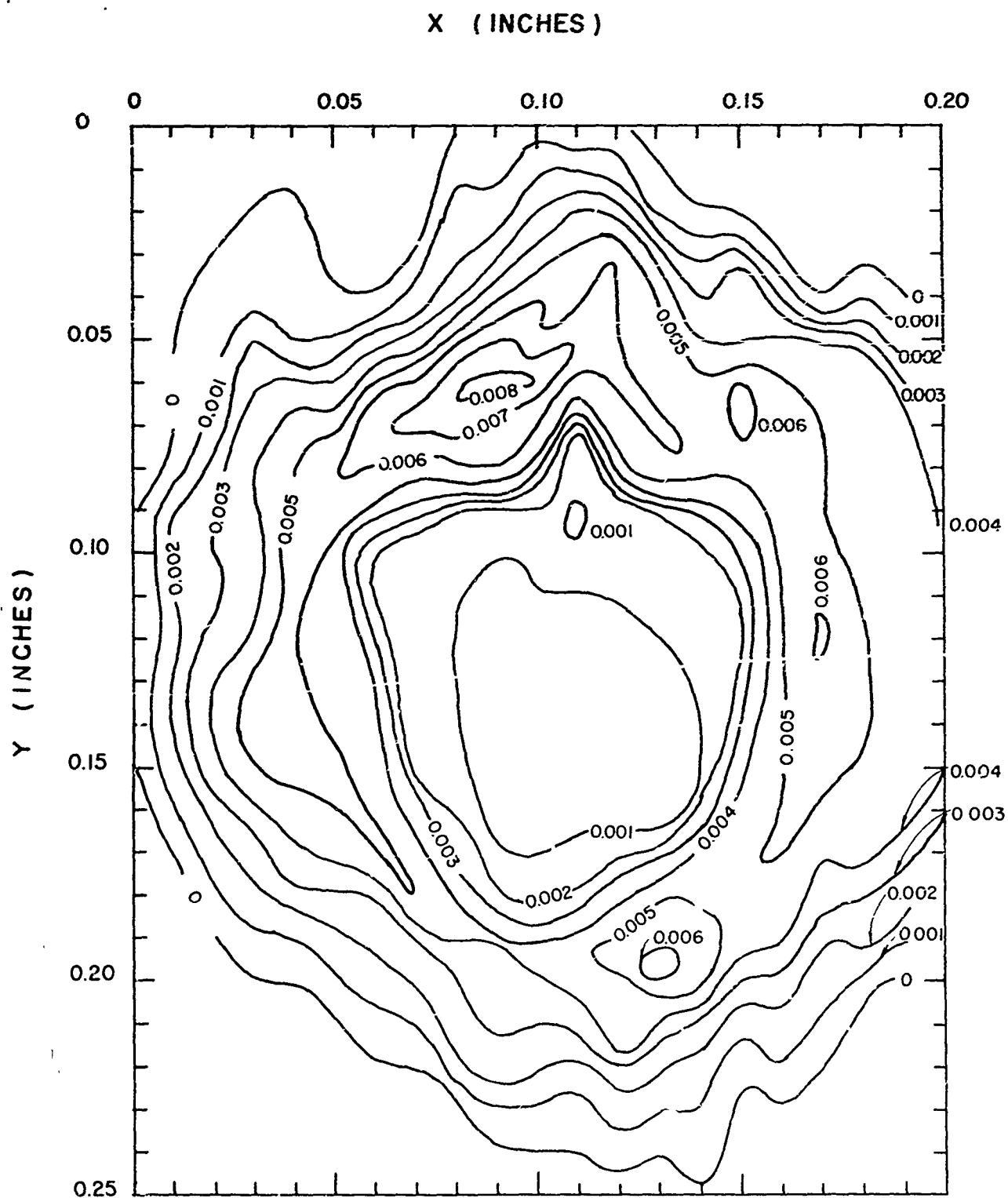
FIGURE 5.10   CRATER DEPTH CONTOURS (FUSED SILICA)

133

FRONT SURFACE

REAR SURFACE

METRIC 1 2 3 4 5
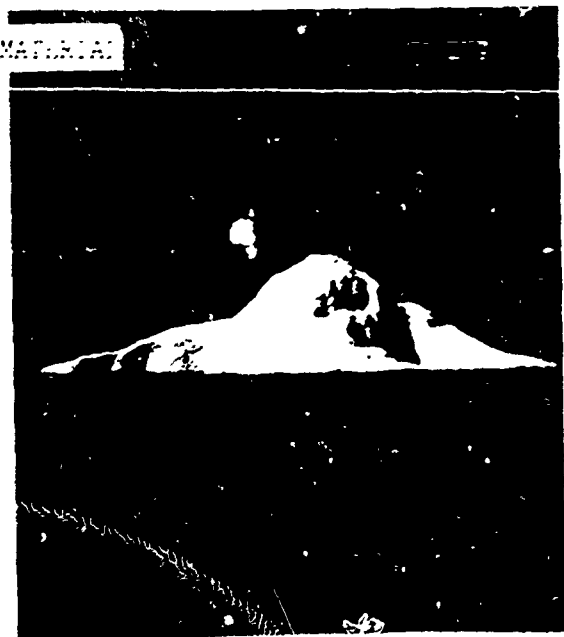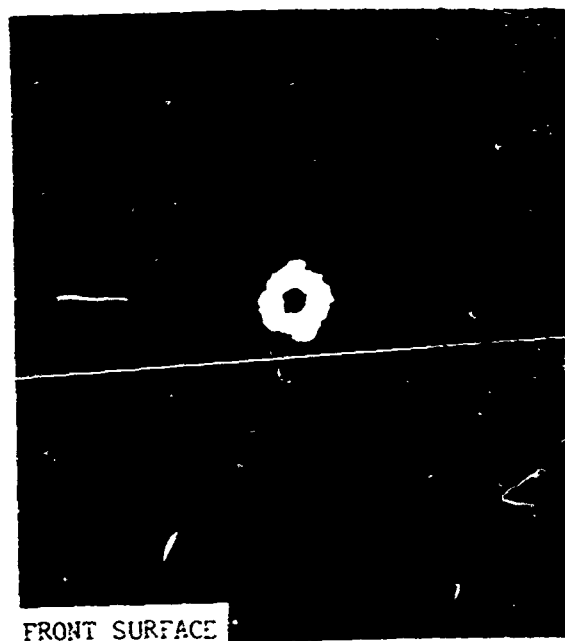
FIGURE 5.11   WATER IMPACT DAMAGE TO FUSED SILICA TARGET
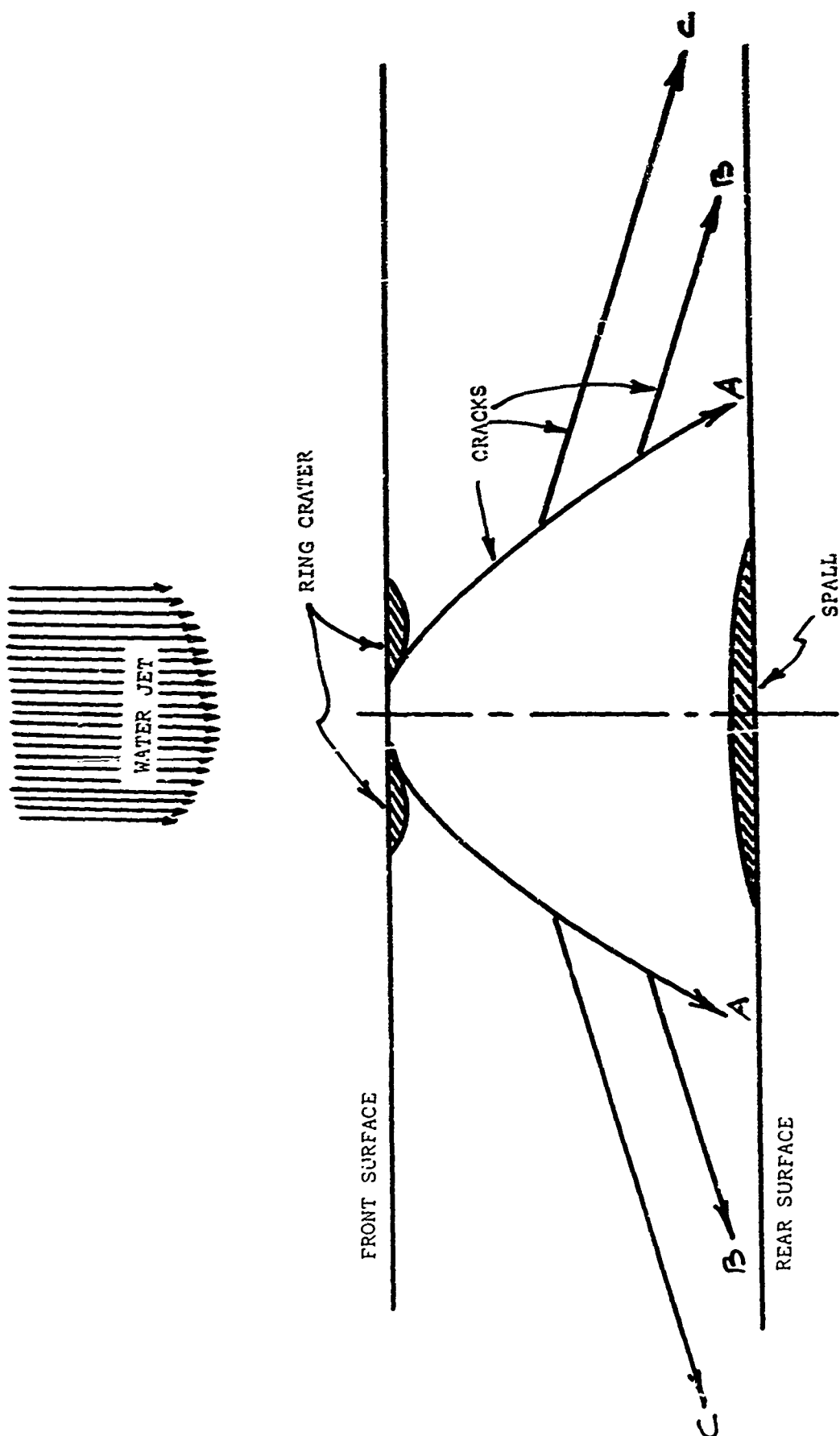
FIGURE 5.12 FRACTURE LOCATIONS
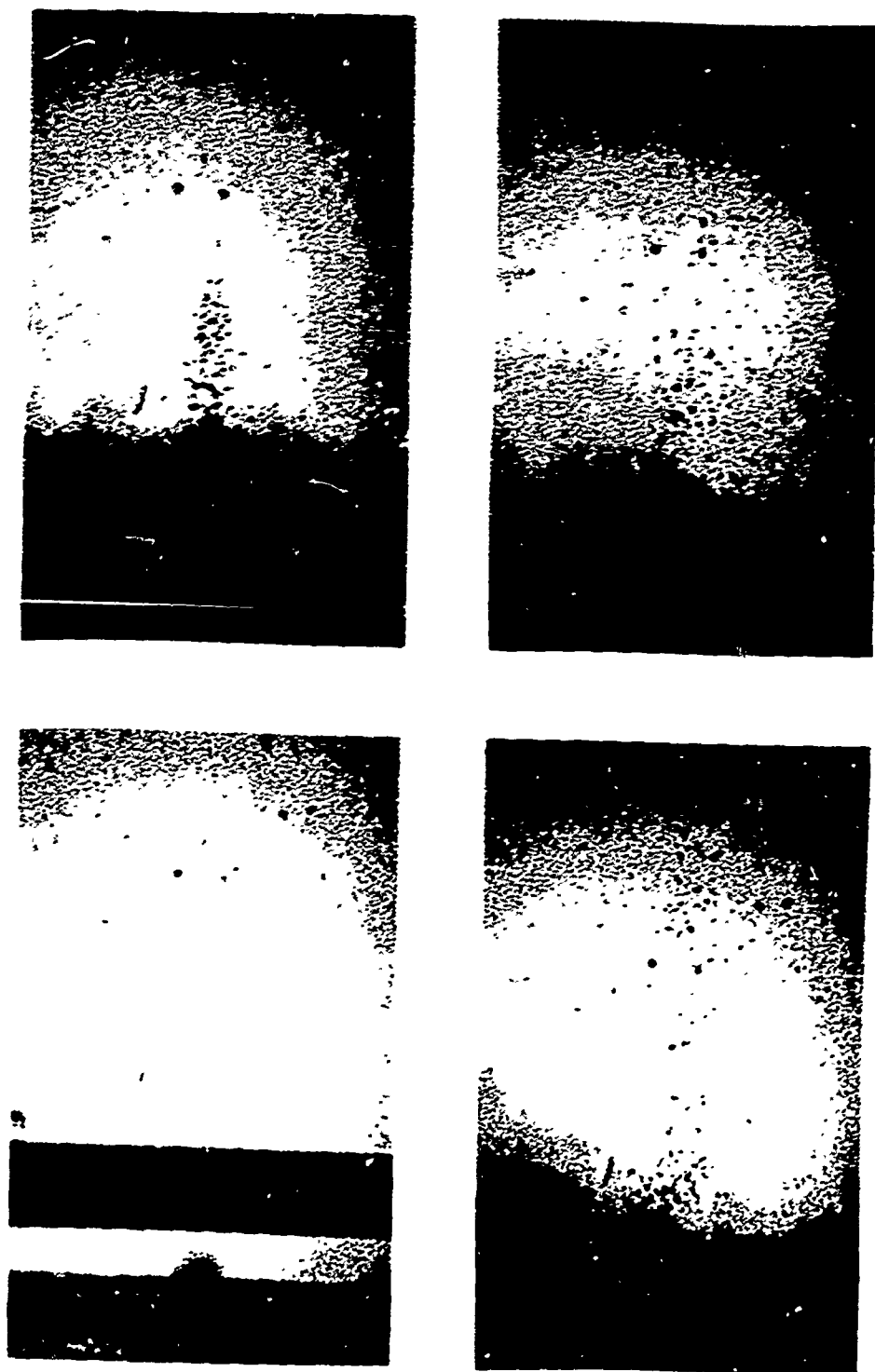
FIGURE 5.13 EJECTA FROM REAR SURFACE SPALL.
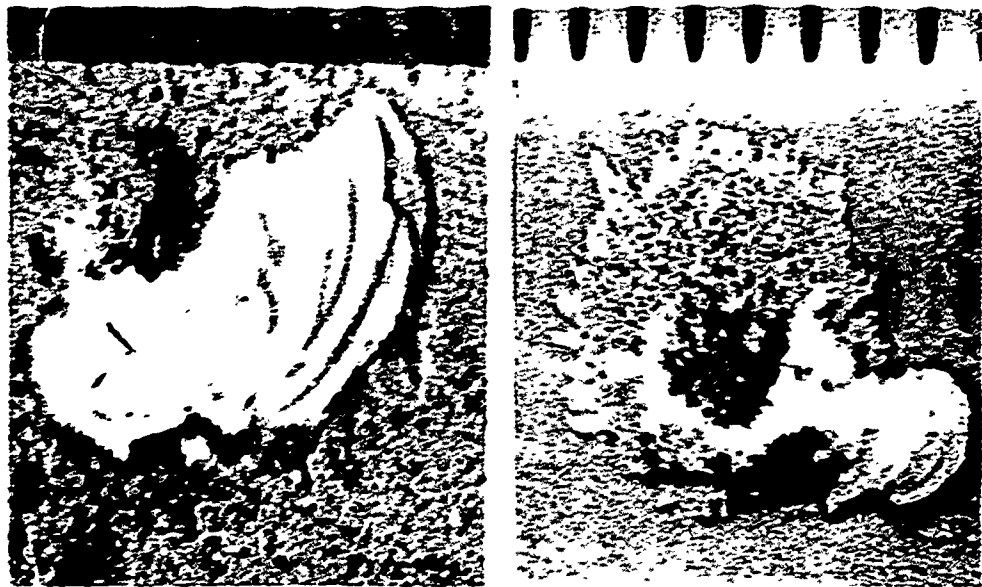
60-DEGREE
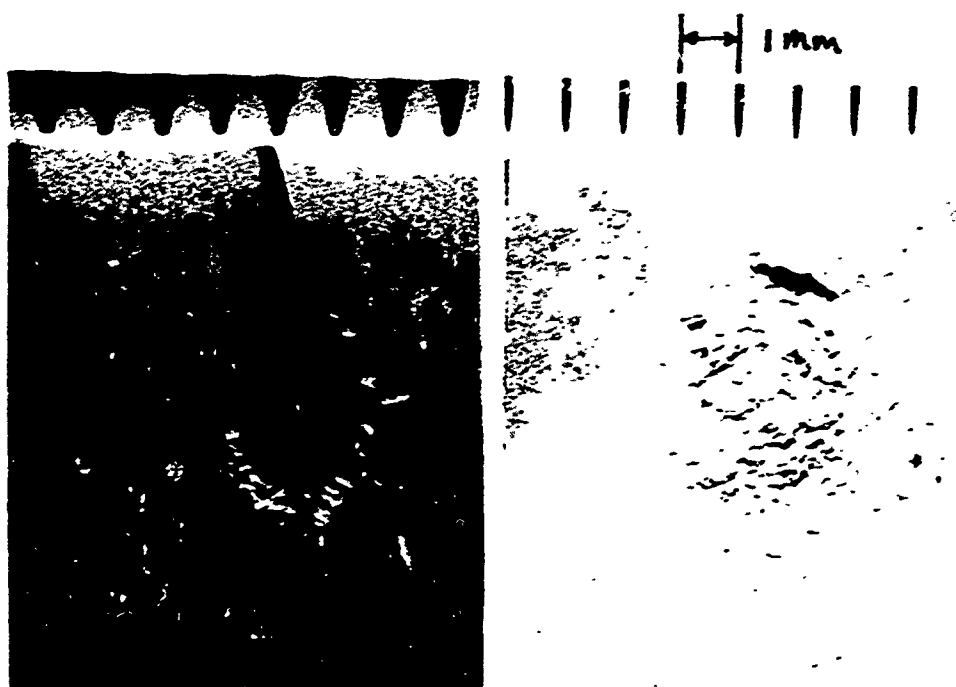
30-DEGREE

FIGURE 5.14   SURFACE DAMAGE RESULTING FROM OBLIQUE IMPACTS
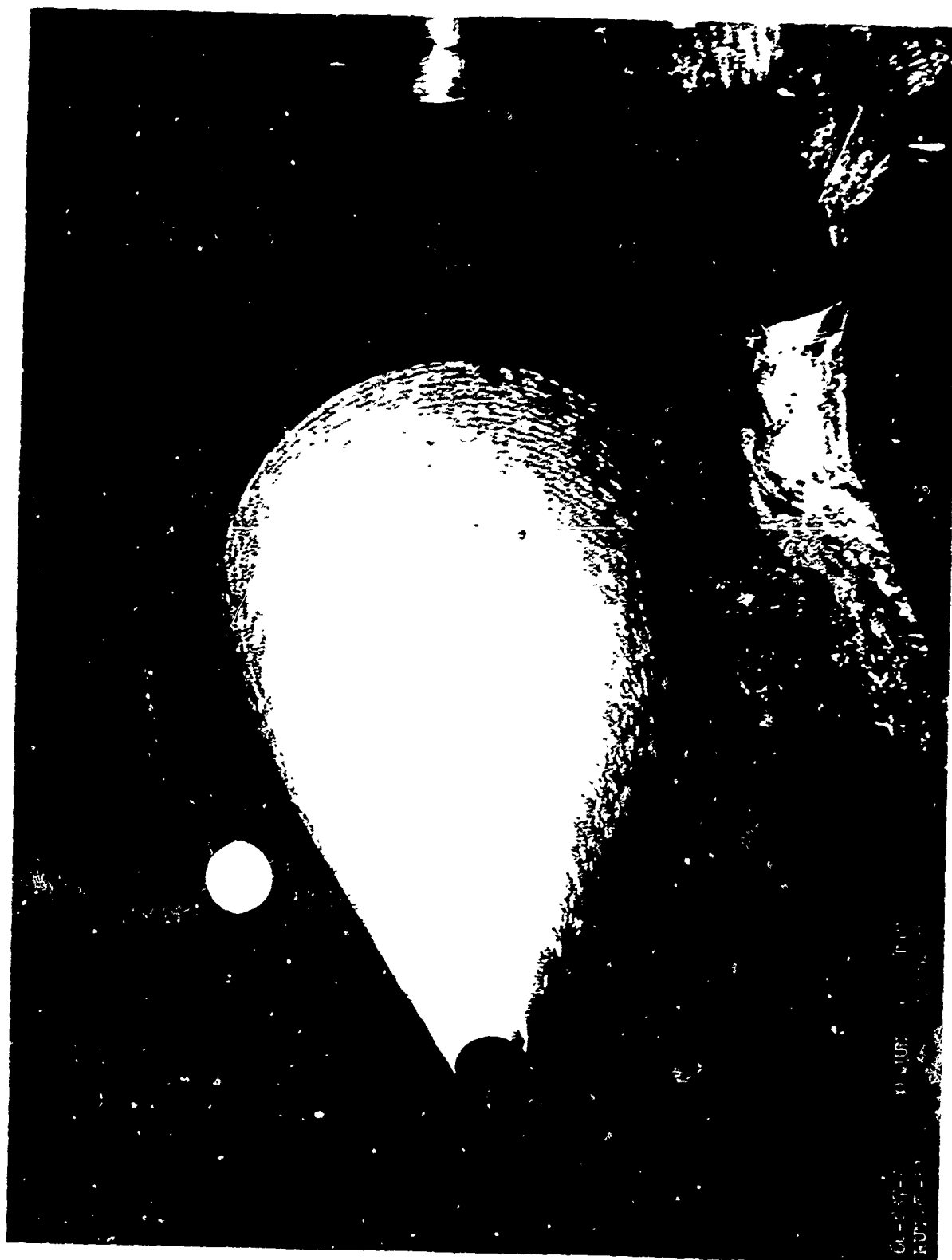
FIGURE 6.1 RADOME ON SLED AFTER TEST AT HOLLOMAN AFB
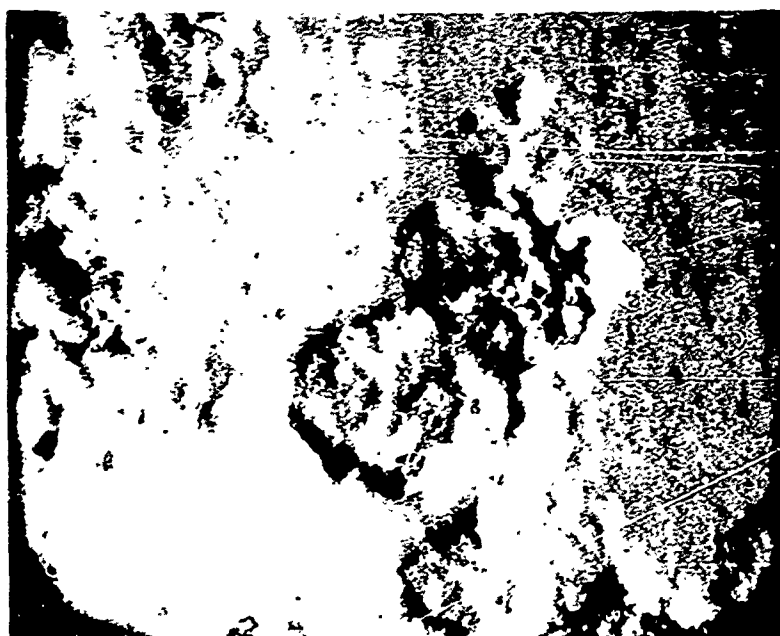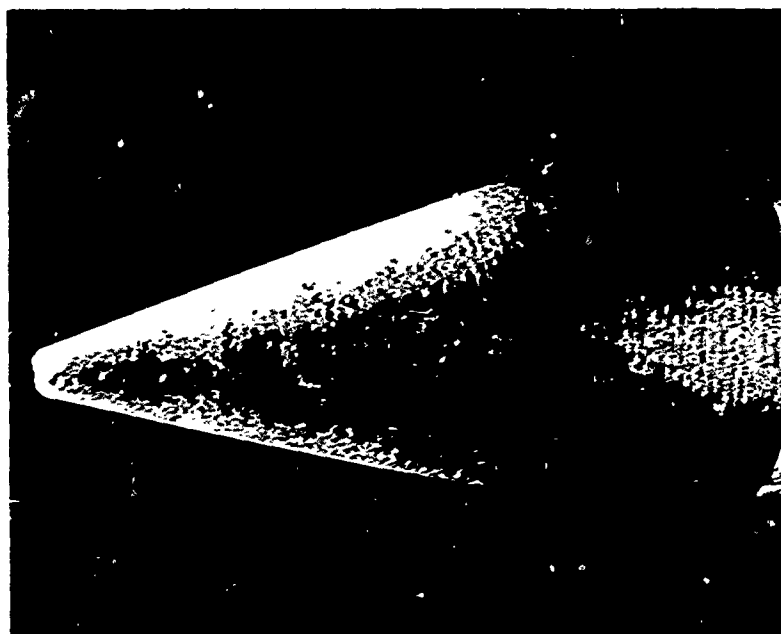
FIGURE 6.2 RADOME AND CLOSE-UP OF CRATERS
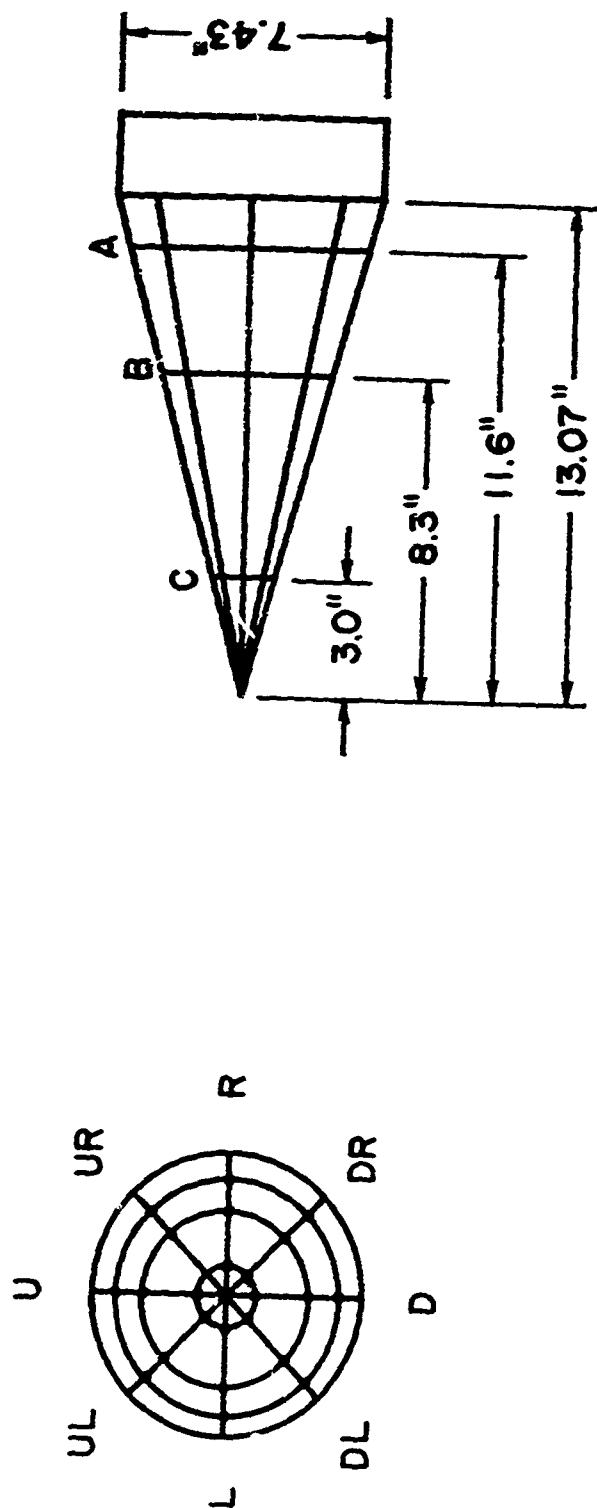
FIGURE 6.3 DIMENSIONS OF RADOME
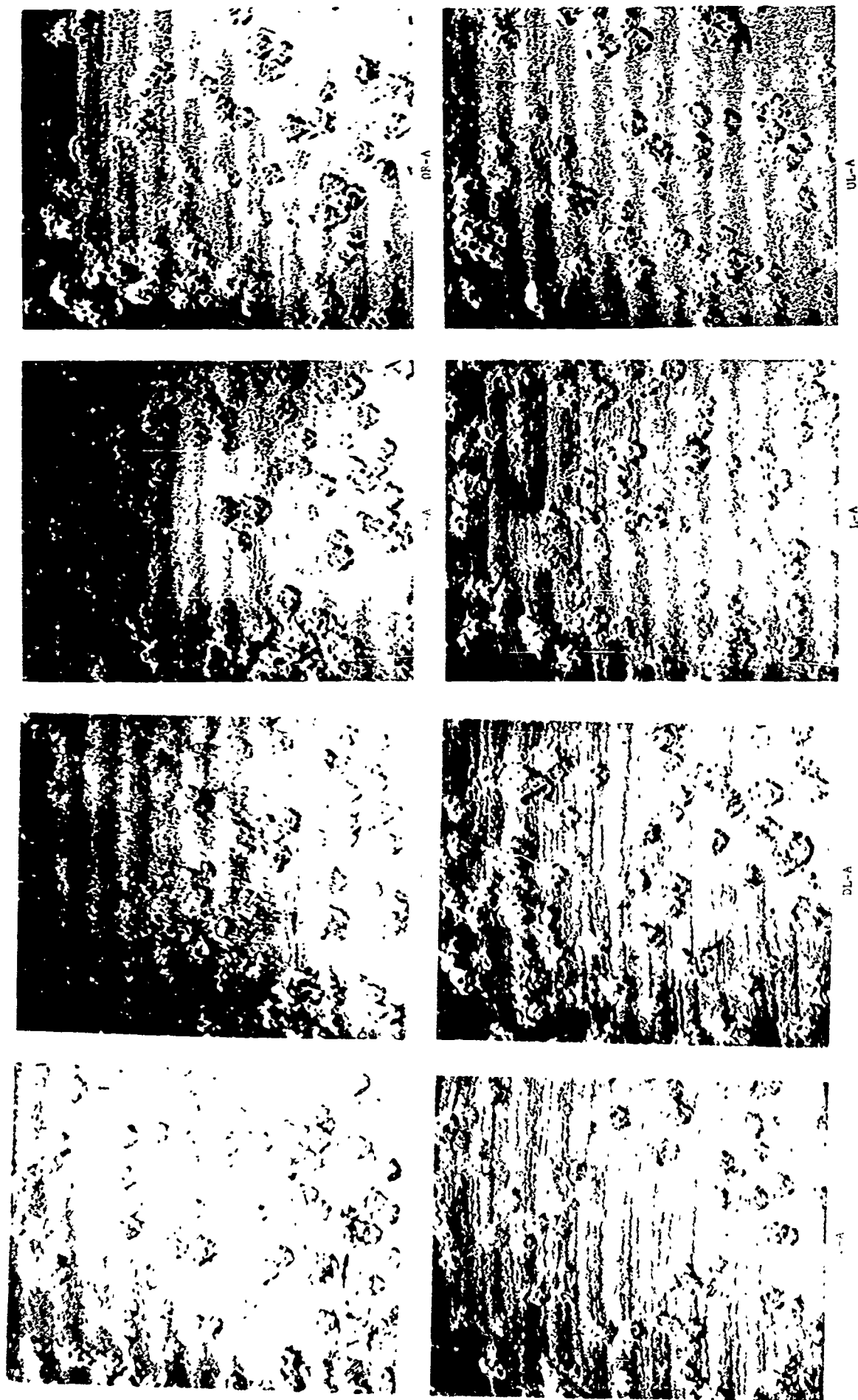
FIGURE 6.4 PHOTOGRAPHS OF CRATERS NEAR BASE
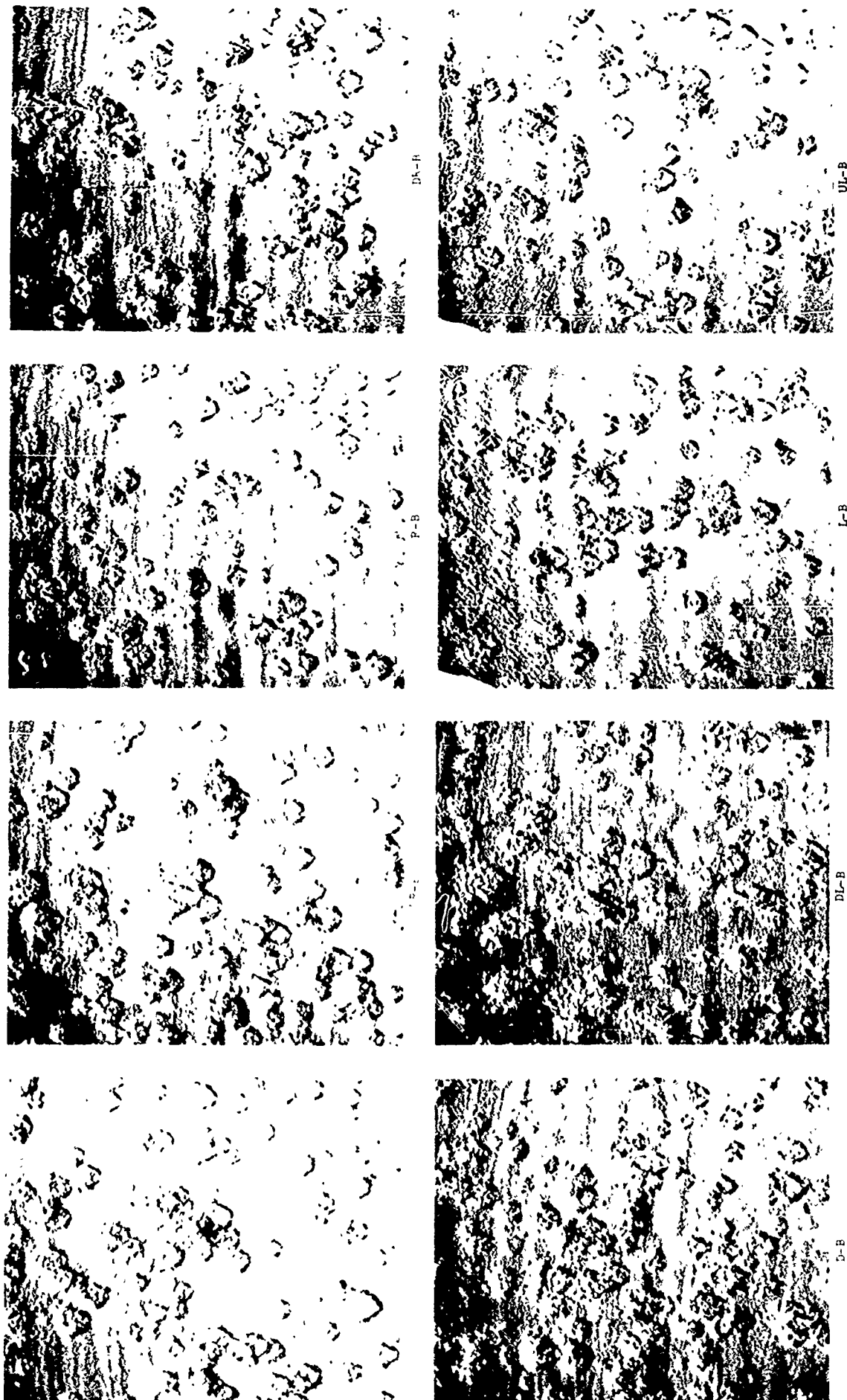
FIGURE 6.5 PHOTOGRAPHS OF CRATERS NEAR MID-SECTION
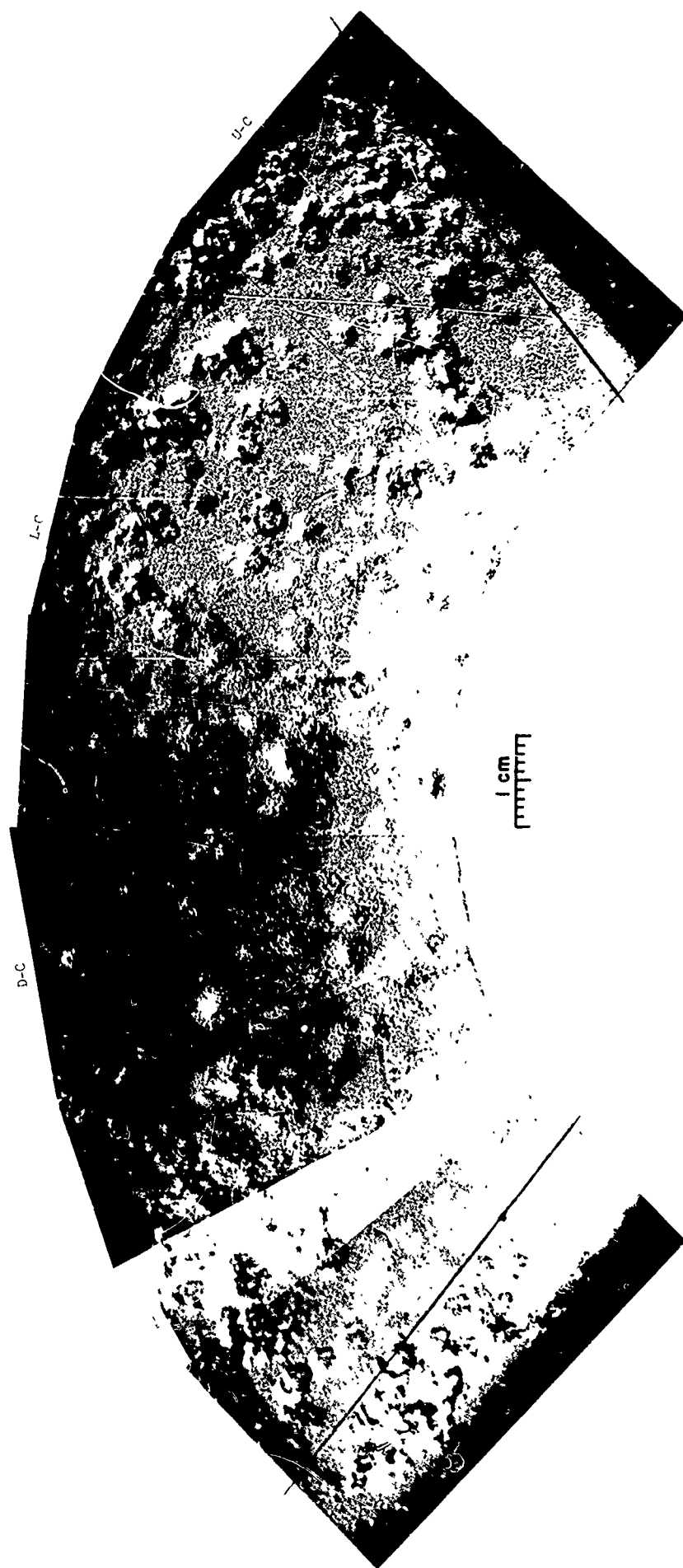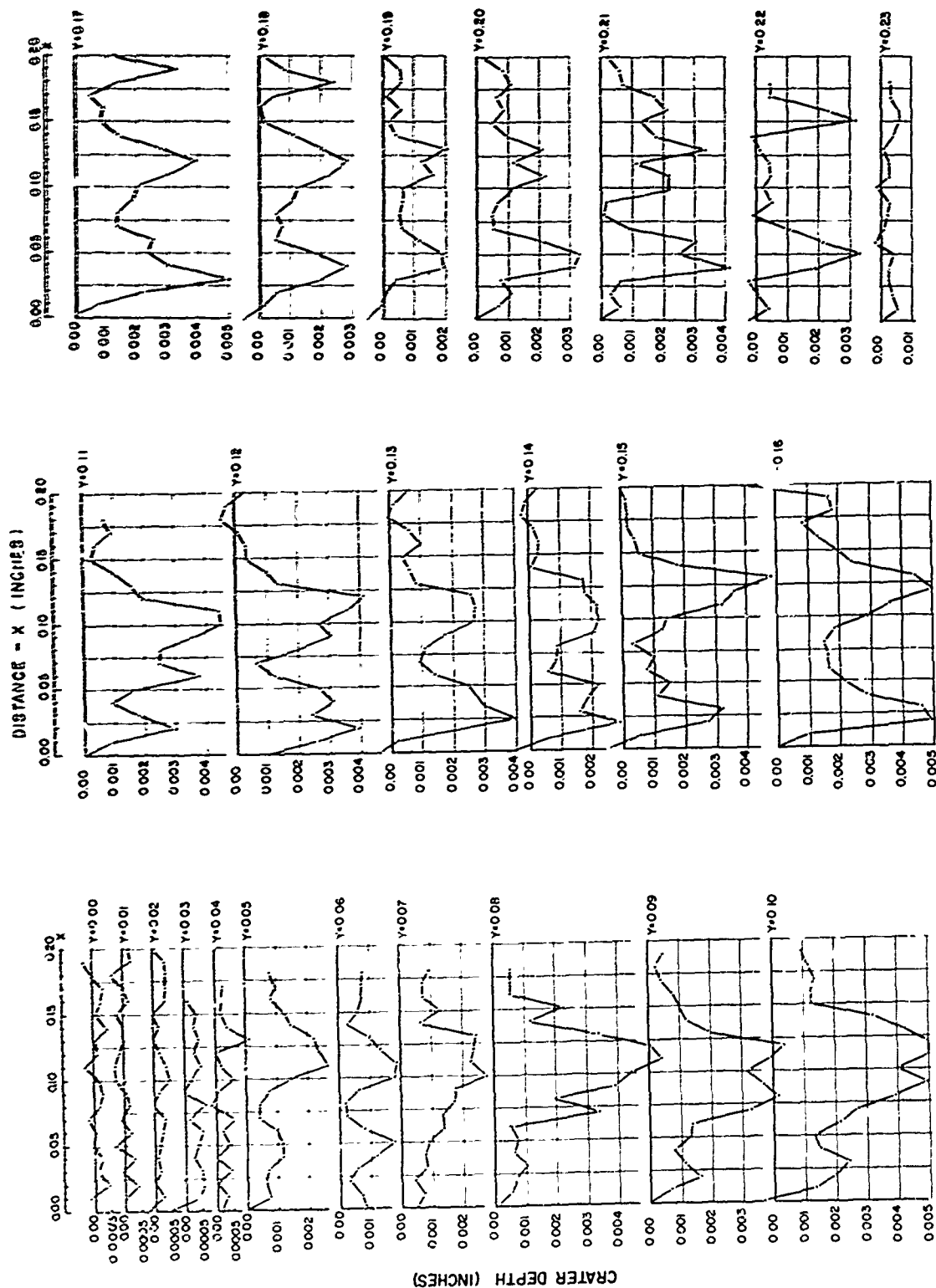
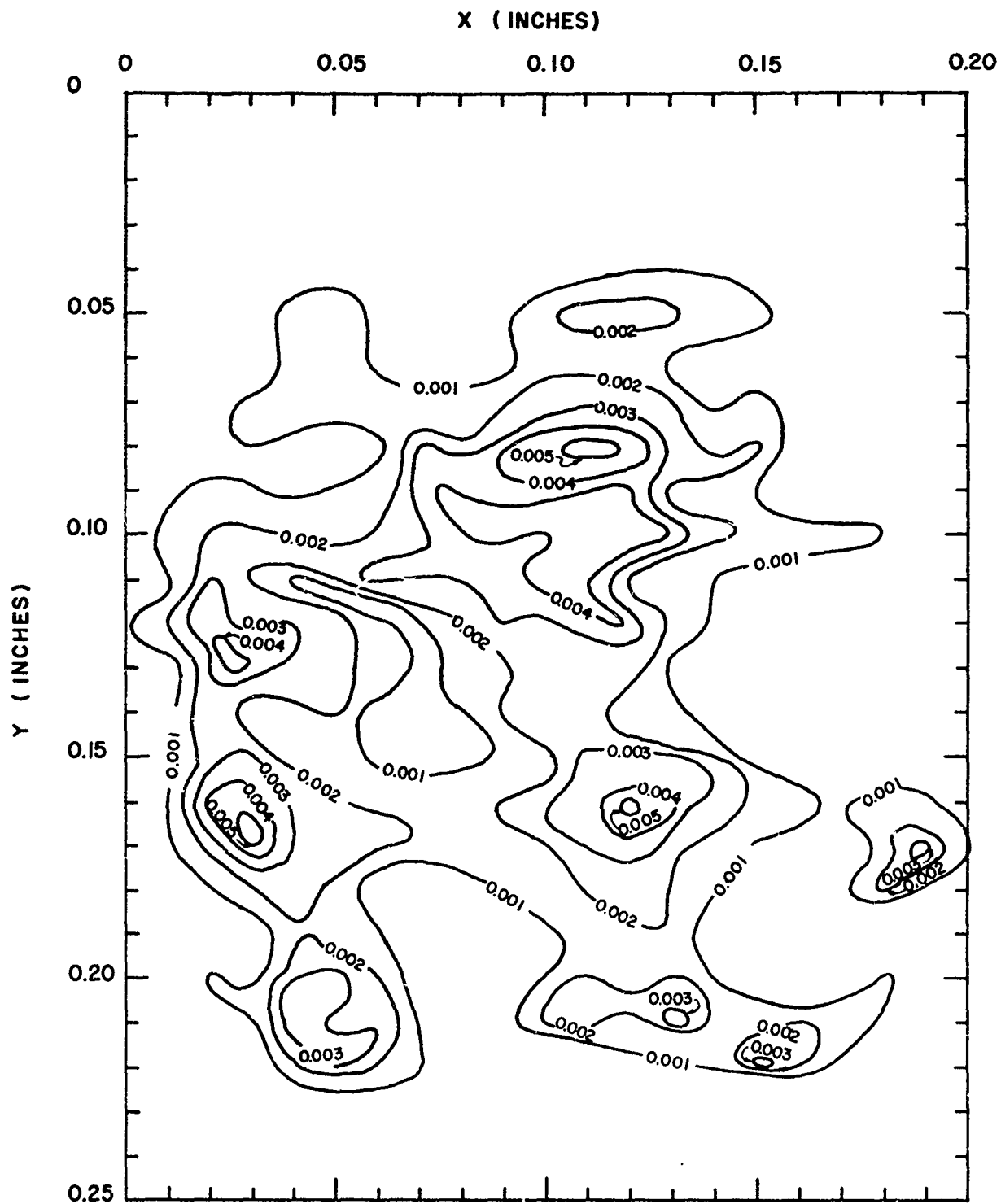FIGURE 66 PHOTOGRAPHS OF CRATERS NEAR TIP

FIGURE 6.7 CRATER CROSS – SECTIONS

FIGURE 6.8   DEPTH   CONTOURS
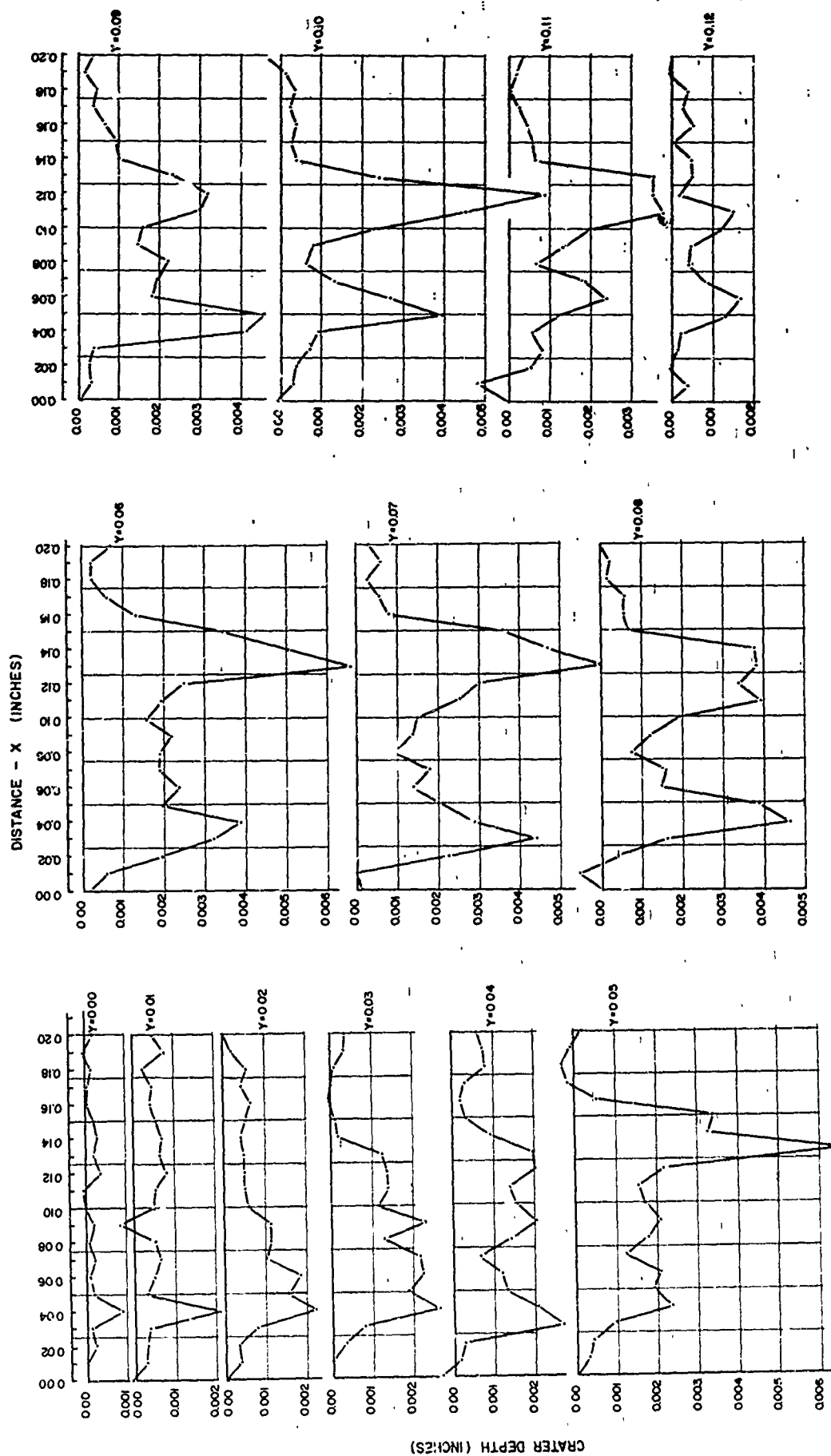
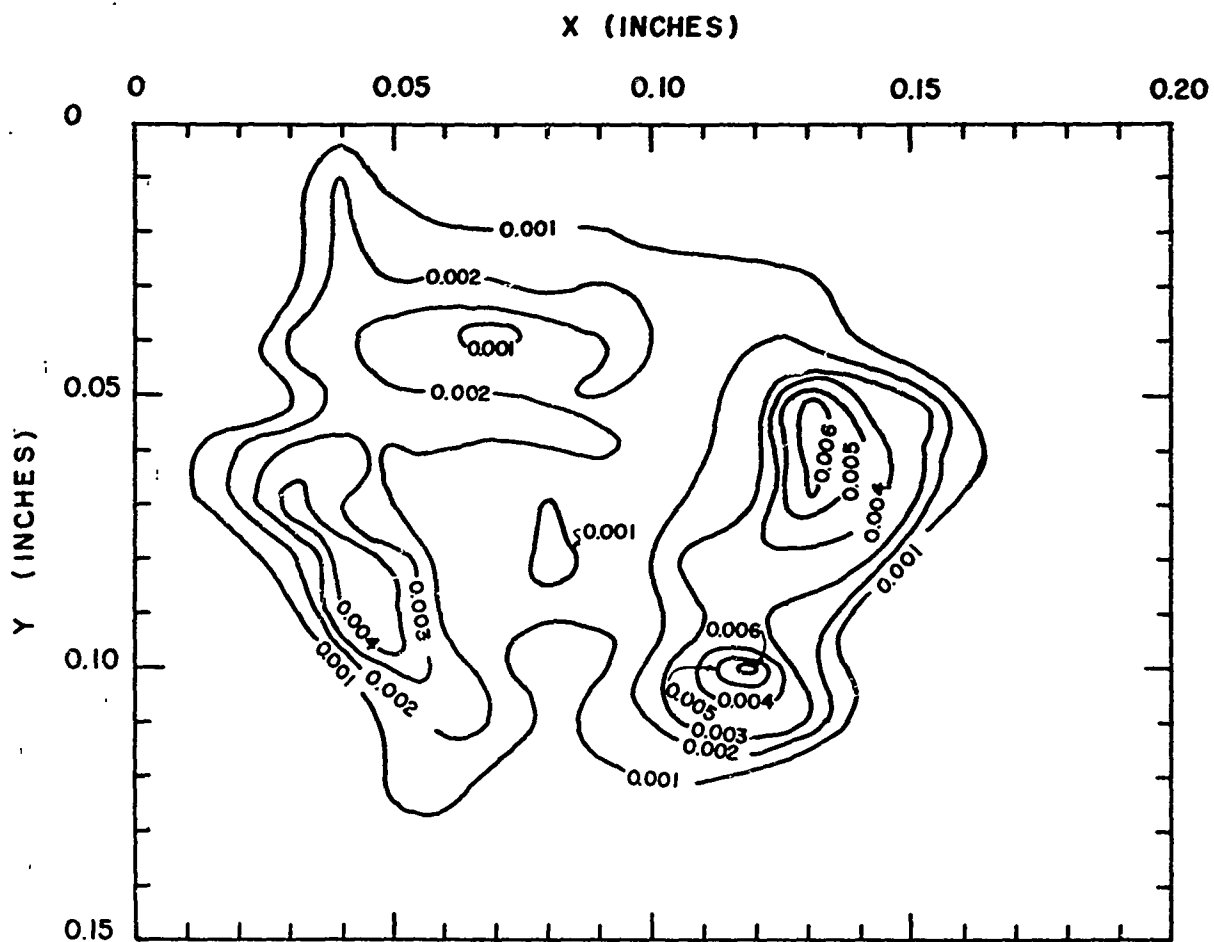FIGURE 6.9 CRATER CROSS – SECTIONS

FIGURE 6.10   DEPTH   CONTOURS

APPENDIX 1

by

H. W. Bennett, D. E. Re: ioids, and J. C. Smelcer

The purpose of this appendix is to present a closed-form approximate solution for the drop-phase flow field on thin wedges and cones. Such solutions are useful in that they allow designers to make rapid estimates of the flow variables without having to engage in extensive numerical calculations. The notation is the same as in section II of the body of this report unless otherwise stated. For simplicity in the analytical work attention is restricted to the linear drag law and tangential and normal coordinates, x and y respectively, are used.

In dimensionless form the governing equations are

$$((\theta_b s + n)^j Q_p F_p)_{,s} + ((\theta_b s + n)^j Q_p G_p)_{,n} = 0$$

$$F_p F_{p,s} + G_p F_{p,n} = \alpha_1 (1 - F_p)$$

$$F_p G_{p,s} + G_p G_{p,n} = -\alpha_1 ((jn/s) + G_p)$$

$$F_p H_{p,s} + G_p H_{p,n} = \alpha_1 (H_s - H_p) \qquad (A1)$$

where (A1a) results from balance of mass, (A1b) from balance of tangential linear momentum, (A1c) from balance of normal linear momentum, (A1d) from balance of energy, and the dimensionless variables are defined as in (2.9) and (2.10). Defining a stream function such that

$$\psi_{p,s} = -(\theta_b s + n)^j Q_p G_p, \qquad \psi_{p,n} = (\theta_b s + n)^j Q_p F_p \qquad (A2)$$

and converting the governing equations to independent variables ψ_p and z = n one obtains

$$G_p F_{p,z} = \alpha_1 (1 - F_p)$$

$$G_p G_{p,z} = -\alpha_1 ((jz/s) + G_p)$$

$$G_p H_{p,z} = \alpha_2 (H_s - H_p)$$

$$G_p s,_z = F_p$$

$$Q_p = -1/((\theta_b s + z)^j G_p s,_{\phi_p}) \tag{A3}$$

Using (A2) evaluated on the shock a relation between the origin of each streamline z_s and the stream function can be found. This was used to rewrite (A3e) as

$$Q_p = -(\theta_s/(\theta_s-\theta_b))^{1+j} (z_s/(\theta_b s+z))^j (1/G_p s,_{z_s}) \tag{A4}$$

The appropriate boundary conditions on the shock $z = z_s$ are

$$F_p = 1, \quad G_p = -\theta_b, \quad Q_p = 1, \quad H_p = 1, \quad s = z_s/(\theta_s-\theta_b) \tag{A5}$$

It was first attempted to solve (A3) and (A4) by a perturbation method for small α_1. The first two approximations were found but the labor involved in computing further approximations was so extensive that this was not done. The second approximation was found to be valid only for $\alpha_1 \ll 1$. Thus the perturbation scheme was abandoned. Instead it was decided to linearize the nonlinear terms in (A3) using the values of G_p and s on the shock. When this is done the linearized equations have the form

$$-\theta_b F_p,_z = \alpha_1(1 - F_p)$$

$$-\theta_t G_p,_z = -\alpha_1(j(\theta_s-\theta_b)(z/z_s) + G_p)$$

$$-\theta_b H_p,_z = \alpha_2(H_s - H_p)$$

$$-\theta_b s,_z = F_p \tag{A6}$$

The solutions to (A6) satisfying the boundary conditions (A5) are easily found to be

$$F_p = 1$$

$$G_p = -\theta_b \exp(-(\alpha_1/\theta_b)(z_s-z)) + j((\theta_s-\theta_b)/z_s)((z_s$$
$$+ (\theta_b/\alpha_1))\exp(-(\alpha_1/\theta_b)(z_s-z)) - (z + (\theta_b/\alpha_1)))$$

$$H_p = H_s - (H_s-1)\exp(-(\alpha_2/\theta_b)(z_s-z))$$

$$s = (z_s/(\theta_s-\theta_b)) + ((z_s-z)/\theta_b) \tag{A7}$$

Using (A7) and

$$S_{,z_s} = \theta_s/(\theta_b(\theta_s-\theta_b))\} \tag{A8}$$

the dimensionless density Q_p can be easily evaluated from (A4).

Figures A.1 and A.2 show comparisons of the approximate results with the numerical solutions obtained for slender wedges and cones in section II. The density ratio is $\varepsilon = 0.1$ for this data. The quantities chosen for comparison are the normal velocity and the density of the drop phase evaluated at the vehicle surface. It can be seen that for small and moderate values of α_1 the approximate solution is in good agreement with the numerical results (for the wedge the numerical results are identical to the exact analytical solution given in section II). For $\alpha_1 = 10$ the approximate solution begins to overestimate the impact velocity and underestimate the density. This could probably be corrected by modifying the linearizing factors but this was not attempted in the present work.

The agreement between the exact and approximate solutions appears to be satisfactory for small and moderate values of the drag parameter α_1. It appears that a similar procedure could also be used to obtain approximate results for general shock layer problems.
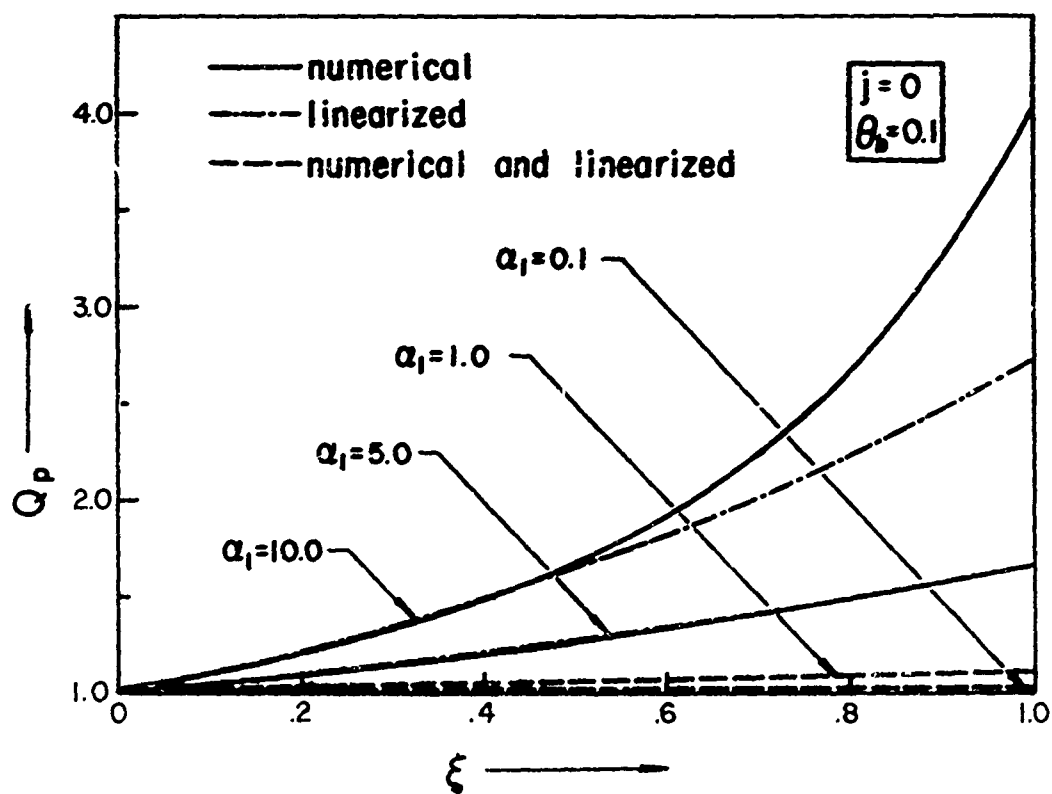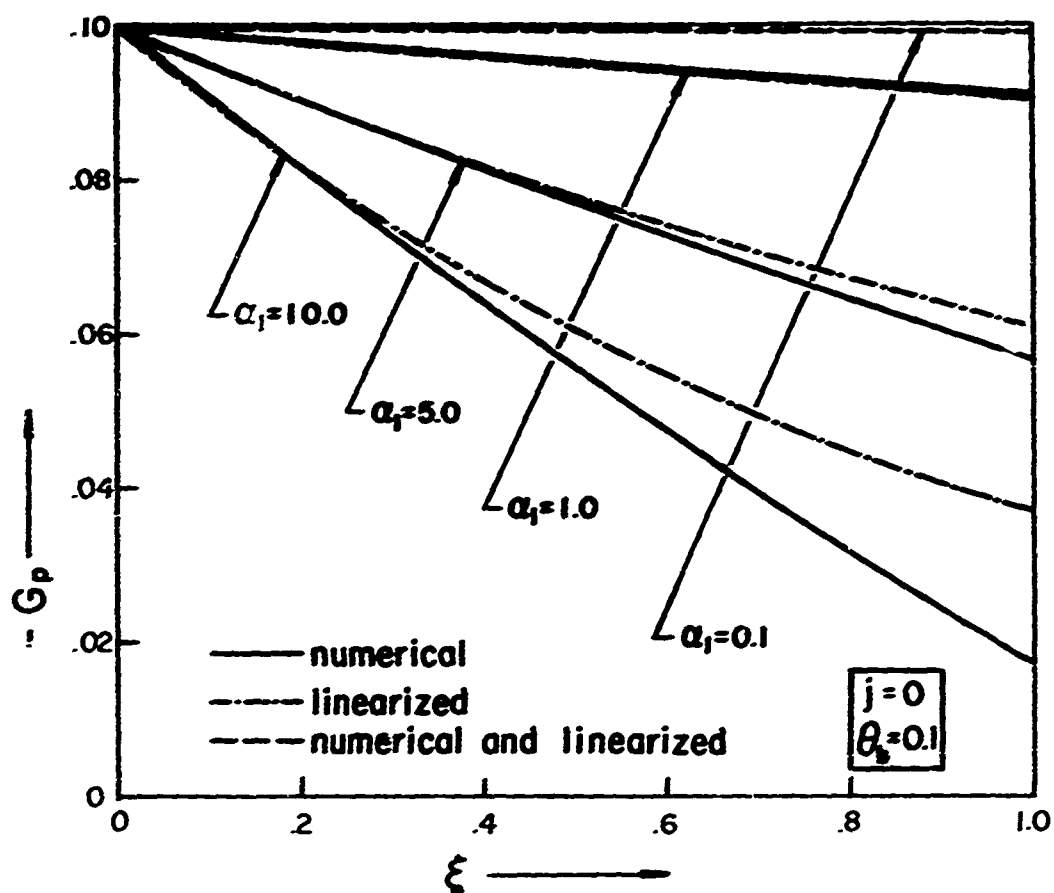
FIGURE A.1.   SURFACE DISTRIBUTIONS OF DROP-PHASE NORMAL VELOCITY
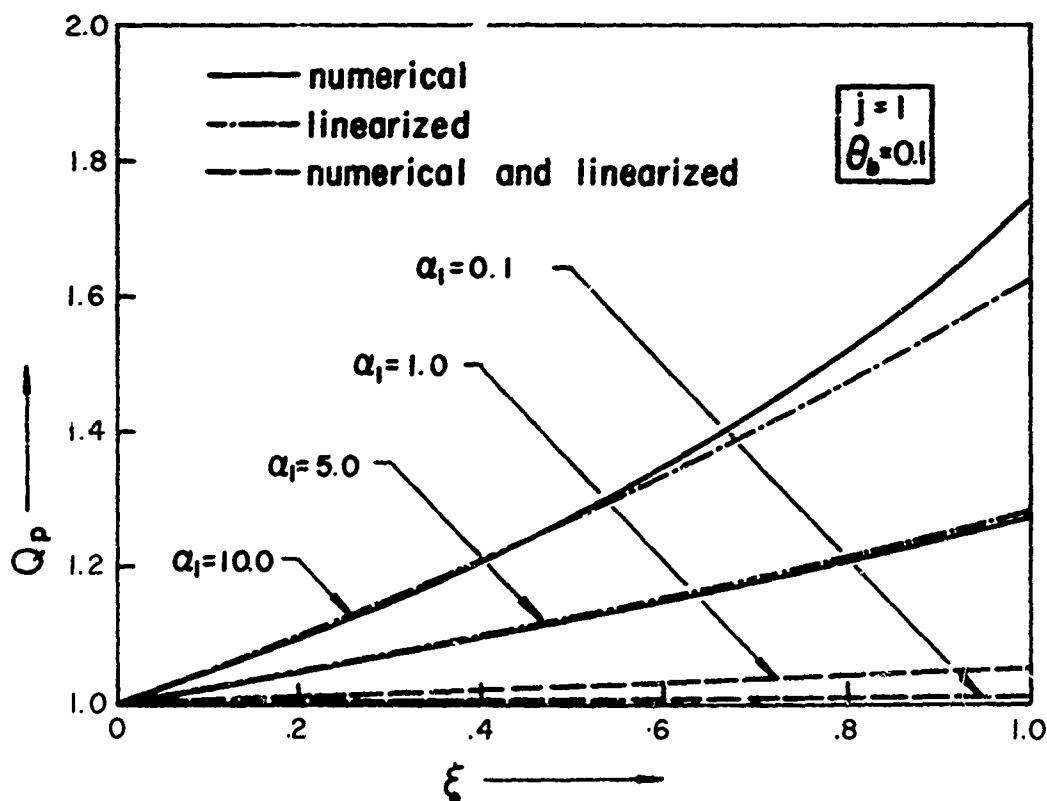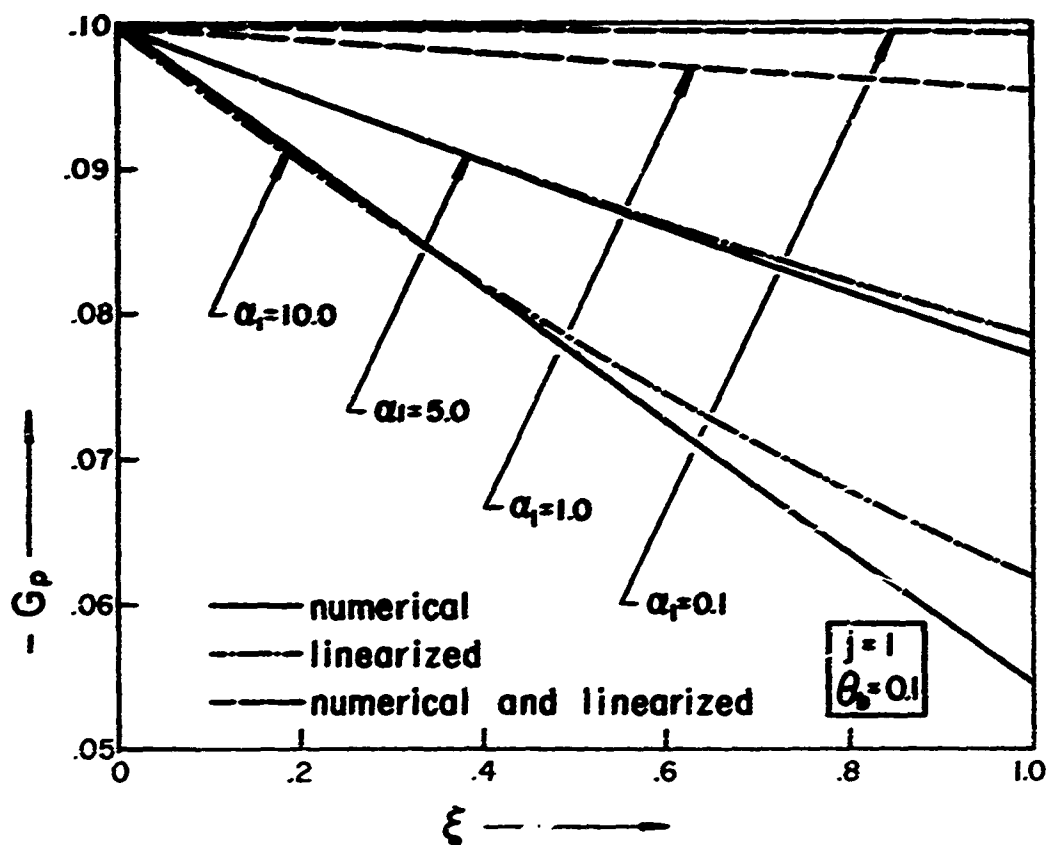AND DROP-PHASE DENSITY

FIGURE A.2.   SURFACE DISTRIBUTIONS OF DROP-PHASE NORMAL VELOCITY
AND DROP-PHASE DENSITY